# ผลของแบบรูปการไหลต่อการจับยึดคาร์บอนไดออกไซด์โดยใช้โพแทสเซียมคาร์บอเนตในฟลูอิไดซ์เบดแบบหมุนเวียน

นางสาวอ้ออำไพ ใจบุญ

วิทยานิพนธ์นี้เป็นส่วนหนึ่งของการศึกษาตามหลักสูตรปริญญาวิทยาศาสตรดุษฎีบัณฑิต

สาขาวิชาเคมีเทคนิค ภาควิชาเคมีเทคนิค

คณะวิทยาศาสตร์ จุฬาลงกรณ์มหาวิทยาลัย

ปีการศึกษา 2554

# EFFECTS OF FLOW PATTERN ON $CO_2$ CAPTURE USING POTASSUIM CARBONATE IN CIRCULATING FLUIDZED BED

Miss Or-ampai Jaiboon

A Dissertation Submitted in Partial Fulfillment of the Requirements

for the Degree of Doctor of Philosophy Program in Chemical Technology

Department of Chemical Technology

Faculty of Science

Chulalongkorn University

Academic Year 2011

| | |
|---|---|
| Thesis Title | EFFECTS OF FLOW PATTERN ON $CO_2$ CAPTURE USING POTASSIUM CARBONATE IN CIRCULATING FLUIDIZED BED |
| By | Miss Or-ampai Jaiboon |
| Field of Study | Chemical Technology |
| Thesis Advisor | Associate Professor Pornpote Piumsomboon, Ph.D. |

Accepted by the Faculty of Science, Chulalongkorn University in Partial Fulfillment of the Requirements for the Doctoral Degree

…….....Dean of the Faculty of Science

(Professor Supot Hannongbua, Dr.rer.nat.)

THESIS COMMITTEE

……..……Chairman

(Associate Professor Kejvalee Pruksathron, Ph.D.)

…….Thesis Advisor

(Associate Professor Pornpote Piumsomboon, Ph.D.)

……..Examiner

(Professor Pattarapan Prasassarakich, Ph.D.)

……..Examiner

(Assistant Professor Prapan Kuchontara, Ph.D.)

……..External Examiner

(Boonrod Sajjakulnukit, Ph.D.)

อ้ออำไพ ใจบุญ : ผลของแบบรูปการไหลต่อการจับยึดคาร์บอนไดออกไซด์โดยใช้โพแทสเซียมคาร์บอเนตในฟลูอิไดซ์เบดแบบหมุนเวียน. (EFFECTS OF FLOW PATTERN ON $CO_2$ CAPTURE USING POTASSIUM CARBONATE IN CIRCULATING FLUIDIZED BED) อ.ที่ปรึกษาวิทยานิพนธ์หลัก : รศ.ดร. พรพจน์ เปี่ยมสมบูรณ์, 172 หน้า

วัตถุประสงค์ของงานวิจัยนี้เพื่อศึกษาผลของแบบรูปการไหลภายในเครื่องปฏิกรณ์ฟลูอิไดซ์เบดที่ทำจากแก้ว ที่มีขนาดเส้นผ่านศูนย์กลางภายใน 0.025 เมตร และความสูง 0.80 เมตร ต่อการดูดซับคาร์บอนไดออกไซด์จากไอเสียหลังกระบวนการเผาไหม้เชื้อเพลิงฟอสซิล ที่อุณหภูมิ 60 องศาเซลเซียส ด้วยตัวดูดซับโพแทสเซียมคาร์บอนเนตบนตัวรองรับอลูมินา สำหรับแบบรูปการไหลภายในเครื่องปฏิกรณ์ฟลูอิไดซ์เบดถูกแบ่งแยกด้วยวิธีการศึกษาการกวัดแกว่งความดัน ซึ่งสามารถแบ่งแยกแบบรูปการไหลจากความเร็วอากาศที่เพิ่มขึ้นได้ 5 แบบรูป ได้แก่ เบดนิ่ง, เบดแบบฟองอากาศ, เบดแบบสลักกิ้ง, เบดแบบปั่นป่วน และเบดแบบความเร็วสูง จากการทดลองพบว่าเบดแบบนิ่ง และแบบฟองอากาศสามารถกำจัดคาร์บอนไดออกไซด์ได้ทั้งหมด สำหรับเบดแบบสลักกิ้ง, แบบปั่นป่วน และแบบความเร็วสูงไม่สามารถกำจัดคาร์บอนไดออกไซด์ได้ทั้งหมด โดยสัดส่วนการกำจัดคาร์บอนไดออกไซด์ที่สูงที่สุดสำหรับเบดแบบสลักกิ้ง, ปั่นป่วน และความเร็วสูง ได้แก่ 0.98, 0.94 และ 0.72 ตามลำดับ แต่อย่างไรก็ตามตัวดูดซับในเบดแบบปั่นป่วนมีความสามารถในการดูดซับคาร์บอนไดออกไซด์สูงสุด โดยตัวดูดซับสามารถดูดซับได้ร้อยละ 90 ของความสามารถในการดูดซับทางทฤษฎี โดยลำดับความสามารถในการดูดซับรองลงมา ได้แก่ เบดแบบฟองอากาศ และเบดแบบความเร็วสูง โดยดูดซับได้ร้อยละ 66-72 ของความสามารถในการดูดซับทางทฤษฎี โดยเบดแบบนิ่งและเบดสลักกิ้ง ให้ความสามารถในการดูดซับที่ต่ำที่สุด คือร้อยละ 53-60 ของความสามารถในการดูดซับทางทฤษฎี และในงานวิจัยนี้ยังศึกษาผลของอุณหภูมิต่อการฟื้นฟูตัวดูดซับโพแทสเซียมคาร์บอนเนต พบว่าการฟื้นฟูตัวดูดซับที่อุณหภูมิสูงกว่า 300 องศาเซลเซียส ตัวดูดซับมีเสถียรภาพมากที่สุด

ภาควิชา เคมีเทคนิค ลายมือชื่อนิสิต .....

สาขาวิชา เคมีเทคนิค ลายมือชื่อ อ.ที่ปรึกษาวิทยานิพนธ์หลัก .....

ปีการศึกษา 2554 .....

# # 5073901923 : MAJOR CHEMICAL TECHNOLOGY
KEYWORDS : $CO_2$ CAPTURE/ ADSORPTION/ FLUIDIZED BED/ SOLID SORBET/POTASSIUM CABONATE/ $CO_2$ REGENERATION

OR-AMPAI JAIBON: EFFECTS OF FLOW PATTERN ON $CO_2$ CAPTURE USING POTASSIUM CARBONATE IN CIRCULATING FLUIDIZED BED. ADVISOR: ASSOC.PROF. PORNPOTE PIUMSOMBOON, Ph.D., 172 pp.

The purpose of this study is to investigate the effect of flow pattern/regime in fluidized bed/circulating fluidized bed on $CO_2$ capture from flue gas, released from a fossil fuel combustion process, at low temperature 60 °C using potassium carbonate supported on alumina ($K_2CO_3/Al_2O_3$) solid sorbent prepared by impregnation method. The semi-circulating fluidized riser made from glass has 0.025 m of inner diameter and 0.80 m of height. The flow pattern/regime was characterized by measuring pressure fluctuation in the riser. It can be divided into five different flow patterns/regimes including fixed bed, multiple bubbling, slugging, turbulent and fast fluidization as gas velocity increased. The fixed bed and multiple-bubbling bed could adsorb all $CO_2$ in flue gas ($CO_2$ removal fraction = 1). The slugging, turbulent and fast fluidization could not remove all $CO_2$ in flue gas. Maximum $CO_2$ removal fractions for slugging, turbulent and fast fluidization are 0.98, 0.94 and 0.72, respectively. However, the turbulent regime provides the best $CO_2$ capture capacity at about 90% of stoichiometic theoretical value. The $CO_2$ capture capacity for the multiple-bubbling and fast fluidization regimes are secondary with about 66-72% of stoichiometic theoretical value. The fixed bed and slugging regimes provide the poorest $CO_2$ capture capacity at about 53-60% of stoichiometic theoretical value. For $K_2CO_3/Al_2O_3$ solid sorbent, this solid sorbent was completely regenerated for temperature higher than 300 °C resulting in higher stability to maintain capacity.

Department : Chemical Technology Student's Signature .....

Field of Study : Chemical Technology Advisor's Signature .....

Academic Year : 2011 .....

# ACKNOWLEDGEMENTS

This dissertation would have never been successful without the assistance of the following persons and organizations:

I would like to express my deepest appreciation to my dissertation advisor, Associate Professor Pornpote Puimsomboon, Ph.D. and Associate Professor Lursaung Mekasut, Ph.D., for their endless special guidance, who reviewed this dissertation, offered many helpful suggestions, and much encouraged of my research. They always teach me not only the theoretical knowledge but also the other skills to think and to solve many problems. Moreover, I especially extend my appreciation to Professor Pattarapan Prasassarakich, Ph.D., Associate Professor Kejvalee Pruksathron, Ph.D., Assistant Professor Prapan Kuchontara, Ph.D., and Mr. Boonrod Sajjakulnukit, Ph.D., for their participation on the dissertation chairman and committees.

Secondly, I am sincerest appreciation also extends to Energy Policy and Planning Office of Ministry of Energy and Center for Petroleum, Petrochemicals and Advanced Materials for their financial support throughout this research.

Thirdly, many thanks are extended to all members and staff of the Department of Chemical Technology, Chulalongkorn Universtiy for their assistance and friendships.

The last, I would like to extensively thank my family, Teste family members and especially Mr Christophe Teste for their support, assistance and encouragement. Without their love and support, I would not be able to success my doctoral degree.

# CONTENTS

Page

Page

# LIST OF TABLES

Page

Page

# LIST OF FIGURES

Page

Page

Page

# CHAPTER I

# INTRODUCTION

## 1.1 General Introduction- Rationale

Carbon dioxide ($CO_2$) is a major gas released into the atmosphere due to the intensive use of fossil fuels. Nowadays, global warming remains a critical issue for the industries and $CO_2$ emission plays a key role in the greenhouse effect. Therefore, reducing $CO_2$ emission is still one of the main concerns to prevent from climate changes and coal fired power plants are the most important source of producing $CO_2$. To reduce $CO_2$ emission, the options are to increase the efficiency of energy conversion, to switch to less carbon intense fuels, and to use renewable energies [1]. On the other hand, these options may not be sufficient to control the $CO_2$ concentration in the atmosphere in the future. Currently, $CO_2$ capture and storage option becomes highly promising. With this technology, various methods to capture $CO_2$ have been used and investigated such as adsorption, absorption, membrane separation, cryogenic separation and others. Among these methods, chemical sorption with liquid solvents, mainly amines and ammonia, is the most developed nowadays. $CO_2$ reacts with both solvents, and is then released as a pure gas when the solution is heated. However, liquid solvent separation is expensive and energy intensive, because of the large volume of gas and the low partial pressure of $CO_2$ in the flue gas. The presence of contaminants could deteriorate the solvent and increase the energy demand associated with solvent regeneration [2].

One of the improved techniques for $CO_2$ removal is the chemical sorption with dry solid sorbents. The use of solid sorbents can be a highly cost effective and energy efficient way to remove $CO_2$ because of the ease of material handling, the safety for local environment, high $CO_2$ capacity capture, lower regeneration energy and multi-pollutant control [3]. An alkaline carbonate support on the porous particle has been proposed as solid sorbent for $CO_2$ capture. Data from several reviews confirmed that $CO_2$ is effectively adsorbed on the alkaline carbonate solid sorbent during multiple cycles [3,4]. Among various alkaline carbonate such as $Li_2CO_3$, $Na_2CO_3$ and $K_2CO_3$, $K_2CO_3$ has been revealed to give results in adsorbing $CO_2$ in wide range of temperature. For example, the $K_2CO_3$ still efficiently adsorbs $CO_2$ at 100°C temperature, while, $Na_2CO_3$ and $Li_2CO_3$ could critically decomposed at lower temperature (<60°C) [4]. Consequently, $K_2CO_3$ was preferred to use in this study.

The chemical reactions involved in $CO_2$ capture with $K_2CO_3$ solid sorbent are shown in following equations (1.1) and (1.2):

$$\text{Carbonation:} \quad K_2CO_3 + CO_2 + H_2O \longrightarrow 2KHCO_3 + \text{heat} \quad (1.1)$$

$$\text{Regeneration:} \quad 2KHCO_3 \longrightarrow K_2CO_3 + CO_2 + H_2O - \text{heat} \quad (1.2)$$

The reactions characterizing $CO_2$ capture can be divided following two steps: carbonation and regeneration. Potassium carbonates ($K_2CO_3$) react with $CO_2$ and $H_2O$ and are transformed to potassium hydrogen carbonates ($KHCO_3$) after $CO_2$ sorption during the carbonation reaction (equation (1.1)). For decomposed, these potassium hydrogen carbonates can be thermally regenerated to the alkaline potassium carbonates and $CO_2$ by heating the alkaline metal carbonates (equation (1.2)). Water vapor is needed to form potassium hydrogen carbonates as shown in the carbonation reaction (equation (1.1)). Therefore moisture contained in the flue gases, as high as 8-

17% content, is useful for the $CO_2$ capture reaction, while it negatively affects the adsorption capacity of molecular sieves processes [5].

The adsorption is an exothermic reaction and regeneration is an endothermic one. Heat is a crucial important factor which have to controlled in the process in order to prevent hot spot creation during carbonation reaction. In consequence, the fluidization technique is a good solution for this process. Fluidized beds are ideal contacting devices for solid-gas systems that require large circulation rate of solids. Internal and external solids transport, reactions of solids and gas streams, such as adsorption and desorption reactions, are greatly enhanced by the excellent mixing of the reactants through the fluidized bed [6].

Currently, many researches focused already their works on the improvement of the performance of $K_2CO_3$ based sorbent by modifying solid sorbent characteristics. Lee et al., [5] modified the $K_2CO_3$ solid sorbent by water pretreatment before adsorption in fixed bed reactor. The $K_2CO_3$ formation was changed to new active species defined as $K_2CO_3 \bullet 1.5H_2O$ providing enhance $CO_2$ capture capacity and reaction rate. The kinetic behavior of $CO_2$ adsorption by $K_2CO_3$ in porous material was studied in fixed-bed reactor [7]. Lee et al., [5] investigated the $CO_2$ adsorption and regeneration of potassium carbonate sorbent such as $K_2CO_3$/AC (activated carbon), $K_2CO_3/TiO_2$, $K_2CO_3$/MgO, $K_2CO_3/ZrO_2$ and $K_2CO_3/Al_2O_3$ in a fixed bed reactor.

They obtained some interesting and promising results on $CO_2$ adsorption characteristic of $K_2CO_3$ solid sorbent. However, all researchers faced the same problem and concluded on the same issue: the reaction rate of $K_2CO_3$ was rather slow and the capture capacity reached only 80 % of theoretical values [5, 7]

As a result, the transport phenomena of the reaction of $K_2CO_3$ solid sorbent and $CO_2$ and water is still observed to be not completely investigated and is still missing to optimize $CO_2$ Capture process. The transport phenomena of a fluidized bed reactor consist of hydrodynamic analysis. The hydrodynamic of gas-solid in a fluidized bed largely depends on the fluidization regime. The gas-solid mixing characteristic is also affected by the fluidization regime. Information of gas-solid mixing may be used to evaluate reaction conversion and selectivity at different flow regime in a fluidized bed.

This research focused on the effect of flow pattern in fluidization/circulating fluidization systems, including fixed bed, multiple bubbling, slugging, turbulent and fast fluidization regimes, on $CO_2$ removal efficiency and $CO_2$ capture capacity using $K_2CO_3$ solid sorbent.

## 1.2 Purposes of this Study

- To design and construct the riser of a semi-circulating fluidized bed reactor.
- To study the effect of flow pattern/regime on the $CO_2$ sorption activities of $K_2CO_3/Al_2O_3$ solid sorbent in fluidization system.
- To study the regeneration process of $K_2CO_3/Al_2O_3$ solid sorbent in the fluidization system.

Hypothesis: To propose the flow pattern/regime in fluidized bed/circulating fluidized bed and the regeneration temperature that provides the most efficient $CO_2$ capture capacity and regeneration property.

## 1.3 Scope of the Dissertation

1. Design and Construct the semi-circulating fluidized bed together with setting up the tool such as pressure and temperature probes, which are used to measure the pressure and temperature, respectively, in the riser.

2. Prepare $K_2CO_3/Al_2O_3$ solid sorbent by conventional impregnation method.

3. Investigate the hydrodynamic parameters of $K_2CO_3/Al_2O_3$ solid sorbent in the simi-circulating fluidized bed riser such as solid volume fraction and pressure fluctuation to determine the flow regime at various gas velocity.

4. Investigate the effect of adsorption temperature and water vapor content in simulated flue gas on $CO_2$ capture breakthrough and $CO_2$ capture capacity of $K_2CO_3/Al_2O_3$ solid sorbent

5. Investigate the effect of flow pattern/regime in fluidized bed/circulating fluidized bed on $CO_2$ capture breakthrough and $CO_2$ capture capacity of $K_2CO_3/Al_2O_3$ solid sorbent

6. Investigate the effect of regeneration temperature on $CO_2$ capture breakthrough and $CO_2$ capture capacity of $K_2CO_3/Al_2O_3$ solid sorbent.

7. Characterize $K_2CO_3/Al_2O_3$ solid sorbent : the prepared solid sorbent are characterized by analyzers such as

- The Brunauer-Emmett-Teller (BET) method is carried out to determine the surface area of prepared solid sorbent by $N_2$ adsorption/desorption.

- X-ray diffactometer (XRD) is used for the examination of the crystalline structure.

- Temperature programmed desorption (TPD) is introduced to investigate the desorption of prepared solid sorbent

- Thermogravimetric analysis (TGA) and Differential thermal analysis (DTA) and atomic absorption (AA) is used to investigate the actual weight of $K_2CO_3$ impregnated on supporter.

**Anticipated benefits**

1. To set-up a fluidized bed reactor for $CO_2$ capture from flue gas after fossil-fuel combustion process for producing high cleaning flue gas.

2. To obtain an effective flow pattern in fluidization/circulation fluidization system for $CO_2$ capture from flue gas.

3. To obtain a suitable regeneration temperature for $CO_2$ desorb using $K_2CO_3/Al_2O_3$ solid sorbent.

## 1.4 Format of the Dissertation

The dissertation was formatted in a chapter form. Background, purpose and scope of this research work were presented in Chapter 1. Theoretical information and literature reviews were presented in Chapter 2. Material used in this work and methodology, accompany with solid sorbent preparation, flow pattern/regime characterization, $CO_2$ adsorption and solid sorbent regeneration, were described in Chapter 3. Flow pattern/regime in fluidization characterization was revealed in Chapter 4. Effect of flow pattern/regime on $CO_2$ adsorption capacity was evaluated in Chapter 5. Effect of temperature on solid sorbent regeneration capacity was studied in Chapter 6. Finally conclusion and recommendations were introduced in Chapter 7.

# CHAPTER II

# THEORY AND LITERATURE REVIEWS: $CO_2$ CAPTURE AND FLUIDIZATION

$CO_2$ capture systems and technologies currently available are presented in section 2.1 and 2.2 respectively. In this research, the gas-solid fluidization has been selected to be investigated for $CO_2$ capture by using potassium carbonate solid sorbent. Therefore, fluidization definition and notions are introduced in section 2.3 to have a better understanding on the practical process application. Flow patterns/regimes in fluidization are detailed in section 2.4. Eventually, fluidization property of solid used in this research is explained in section 2.5.

## 2.1 $CO_2$ Capture Systems

The aim of $CO_2$ capture process is to separate $CO_2$ from industrial and energy-related sources. This process typically produces high $CO_2$ concentration streams, then transported to a storage location and long-term isolation from the atmosphere. There are three basic systems to capture $CO_2$ from combustion using fossil fuels and/or biomass including post-combustion capture, oxy-fuel combustion capture and pre-combustion as shown in Figure 2.1 [1,2].

- Post-combustion capture (described in section 2.1.1)

- Oxy-fuel combustion capture (described in section 2.1.2)
- Pre-combustion capture (described in section 2.1.3)

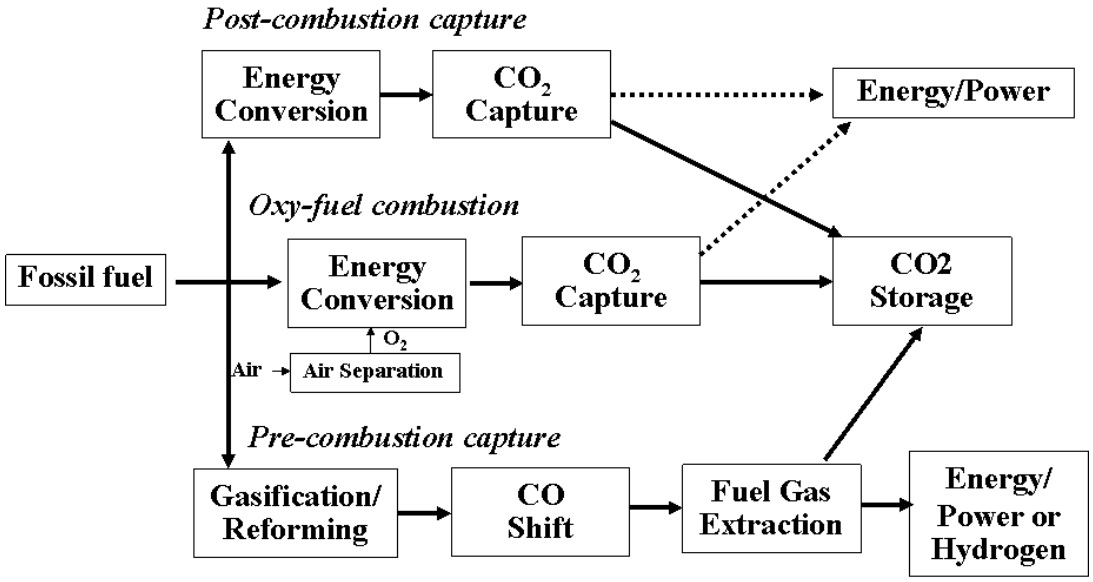


**Figure 2.1. $CO_2$ capture system pathways in fossil energy conversion processes.** [1].

### 2.1.1 Post-combustion Capture

Capture of $CO_2$ from flue gases in the downstream of fossil fuels and biomass combustion unit is generally referred to as post-combustion capture. In fossil fuels combustion process, flue gas stream after combustion contains lean concentration of $CO_2$ (3-15 vol.%). This process, flue gas passed through processes, which can be used to separate most of the $CO_2$. The $CO_2$ is then transferred to a storage reservoir and the remaining cleaner flue gas is discharged to the atmosphere. Various techniques can be used to capture $CO_2$ such as absorption by amines, membrane separation and cryogenic separation etc. Nowadays, the absorption by amines is considered to be commercially available technology [1,8].

### 2.1.2 Oxy-fuel Combustion Capture

In oxy-fuel combustion capture system, the fossil fuels are burnt in pure oxygen instead of air, resulting in more complete combustion. When burnt with $O_2$, a flue gas consists of almost pure $CO_2$ (typically 80-98 vol.%) and water vapor. The water vapor stream can easily be separated from the $CO_2$ by condensation. The pure $CO_2$ stream can be compressed and stored, respectively. If the $CO_2$ content is very high, the removal of impurities (water vapor) can be operated at relatively acceptable costs. The major determining factor in cost and efficiency of oxy-fuel $CO_2$ capture is the oxygen production. Oxygen supply is usually produced by low temperature (cryogenic) air separation [1,9].

### 2.1.3 Pre-combustion Capture

A process where the carbon in the fossil fuel is separated or removed before the combustion is referred as pre-combustion capture. Instead of burning fuel in combustion, the fuels react with oxygen or air and/or steam through gasification or through steam reforming to produce mainly a synthesis gas, or fuel gas composed of carbon mono-oxide (CO) and hydrogen. The CO is then converted into $CO_2$ through shift conversion process resulting in a fuel gas composed mainly by $CO_2$ and $H_2$. Subsequently, the $CO_2$ can be removed, resulting in a hydrogen-rich fuel which can be combusted to produce power without $CO_2$ emission [1,11].

## 2.2 $CO_2$ Capture Technologies

$CO_2$ capture systems use many of well-known gas separation technologies. Various available technologies to separate and capture $CO_2$ can be classified as follow: [1]

- Separation with sorbents/solvents
- Separation with membrane
- Separation with cryogenic.

The general schematics of the main separation processes relevant for $CO_2$ capture are shown in Figure 2.2.

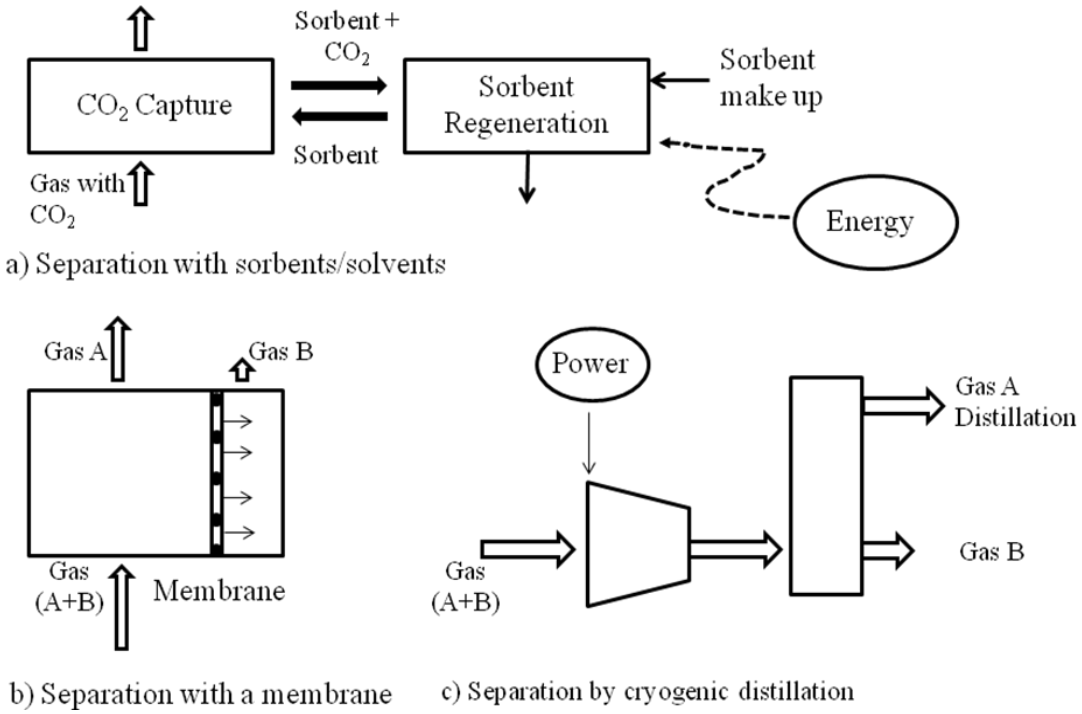


**Figure 2.2. General schemes of the main separation processes relevant for $CO_2$ capture (The gas removed in the separation may be $CO_2$, $H_2$, or $O_2$ in Figure 2.2b and 1c represent A and B)** [1]

### 2.2.1 Separation with Solvents/Sorbent Process

This process separates $CO_2$ from a mixed gas by contacting the gas with a liquid absorbent or solid sorbent which is able to capture $CO_2$ as shown in Fig.2.2a. Then, the $CO_2$ captured sorbent/solvents are brought to another vessel, where $CO_2$ can be released (regeneration) by different ways: bring heated or depressurized. The resulting sorbents after regeneration step are sent back to the $CO_2$ capture step to capture $CO_2$ again. There are two well-known solvents used for $CO_2$ capture such as ammonia and amine. Concerning solid sorbents, there are many possibilities, for example, metal oxide, metal based sorbent, zeolites, activated carbon etc. The separation with solvent/solid sorbent is based on the process of sorption between gas and solvent/solid sorbent that can be classified as follow:

- Chemical absorption process with amine (discussion in section 2.2.1.1)
- Physical adsorption process with porous material (discussion in section 2.2.1.2)
- Chemical adsorption process with regenerable solid sorbent (discussion in section 2.2.1.3)

#### 2.2.1.1 Chemical Absorption Process with Amine

Chemical absorption with amines has been widely used commercially to capture $CO_2$ from flue gas in fossil fuel combustion. Currently, there are three generated electric power plants in the U.S. that capture $CO_2$ from flue gas and six major flue gas $CO_2$ capture facilities worldwide. All nine are using amine as the chemical absorbent. Several amine solvents such as monoethanolmine (MEA),

diethanolamine (DEA), methyldiethanolamine (MDEA), or diisopropanolamine (DIPA) have been found as commonly operated with this technology [12].

The general method involves exposing a gas stream to an aqueous amine solution that reacts with the $CO_2$ in the gas by an acid-base neutralization reaction to form a soluble carbonate salt as shown in Equation 2.1

$$2RNH_2 + CO_2 + H_2O \leftrightarrow (RHN_3)2CO_3 \qquad (2.1)$$

This reaction is reversible, so the $CO_2$ gas can be released by heating in a separation step. Figure 2.3 describes the operation of a typical amine based absorption plant for recovery of $CO_2$ from flue gas. It can be separated into 3 main steps including flue gas pretreatment, absorption and regeneration step. Before $CO_2$ absorption step, the flue gas normally needs to be cooled and pretreated for decreasing impurities such as $SO_x$, $NO_x$ to suitable levels. Then, the cooled and pretreated flue gas passes through a feed blower to overcome the pressure drop in the absorber. In the absorber, the temperature is typically about 40-60°C. Flue gas is flowed up from the bottom of absorber and $CO_2$-lean amine inserted at the top of the absorber. In the absorber reactor, the $CO_2$ lean amine solution, in counter flow, comes in contact with the gas and absorbs the $CO_2$ from the flue gas. After absorption step, the $CO_2$-rich amine solution at the bottom of the absorber is pumped through a lean/rich exchanger. In this step, the $CO_2$-rich amine solution is heated to 105 °C by $CO_2$-lean amine solution. Then, the heated $CO_2$-rich amine enters into a stripper/regenerator. In the striper/regenerator, $CO_2$ is stripped out from the chemical solvent. The stripped lean amine accumulates in the bottom of the stripper/regenerator column and is recycled to the absorber for a new cycle. At the top of the stripper/regenerator column, $CO_2$

product, water vapor, and entrained amine enter the reflux condenser to separate $CO_2$ gas.

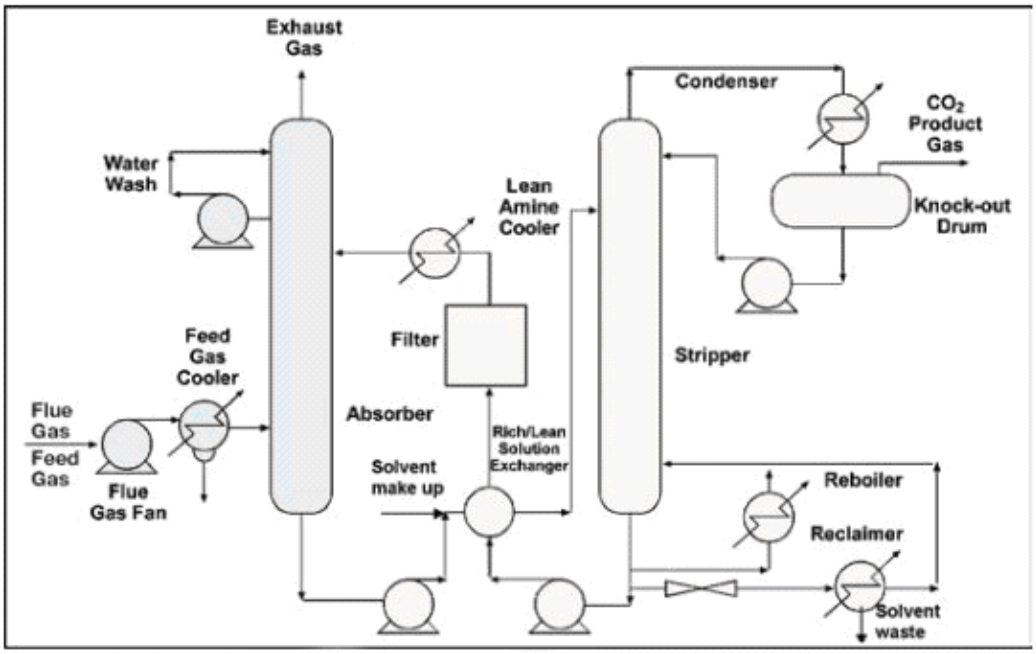


**Figure 2.3. Typical amine absorption process for $CO_2$ recovery from flue gas** [1]**.**

Chemical absorption with amines is the most cost-effective and well-known process to capture $CO_2$ from the flue gas because the obtained product after amine chemical absorption is a very high purity (>99%) $CO_2$ [13]. However, amine chemical absorption also has some major disadvantages: extremely slow reaction rate, large volume of solvent needed, toxic by product in regeneration step, the treatment of the solvents from recovery columns, the reduction of water consumption and the disposal process for expired solvent [14]. Moreover, the presence of contaminants, such as $O_2$, $SO_x$, $NO_x$, HCl, HF, Hg and particulates matters in the flue gas, reduces the absorption capacity of the amines significantly, and results in operational problems such as foaming and corrosion [15]. All these problems result into higher energy

requirement and efficiency penalty on power cycles decreasing in the same time initial interest for this process being less cost-effective.

Various alternative solvents to reduce the process cost have currently been developed. These solvents must have faster $CO_2$ absorption rate, low by product formation and low enery of desorption. The sterically hindered amines have been employed as innovative technology for $CO_2$ capture. They are amine with bulky groups attached to the nitrogen atom of amine molecule such as 2-amino-2-methyl-1-1proponal (AMP) and 2-piperidine ethanol (PE). They are commercially available for $CO_2$ capture in post-combustion system such as The Kansai Electric Power Co., Mistubishi Heavy Industries, Ltd., KEPCO/MHI Process [16]. The main advantages of this kind of amines over alkanolamies are lower circulation rate, lower heat of adsorption/regeneration and thermal degradation occurring at higher temperature as compared with MEA [17]. Dang and Rochelle (2001) proposed an aqueous solutions of blended monoethanolamine (MEA) and piperazine (PZ) to be another attractive alternative for $CO_2$ capture due to the faster $CO_2$ absorption rate resulting in lower energy consumption.

Beside novel solvents, novel process designs are also currently becoming available [18]. In 2001, Chakravati [13] invented the method that can prevent oxidative degradation of MEA solution by de-oxygenation of the solvent solutions. In addition, catalytic removal of oxygen in flue gas has been suggested to facilitate operation with promising solvents sensitive to oxygen [19]. Another type of process design aims at improving mass transfer between gas and liquid solvent by creating turbulence and greater interfacial area [20].

2.2.1.2 Physical Adsorption of Porous Solid Sorbent

Separation with porous particles, normally molecular sieves, zeolite or activated carbon, relies on the adsorption property of porous materials. The adsorption and desorption of $CO_2$ is operated with a pressure swing adsorption (PSA) or temperature swing adsorption (TSA). Most applications are associated with pressure swing adsorption while the TSA technique is less employed because it takes longer time to heat up the sorbent during regeneration process [21, 22].

Pressure swing adsorption relies on the fact that, under pressure, gases tend to be attached to solid surface and then to be adsorbed by porous particles. The higher the pressure is, the more gas is adsorbed. When reducing pressure, the gas is desorbed. PSA processes can be used to separate gases in a mixture as each gas will differently create higher or lower links with the solid surface. In the case of $CO_2$ recovery from syngas as shown in Figure.2.4, normally, the PSA process includes two reactors containing a zeolite adsorbent for operation continuous process. The first reactor (Bed A) is controlled under high pressure and then the syngas is passed through an adsorbent bed of zeolite that captures preferentially $CO_2$ rather than others. Therefore, the $CO_2$ in syngas will be adsorbed, and the gas entrained from the Bed A reactor will be dilute in $CO_2$. When the adsorbent material in Bed A reaches the limit capacity of $CO_2$ adsorption, the syngas flow entrance will be switched to pass through the other reactor (Bed B). During adsorption in Bed B, the $CO_2$-rich zeolite in Bed A, is regenerated by reducing the pressure and consequently releasing the adsorbed $CO_2$. When the adsorber in Bed B reactor reaches full capacity, the adsorbent in Bed A reactor will be ready to adsorb $CO_2$ by increasing pressure again. The pressure of

both reactors is switched alternately with high and low values giving the name to this process: Pressure Swing Adsorption.

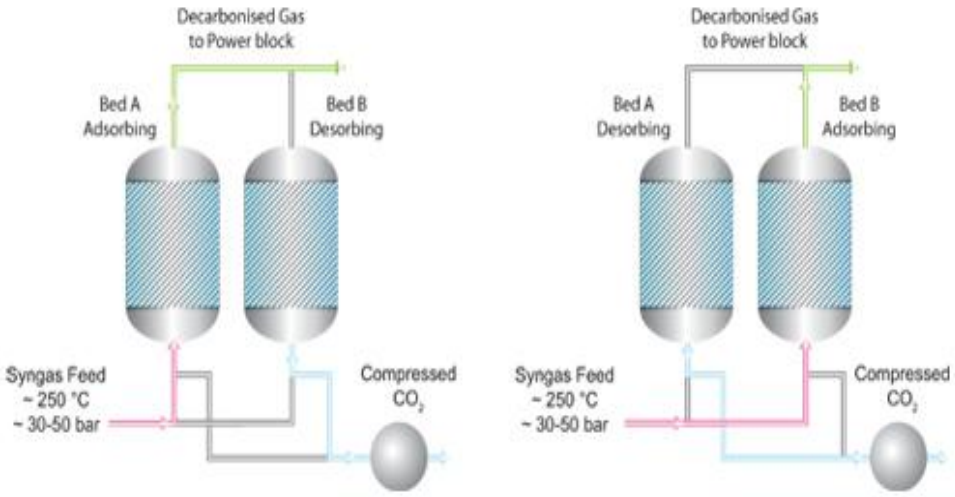


**Figure 2.4. Schematic f pressure swing adsorption (PSA) process for $CO_2$ recovery from syngas feed** [23]**.**

The crucial advantage of physical adsorption by porous material is the opportunity to have low energy requirement to regenerate the sorbent and quick regeneration time associated with changing the pressure. Adsorption processes have been used for $CO_2$ removal from synthesis gas for hydrogen production and from natural gas in its production. The $CO_2$ removal process from flue gas is not yet reached a commercial stage due to its low $CO_2$ selectivity and high power consumption. Another reason is the presence of water vapor in feed gas causing the reduction of adsorption capacity of porous solid sorbent.

Various novel methods have been investigated to increase the capacity of physical adsorption process of porous materials such as a combination of pressure and temperature swing adsorption (PTSA) and Electric swing adsorption (ESA). The PTSA were examined at the bench scale and pilot scale levels by Tokyo Electric

Power Company (TEPCO) and Mitsubishi Heavy industries, respectively [21]. The PTSA can reduce the power consumption required for separation when compared to PSA. The ESA technology is proposed as a possible advanced $CO_2$ separation technology that uses lower energy than other processes [24]. The ESA system is operated as an adsorption cycle followed by electrothermal desorption step performed by direct heating adsorbent particles with electrical current.

2.2.1.3 Chemical Adsorption of Regenerable Solid Sorbent

Chemical adsorption of $CO_2$ with a regenerable solid sorbent is also a promising technique to capture $CO_2$. This technique is proposed as post combustion $CO_2$ capture system by Shimizu (1999) [25]. The $CO_2$ capture process with a regenerable solid sorbent generally consists of two steps such as $CO_2$ capture or adsorption and regeneration as shown in Fig. 2.1 (a). The combustion flue gas is passed through the suitable reactor where the flue gas contacts with the regenerable solid sorbent. During this step, The $CO_2$ is chemically adsorbed on solid sorbent. Then a $CO_2$-rich regenerable solid sorbent is transported to the sorbent regeneration step. The $CO_2$-rich regenerable solid sorbent can be desorbed $CO_2$ by heat. The heat needed for regeneration is depending on the type of metal used and the chemical phase that occurs during $CO_2$ adsorption. Finally, the regenerated solid sorbent is sent back to start the $CO_2$ capturing cycle again.

Solid sorbent containing alkaline-and alkaline-earth metal and high surface area supporter are commonly investigated for their commercial feasibility. The high surface area allows for more numerous active sites for the desired reaction to occur. The common supporters used are alumina or silica.

The alkaline-earth metal has been investigated to capture $CO_2$ at high-temperature. The suitable alkaline-earth metals are magnesium oxide (MgO) and calcium oxide (CaO) based sorbent. The MgO/CaO based mineral have been considered as a sorbent for $CO_2$ capture since 19$^{th}$ century [1]. The carbonation reaction of MgO/CaO to capture $CO_2$ from the flue gas is favored at temperature higher than 600 °C. The reactions of MgO/CaO are very fast and produce stable carbonates ($MgCO_3$/$CaCO_3$). The regeneration of the MgO/CaO-based solid sorbent can be achieved by calcining the $MgCO_3$/$CaCO_3$ at > 900 °C and the product are MgO/CaO and pure $CO_2$. The general chemical reaction of $CO_2$ capture by using the CaO-based sorbent is

$$(Mg,Ca)O+CO_2 \leftrightarrow (Mg,Ca)CO_3 \qquad (2.2)$$

Even though the capacity of capture-regeneration by using MgO/CaO is higher than amine solvent absorption method [26, 27], the MgO/CaO is deactivated more rapid and a large make-up flow of sorbent is required to maintain the activity in the capture-regeneration loop [28]. As a solution to this weak point of MgO/CaO-based solid sorbent, several researchers proposed another type of metal to capture $CO_2$ from dry flue gas such as $Li_4SiO_4$ and $Li_2ZrO_3$. Both of Li-based metal are suitatble for high temperature flue gas. Among these Li-based metal, the lithium zirconate ($Li_2ZrO_3$) is a promising sorbent for temperature lower than 800°C due to its highly stable adsorption reactivity, good stability over many regeneration cycles, rapid regeneration at high temperature and thermal stability [29, 30, 31]. Moreover, it has high selectivity for $CO_2$. $CO_2$ capture and regeneration are expressed by the reversible reaction:

$$Li_2ZrO_3 + CO_2 \leftrightarrow Li_2CO_3 + ZrO_2 \qquad (2.3)$$

However, the $CO_2$ capture using $Li_2ZrO_3$ has extremely high operating costs because lithium is an expensive material.

Since the flue gas from fossil-fuel combustion power plant contains a small amounts of moisture, alkaline metal carbonates such as sodium carbonate ($Na_2CO_3$) and potassium carbonate ($K_2CO_3$) have been attractive alternatives for capturing $CO_2$, because they easily react with $CO_2$ and $H_2O$ and transform to alkaline metal hydrogen carbonate ($Na,KHCO_3$) after $CO_2$ adsorption by the following reaction,

$$(Na,K)_2CO_3 + CO_2 + H_2O \leftrightarrow 2(Na,K)HCO_3 \quad (2.4)$$

Water vapor is always necessary in forming sodium/potassium hydrogen carbonate in all reactions as shown in the adsorption mechanism unlike alkaline earth metal based sorbent, moisture contained in flue gases as high as 8-17 vol.% which negatively affects the adsorption capacity of molecular sieves [32]. In the $CO_2$ capture process for wet flue gas, $CO_2$ capture is effectively adsorbed at very low temperature (50-70 °C). After adsorption, the alkaline metal solid sorbent is transferred to the regeneration reactor, and it is regenerated by heating in the temperature range of 150-200 ºC. These regenerable solid sorbent can be used for a high number of cycles through the continuous operation the cycles. Figure 2.5 shows the intergration of the regenerable Na, K carbonate-based sorbent technology into a fossil fuel fired power plant with the final products being a stack gas essentially free of $CO_2$ and a pure $CO_2$ gas stream suitable for commercial sale or sequestration.

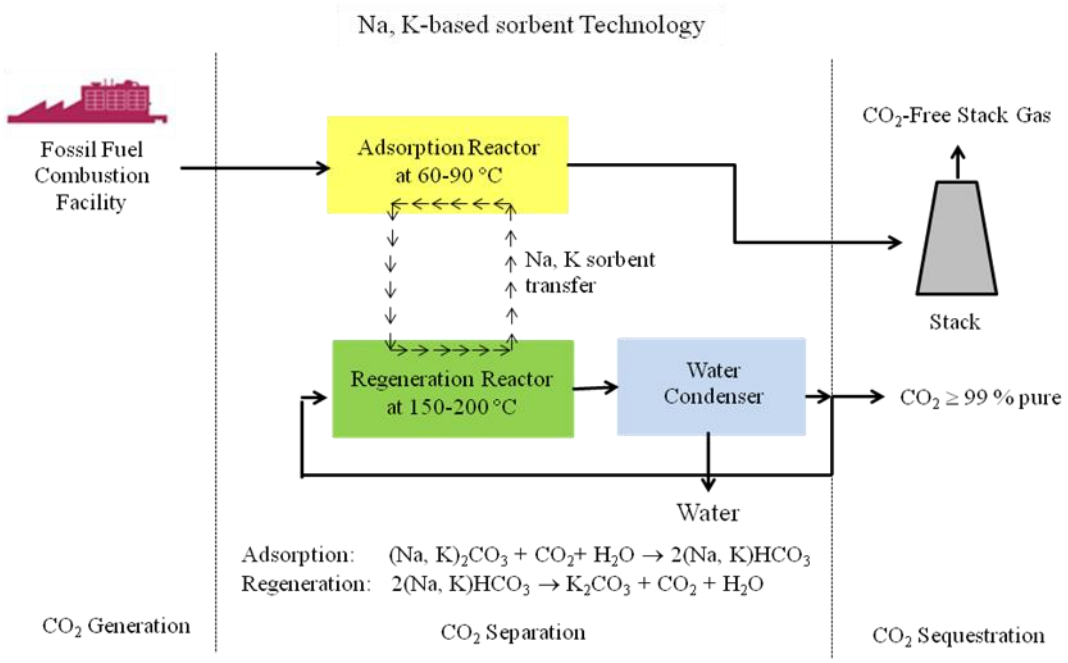


**Figure 2.5. Schematic of $CO_2$ cature from flue gas using Na, K carbonate-base sorbent processs** [33]**.**

### 2.2.2 Gas-liquid Membranes Absorption Technology

Membrane gas separation processes have been commercially used for $CO_2$ removal from natural gas at high pressure and high $CO_2$ concentration. Membrane is a thin barrier that allows selective permeation of some molecule from others as shown in Figure 2.6. The desired gas molecule in a feed mixture gas is allowed to pass through the barrier faster than the others. The desired gas is then absorbed on the membrane surface on one side usually at higher pressure [11]. The absorbed gas component penetrates into the membrane inside part, eventually reaching the other side where it can be desorbed under different specific conditions, such as lower pressure [34].

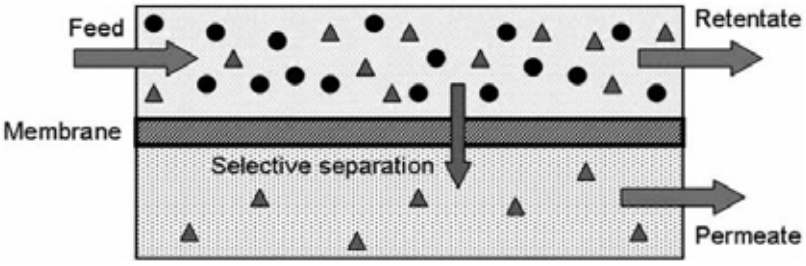


**Figure 2.6. Schematic of membrane gas separation** [35]**.**

Membrane gas separation have been widely used in two main $CO_2$ removal applications such as natural gas sweetening and enhanced oil recovery (EOR), since these applications have high $CO_2$ contents. On the other hand, $CO_2$ content in flue gas are far fewer in number because low $CO_2$ partial pressure in the flue gas provides a low driving force for gas separation resulting in higher energy supplies on the system efficiency compared to a standard process [36, 37, 38]. The presence of fly ash and impurity components such as $SO_x$, $NO_x$, HCI and HF also creates potential complications. The increase of efficiency for gas membrane separation can be reached by improving the selectivity of the process.

A hybrid membrane-absorbent system is currently receiving the most attention for flue gas $CO_2$ recovery due to higher selectivity [39]. This option has been called membrane contactor or gas-liquid membrane absorption. Membrane contactors are devices that achieve gas/liquid or liquid/liquid mass transfer without dispersed one phase within another. In a gas-liquid membrane contactor, the membrane acts as an interface between the feed gas and the absorption liquid. In the case of $CO_2$/exhaust gas separation as shown in Figure 2.7, $CO_2$ diffuses from the feed gas side through the membrane and is then absorbed in the selective absorption liquid. The loaded liquid circulates from the absorber to the desorber, which can be a traditional stripper or a

second membrane contactor, where desorption of $CO_2$ occurs. In general, the membrane is not involved in the separation process. In the case of porous membranes, gaseous components diffuse through the pores and are absorbed by the liquid. For non-porous membranes, the gas first dissolves into the membrane and then diffuses through the membrane due to a driving force. The contact surface area between gas and liquid phase is maintained by the membrane and is independent from the gas and liquid flow rate.

The selectivity of the process is not only determined by the absorption liquid, but also the membrane can play a significant role and contribute to the selectivity [41]. The membrane selectivity for different gases is generally related to the nature of the material. There are many different types of membranes used for $CO_2$ capture system application, for example, polymeric, metallic, ceramic etc.

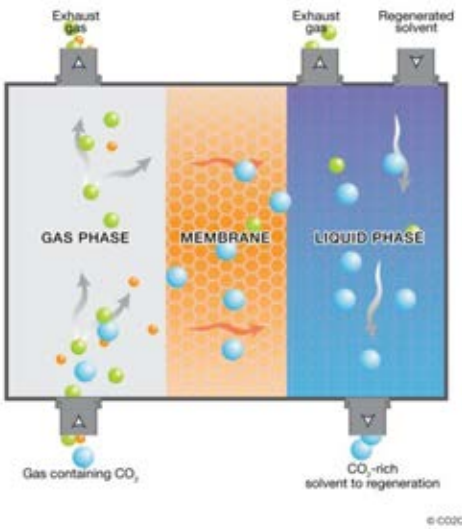


**Figure 2.7. Schematic representation of a membrane contactor for the separation of $CO_2$** [40]**.**

Gas-liquid membrane adsorption have many potential advantages over conventional $CO_2$ capture technologies, such as larger contact area per unit volume, larger treatment capacity and easy scale-up [42] Moreover, one attractive property of gas-liquid membrane absorption is the lower amount of energy required compared to other $CO_2$ capture methods. However membranes have not been developed for the large volume of gas separation such as for $CO_2$ capture of flue gas. They cannot achieve high purity product in one stage. Thus, multiple stages or recycle are necessary. This leads to the increase of complexity, energy consumption and costs [37]. The development is required before the membranes could be used for a large-scale $CO_2$ capture in fossil fuel combustion.

### 2.2.3 Cryogenic Technology

$CO_2$ capture with cryogenic is the method that can separate components according to their different boiling temperature. Consequently, the components can be cooled until they are separated into different phases. Since 1950s, the cryogenic technology has been used to produce liquid natural gas. Currently, the cryogenic separation is widely developed commercially for purification of $CO_2$ from streams that already provide high $CO_2$ concentration [43].

The cryogenic is technology that is operated at ultra-low temperature (lower than -100ºC) and high pressure. A process of cryogenic $CO_2$ capture from flue gas can be divided into 3 main steps such as compression, cooling and expansion as shown in Figure 2.8. First, the $CO_2$-rich flue gas is passed through the filtering and compressing part to increase the gas pressure. During this step, contaminants, including water are removed. The compressed $CO_2$ rich-flue gas is then cooled in the cooling and

expansion step to cryogenic temperature of $CO_2$ approximately -78 °C. The $CO_2$ gas condenses to liquid and then is separated from gas phase in a distillation comlumn.

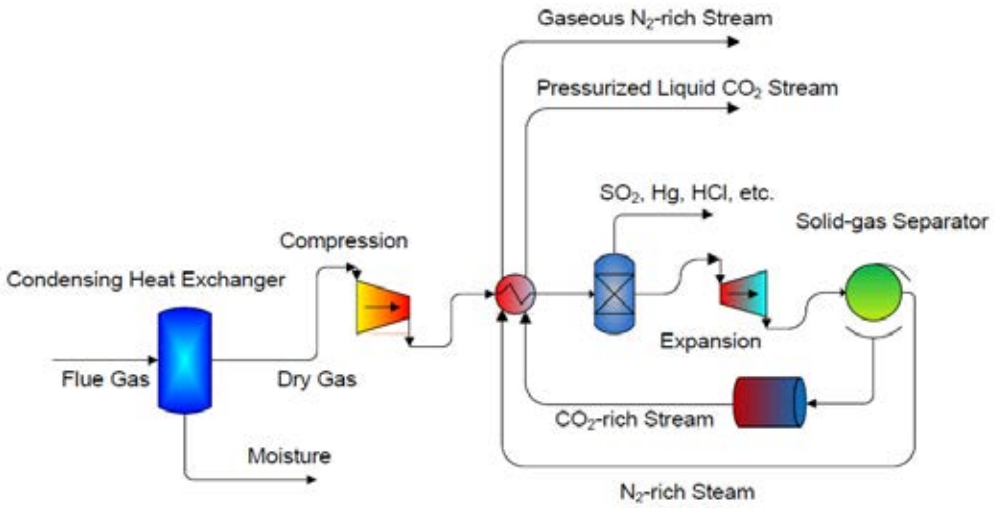


**Figure 2.8. Schematic diagram of the cryogenic carbon capture process** [44]**.**

The cryogenic separation can separate gases into very pure stream and enables direct production of liquid $CO_2$, which is a key advantage for economic transport. Therefore, this technique is receiving attention to be developed for $CO_2$ capture in case of fuel combustion. However, this process is still in pilot-scale stage as post-combustion system due to low $CO_2$ content, resulting in the high required energy for refrigeration. At present, the cryogenic technology is commercially used to remove $CO_2$ in the oxy-fuel combustion and pre-combustion systems, since these two systems are high $CO_2$ contents in the feed gas.

As a conclusion of this chapter regarding $CO_2$ Capture technology, after careful consideration and evaluation of potential technologies for post-combustion system, $CO_2$ capture with chemical adsorption with regenerable alkaline-based solid sorbent has been selected to be investigated in this research for following reasons:

- Post-combustion capture is easy to set up with typical fossil fuel power plant without requiring extensive change.
- Post-combustion offers flexibility, even if the $CO_2$ capture section fails, the power plant still can operate. On the contrary, the other two capture systems including oxy-combustion and the pre-combustion, the plant must shut down when $CO_2$ capture section fails.
- The chemical adsorption with regenerable alkaline-based solid sorbent is effective to capture $CO_2$ from flue gas at low pressure with low $CO_2$ concentration (typically 3-15 vol.%). Neither the membrane nor the cryogenic are well suited for oxy-combustion and pre-combustion.
- Flue gases from coal combustion will include not only $CO_2$, $N_2$, $O_2$ and $H_2O$, but also several types of contaminant including $SO_x$, $NO_x$, HCl, HF and particulate matters. Figure 2.9 shows a general schematic of a coal-fired power plant in which includes a section of air pollutant emission control unit with contaminants removal prior to $CO_2$ capture process. The flue gases emitted from this unit contains only $CO_2$, $N_2$ and moisture with temperature approximately 40-80°C. It represents highly suitable conditions to operate $CO_2$ capture with alkaline-based chemical adsorption. Moreover, with such conditions, it is not required to supply external heat for adsorption or remove water from the stream.

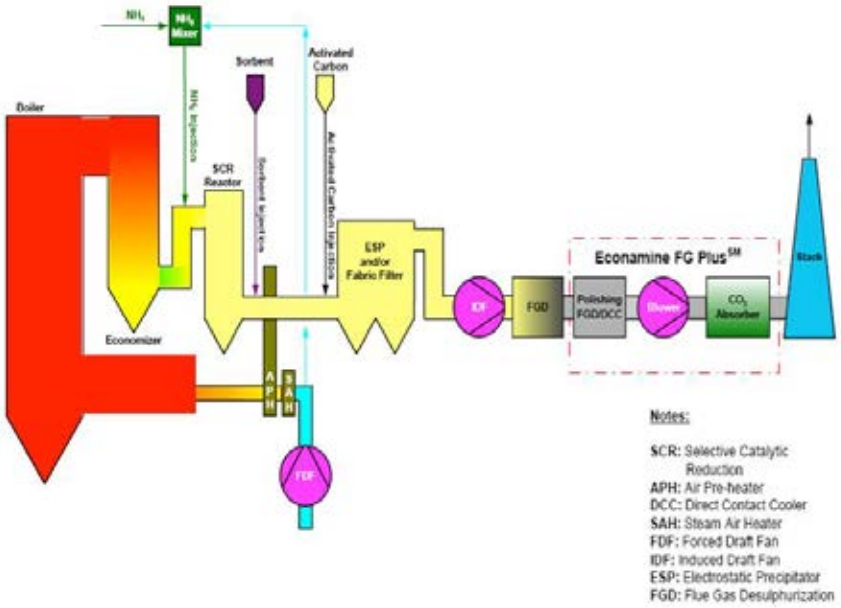


**Figure 2. 9. General schematic of coal-fired combustion power plant with post-combustion $CO_2$ capture system and other emission controls** [45].

- The alkaline-based solid sorbent can be regenerated at low temperature which brings a highly cost-effective process.
- The reaction between $CO_2$, $H_2O$ and potassium carbonate is an exothermic reaction and the regeneration is an endothermic one. Heat will be an important factor to control the process to prevent hot spot creation during carbonation reaction and to minimize energy consumption. In consequence, the fluidization technique can be a good solution for this process since it is ideal contacting device for solid-gas systems. Reactions between solids and gas streams, such as adsorption and desorption reactions, are greatly enhanced by the excellent mixing of the reactants through the fluidized bed. Therefore, the fluidization theory was described in next section of this study.

## 2.3 Fluidization

Fluidization is defined as a process in which the solid particles are converted from a static solid-like state to a fluid-like state. This process takes place when a gas or a liquid is passed through the granular solid particles. When there are no gas or liquid passing through, the granular solid particles is pulled down by only gravitational force and flow downward. When the gas or liquid flow starts to be introduced through the bottom of column, it also introduces drag force that encounters with gravitational force. Under the fluidizing state, the upward drag forces will counterbalance the downward gravitation forces. Thus the granular solid particles become semi-suspended within the gas or liquid. The fluidization of granular particle bed allows for high heat and mass transfer rates between the gas or liquid phase and the solid phase, large effective gas/solid surface, ease of solids handling, rapid mixing and applicable for large or small scale operation . Therefore, many applications of fluidization are utilized as given in Table 2.1

**Table 2.1 Industrial applications of fluidized bed** [46]**.**

| Industrial types | Applications |
|---|---|
| Polymeric Materials | Gas phase polymerization of polyethylene |
| | Production of silicon for the semi-conductor industry |
| Biochemical | Cultivation of microorganisms for the food and pharmaceutical industries |
| Chemical Systhesis | Phthalic anhydride |
| | Fischer-Tropsch synthesis of hydrocarbons |
| | Acrylonitrile, maleic anhydride, activated carbon, calcinations, roasting of sulfide ores, chlorination, reduction |
| Petroleum Processing | Fluid catalytic cracking for production of gasoline from oil |
| | Coal gasification |
| | Thermal cracking of naphtha petroleum fraction to produce ethylene and propylene |
| | Fluid coking |
| Combustion | Coal combustion |
| | Solid waste incineration |
| | Stem raising |
| Physical Operations | Coating metal objects |
| | Drying of solids |
| | Adsorption of solvents |

## 2.4 Regimes of Fluidization

When increasing gas velocity through a bed of granular solid, the gas-solid contact behavior changes in many types as shown in Figure 2.10. Several flow patterns/regimes have been determined with the increase of gas flow velocity such as fixed bed, bubbling fluidization, slugging fluidization, turbulent fluidization, fast fluidization and homogenous dilute transport regime. When the gas velocity starts to be fed through a bed, for low gas velocity, granular solids stay in stationary phase. This type of bed is called fixed bed. When gradually increasing gas velocity to a certain velocity, granular solid starts to move and moreover the solid are arranged in array. When increasing gas velocity further, the solid are separated independently from each other. This is the onset of fluidization behavior. After this point, the bed height is increased by increasing the gas velocity. For low gas velocity, the solid in the bed are still close to each other. This behavior is called “Dense-phase fluidized bed”. When increasing the gas velocity, the solid is almost slipped out from the bed by gas. This is identified as “Dilute-phase fluidized bed”. Moreover, when the gas velocity becomes so high, the solids are entrained from the bed. This behavior is used to carry solid from one place to the other place.

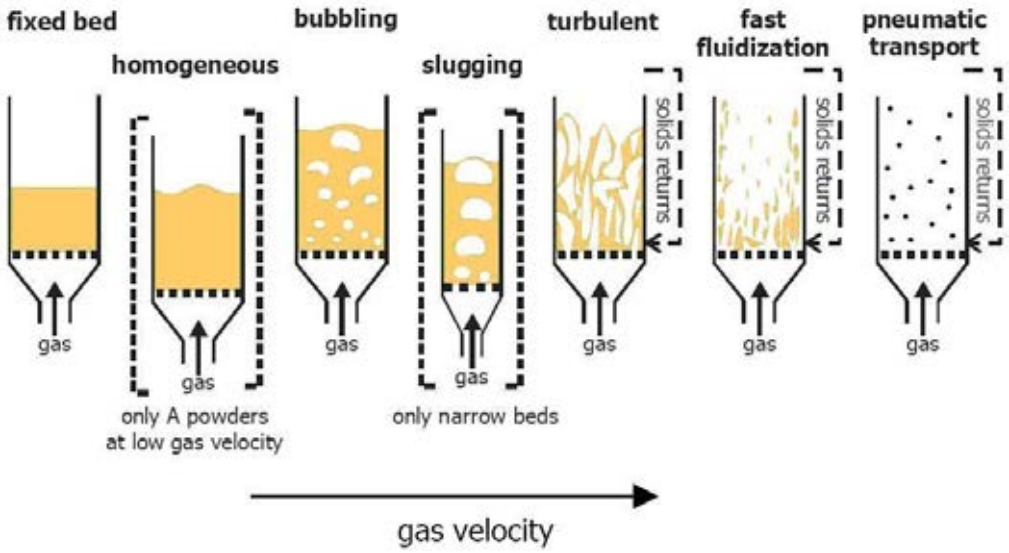


**Figure 2.10. Flow patterns in gas-solid fluidized bed** [47]**.**

### 2.4.1 Fixed Beds

A fixed or packed bed is observed for a column where particles remain stable in stationary phase while a gas is feeding. When there is no gas flow through a bed, there is only gravitational force to act on solid in downward direction. When the gas flows through the bed, it exerts a drag force or friction force on the particles, resulting in a pressure drop across the bed. The drag forces act upward and counter balance with the gravitational force. For a fixed bed, the pressure drop is directly proportional to gas velocity. There are many proposed equation for pressure drop across the bed. The equation of Ergan (1952) is suitable to calculate pressure drop across fluidization [48]. Ergan (1952) proposed the equation presenting the relation of pressure drop per unit height of a fixed bed ($\Delta P/L$) of uniformly sized particles ($d_p$). The Ergan equation is written as:

$$\frac{\Delta P}{L} = 150\frac{(1-\varepsilon)^2}{\varepsilon^3}\frac{\mu U}{(\phi d_p)^2} + 1.75\frac{(1-\varepsilon)}{\varepsilon^3}\frac{\rho_g U^2}{\phi d_p} \qquad (2.5)$$

Where, $\varepsilon$ is the void fraction in the bed, $\phi$ is the sphericity of bed solids, $\mu$ is the dynamic viscosity, and $\rho_g$ is the density of the gas. The superficial gas velocity, U is defined as the gas flow rate per unit cross section of the bed.

### 2.4.2 Bubbling Fluidized Bed

From Figure 2.9, it is found that when increasing gas velocity through the fixed bed, until the velocity reaches a critical value. The bed changes from fixed bed to bubbling fluidized bed. This is known as minimum fluidization velocity ($U_{mf}$). The Figure 2.11 shows the pressure drop and bed height gradient with gas velocity up to and after the minimum fluidization velocity. For gas velocity lower than $U_{mf}$, as the gas velocity increases, the pressure drop due to the fluid drag force rises while bed height remains constant. At the minimum fluidization velocity or the point B in Figure 2.11, the height bed starts to expand while the pressure drop levels off and no longer increase with increasing gas velocity. At the minimum fluidization velocity, the drag force of solid is equal to the net weight of the bed and the solid in the bed perform like fluid. When gas velocity becomes higher than the minimum fluidization velocity, the expansion of bed height continues to increase, but the pressure drop remains constant.

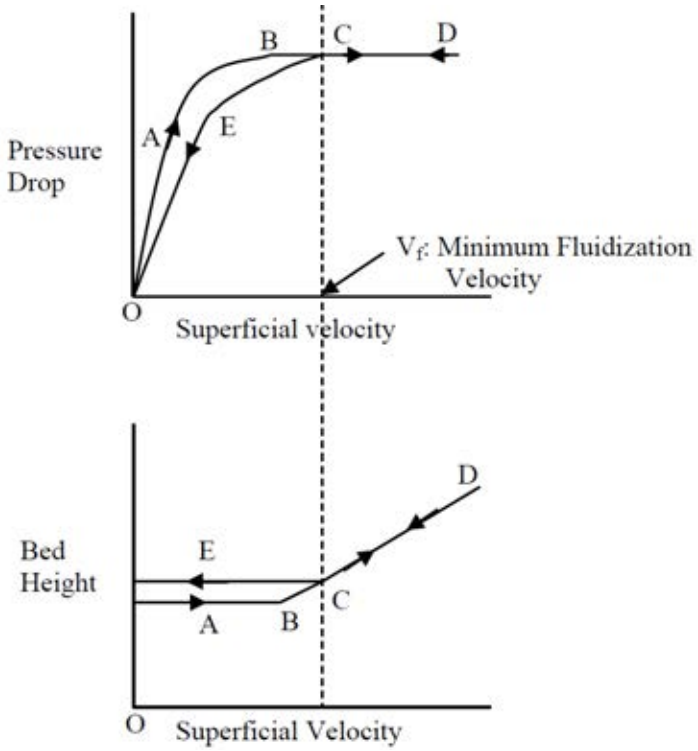


**Figure 2.11. Pressure (a) and bed height (b) gradient with superficial velocity up to and after fluidization** [49]**.**

The minimum fluidization velocity has been widely studied and there are many available equations to predict this velocity. Among these equations, the correlation of Wen and Yu (1966) is generally used to calculate the minimum fluidization velocity [50]. The Wen and Yu correlation is written:

$$\mathrm{Re}_{mf} = \frac{U_{mf} d_p \rho_g}{\mu} = [27.2^2 + 0.0408 Ar]^{0.5} - 27.2 \qquad (2.6)$$

Where Archimedes number,

$$Ar = \frac{\rho_g (\rho_s - \rho_g) g d_g^3}{\mu^2} \qquad (2.7)$$

Several researchers proposed methods for the determination of the minimum fluidization velocity. To evaluate the minimum fluidization velocity by traditional method, pressure drop across the bed were obtained for several different gas velocities

as shown in Figure 2.11. The minimum fluidization velocity is obtained from the intersection of two straight lines depicted in the experimental curves [51]. The traditional method is insufficient for online monitored process. In 1985, Puncochar proposed a methodology to determine the minimum fluidization gas velocity. It is based on the relation of standard deviation of pressure fluctuation and gas velocity. The minimum fluidization gas velocity is obtained at the intersection of the regression line with the gas velocity axis [52].

A bubbling fluidized bed is believed to contain two different phases including bubbles and emulsion as shown in Figure 2.12. The small bubbles form at the bed bottom and grow mostly by coalescence. The bubbles will rise to the surface and break down.

The onset of bubbling regime has been found to be a strong function of particle properties. For solid in Group B and D Geldart's classification (see section 2.5), the onset gas velocity for bubbling regime is equal minimum fluidization velocity. A fluidized bed of Group A Geldart's classification (see section 2.5) does not start bubbling when the gas velocity reaches the minimum fluidization velocity. The bubbles start to appear when the gas velocity is increased up to another gas velocity called minimum bubbling velocity, $U_{mb}$. The regime of solid at the gas velocity between minimum fluidization velocity and minimum bubbling velocity is known as bubble-free fluidization regime [43]. The minimum bubbling velocity for Group A particles is estimated by the Geldart and Abrahamsen (1978) as:

$$U_{mb} = 2.07 \exp(0.716F) d_p \left[ \frac{\rho_g^{0.06}}{\mu^{0.347}} \right] \qquad (2.8)$$

Where F is the mass fraction of particles less than 45 μm, $d_p$ is the mean solid diameter of particles in m, $\rho_g$ is the gas density in kg/m$^3$ and μ is the viscosity of gas in kg/m sec.

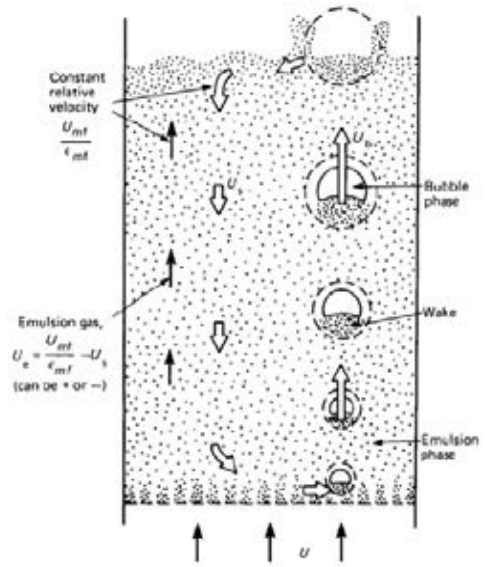


**Figure 2.12. Bubbling fluidization flow pattern** [54]**.**

### 2.4.3 Slugging Fluidization

A Slug is a bubble whose size of diameter is comparable with the bed itself. This phenomenon is called slugging. As the bubble size increases, the effect of the wall becomes greater, and because of this, effect of slug on the solid in column shows a different effect than that of the bubbles. Normally the slugging fluidization occurs in narrow and deep bed with respect ratio (ratio between height of bed and diameter column) higher than 1. There are three necessary conditions for slugging [55].

The maximum stable bubble size, $D_{bmax}$, must be greater that 0.6 times the diameter of the bed (Geldart, 1986 [56]), the bed height must exceed a minimum height.

The gas velocity must exceed the minimum slugging velocity, $U_{sl}$, given by Stewart and Davidson, 1967 [57]

$$U_{sl} = U_{mf} + 0.07(gD)^{0.5} \qquad (2.9)$$

The criterion for slug formation at choking, where a sudden change in the solids holdup occurs in a gas-solid fluidization system, given by Yang (1976) [58] ($U_t^2$/gD) must exceed 0.123 as shown in Equation (2.10)

$$\frac{U_t^2}{gD} \geq 0.123 \qquad (2.10)$$

Where $U_t$ is the terminal velocity of the average-sized solid in m/s, D is the diameter of column in m and g is gravitational acceleration (m/s$^2$).

### 2.4.4 Turbulent Fluidization

The turbulent fluidization flow regime is commonly defined for flow between bubbling fluidization and the fast fluidization regimes [59]. When gas velocity passing through a bubbling fluidization reaches above the minimum bubbling fluidization (equivalent to the onset of bubbling for Group A particles) or the minimum fluidization velocity corresponding with beginning of bubbling for Group B and D particles, the bed expansion starts to take place. If gas velocity continues to increase, the bed expansion may change the pattern from bubbling to a new regime called a turbulent. Over this transition, the large bubble/slug erupts into small void due to rapid coalescence and breaks down the bubbles alternately. Effect of this

phenomenon on the bed behavior is the increase of bed expansion due to the fact that fine particles are splited by bubble/slug eruption. Fine particles were elutriated from the bed and the amount of particles in the free board zone increased with the increase of the gas velocity. Therefore, the top surface of the bed is difficult to distinguish.

Figure 2.13 shows that the amplitude of pressure fluctuation across the bed increases as the bed approaches turbulent fluidization. The pressure drop across a turbulent bed fluctuates drastically. When increasing gas velocity through turbulent bed, the amplitude of pressure fluctuation is magnified to a certain value. Beyound this point, it gradually decreases with the increasing of gas velocity.

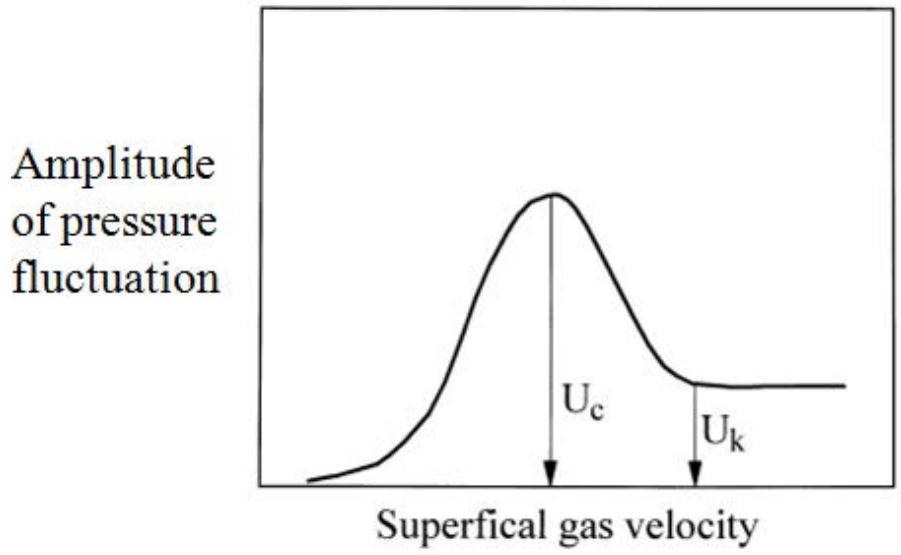


**Figure 2.13. The amplitude of pressure fluctuation across the bed increases as the bed approaches turbulent fluidization [60].**

Two different onset velocities are commonly used to distinguish the difference between bubbling and the turbulent regimes as shown in Figure 2.13. The first onset

velocity defines a transition velocity ($U_c$), where the pressure standard deviation reached a maximum value [61]. $U_c$ is said to be the gas velocity that reflects predominant of the bubble coalescence and eruption. A second velocity used to determine transition from bubbling to turbulent regime is based on a critical velocity ($U_k$) where the standard deviation starts to be steady while increasing gas velocity as shown in Figure 2.13. This behavior means that bubble coalescence and eruption become stabilized, with only small dispersed voids certain [61].

Several researchers claimed that $U_c$ and $U_k$ values are sensitive to several factors such as column diameter, probe location, gas density, temperature, particle size distribution, pressure fluctuation measurement technique and investigators that may observe the different experiment result. Therefore, a number of investigators have developed the correlation equation to predict the $U_c$ and $U_k$ as listed in Table 2.2 and 2.3.

The turbulent fluidization is generally used in the industrial application because high gas-solid contact, high dispersion coefficient for the solid and high back-mixing [62].

**Table 2.2 Correlation for transition velocity, $U_c$**

| Researchers | Correlations | No. |
|---|---|---|
| Yerushalmi and Gankurt (1979) [61] | $U_c = 3.0(\rho_p d_p)^{0.5} - 0.77$ | (2.11) |
| Yang (1984) [63] | $U_c = U_t \varepsilon_e^m$<br>$U_t = U_t \, \mathrm{Re}_t^{-0.485}$<br>$\varepsilon_e = (m-1)/m$<br>$m = 2.31 \mathrm{Re}_t^{-0.0547}$ | (2.12) |
| Jin et al.,(1986) [64] | $\frac{U_c}{\sqrt{g d_p}} = \left( f \frac{D_t}{d_p} \frac{\rho_s - \rho_g}{\rho_g} \right)^{0.27}$<br>$fD_t = 0.00367$(for bed without internals)<br>$fD_t = 0.00232$(for bed with vertical tubes)<br>$fD_t = 0.00032$(for bed with pagoda typebaffles) | (2.13) |
| Lee and Kim (1988) [65] | $\mathrm{Re}_c = 0.700 Ar^{0.485}$ | (2.14) |
| Leu, Huang and Gua (1990) [66] | $\mathrm{Re}_c = 0.568 Ar^{0.578}$ | (2.15) |
| Horio (1991) [67] | $\mathrm{Re}_c = 0.936 Ar^{0.472}$ | (2.16) |
| Nakajima et al., (1991) [68] | $\mathrm{Re}_c = 0.663 Ar^{0.467}$ | (2.17) |
| Dunham et al., (1993) [69] | | (2.18) |
| | $\mathrm{Re}_c = 1.201 Ar^{0.386} (H/D_t)^{0.128 \ln(\rho_p d_p) + 0.264}$<br>for Group A and B particles<br>$\mathrm{Re}_c = 1.027 Ar^{0.450} (H/D_t)^{0.128 \ln(\rho_p d_p) + 0.264}$<br>for Group D particles | (2.19) |
| Bi and Grace (1995) (DPF data) [70] | $\mathrm{Re}_c = 1.243 Ar^{0.447}$ | (2.20) |
| Bi and Grace (1995) (APF data) [70] | $\mathrm{Re}_c = 0.565 Ar^{0.461}$ | (2.21) |
| Chehbouni et al., (1995) [71] | $U_c / \sqrt{g D_t} = 0.463 Ar^{0.145}$ | (2.20) |

**Table 2. 3 Correlation for critical velocity, $U_k$**

| Researchers | Correlations | No. |
|---|---|---|
| Yerushalmi and Cankurt (1979) [72] | $U_k = 7.0(\rho_p d_p)^{0.5} - 0.77$ | (2.21) |
| Horio (1991) [73] | $Re_k = 1.41 Ar^{0.56}$ for $Ar < 10^4$ | (2.22) |
| | $Re_k = 1.46 Ar^{0.472}$ for $Ar > 10^4$ | (2.24) |
| Bi and Fan (1992) [74] | $Re_k = 0.601 Ar^{0.695}$ for $Ar < 125$ | (2.25) |
| | $\mathrm{Re_k} = 2.28 Ar^{0.419}$ for $Ar > 125$ | (2.26) |
| Tsukada et al. (1993) [75] | $\mathrm{Re_k} = 1.31 Ar^{0.45}$ | (2.27) |

### 2.4.5 Fast Fluidization Regimes

The fast fluidized bed regime has been investigated over the past 20 year [72]. Phenomenon occurring during the fast fluidization has been defined by several investigators. Yerushalmi and Cankurt defined that the fast fluidization regime exists for gas velocity above the minimum transport velocity with variation of solid circulation rate ($G_s$). Li and Kwauk [73] proposed the fast fluidization regime has the axial variation of average cross-sectional voidage in the riser from dense to dilute. This is called S-shaped profile. Takeuchi [76] reported that the fast fluidization should contain both the dense phase at the bottom and dilute entrained phase at the dilute region. At the dilute region, the cross-section solid-hold up distribution has an exponential profile. This implies that there are two behaviors that occur in this region such as downward flow of solid near the wall and upward flow of gas-solid at the core region. This is known as core-annulus flow structure. From previous research, the definition of fast fluidization has been far from consistent. However, the compromise results are that fast fluidization denotes other type of bubbleless gas-solid contact, mainly characterized by the solid aggregation into clusters as shown in Figure 2.14. The cluster particles move downward mostly near the wall region, while gas and entrained particles move upward in the core region. The bed surface is difficult to characterize when particles are removed out at the top of the riser. During the fast fluidization solids must be added near the bottom to replace the entrained particles moving out from the riser.

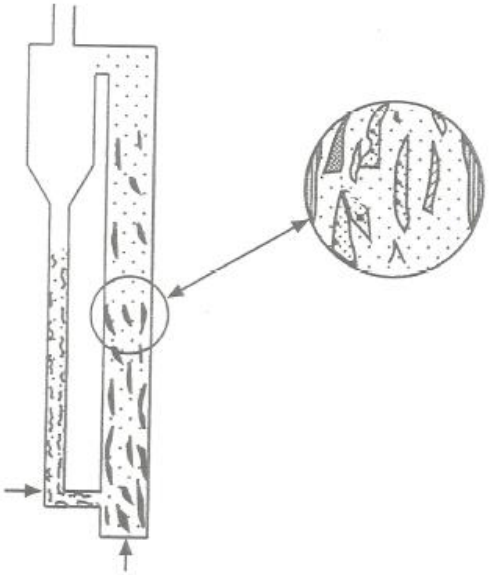

**Figure 2.14. A fast fluidization is composed by solid agglomerates** [74]**.**

The transition from the turbulent to fast fluidization takes place at the transport velocity, $U_{tr}$, where the solid start to be transported and carried out from the top of the column by gas. Several techniques have been used to determine transport velocity. Table 2.4 shows available methods for determining transport velocity.

**Table 2.4 Available methods for determining transition from turbulent to fast fluidization**

| Authors | Methods |
|---|---|
| Yerushalmi and Cankurt (1979) [53] | $\Delta P/\Delta L$- $G_s$ phase diagram |
| Yersushalmi and Cankurt (1979) [53] | Flooding point method |
| Yersushalmi and Cankurt (1979) [53] | $\Delta P/\Delta L$- Ug phase diagram |
| Schnitzlein and Weinstein (1988) [66] | Maximum Gs versus U |
| Parales (1991) [67] | Emptying time of decay of bed particle (blow out) |

According to the measurements of initial $\Delta P/\Delta L$- $G_s$ phase diagram, transport velocity is estimated by observing pressure drop gradient when solid circulation rate is varied at given gas velocities in the column [61]. The transport velocity is defined

as gas velocity where the pressure drop gradient is dependent on upon. Yersushalmin and Cankurt derived ΔP/ΔL- $U_g$ phase diagram from ΔP/ΔL- $G_s$ phase diagram. For derived ΔP/ΔL- $U_g$ phase diagram, the transport velocity is based on a plot of the pressure drop gradient across the riser bottom versus gas velocities at different solid circulation rates. The transport velocity is the lowest gas velocity for which the pressure drop gradient starts to depend on the solid circulation rate [77]. The flooding point method use to define the $U_{tr}$ by examining the relationship between gas velocity and solid volumetric flux at different particle densities and their intersection [61, 78]. Schnitzlein and Weinstein method fixed the gas velocity and determines the maximum value of solid circulation rate to obtain a stable regime of maximum carry-over [65]. The emptying time method proposed by Parales has been commonly used to determine the transport velocity due to simple and quick measurement. The emptying time is based on the time required for all solid particles to leave the bed as function of gas velocity [61, 78]. Several correlations between two dimensionless groups including Reynolds number for the transport velocity ($Re_{tr}$) and Archimedes number (Ar) have been developed to predict the transport velocity, $U_{tr}$, as listed in Table 2.5.

**Table 2.5 Correlations for transport velocity, $U_{tr}$**

| Authors | Correlations | No. |
|---|---|---|
| Lee and Kim (1990b) [79] | $\mathrm{Re}_{tr} = 2.916 Ar^{0.354}$ | (2.28) |
| Perales et al. (1991) [75] | $\mathrm{Re}_{tr} = 1.415 Ar^{0.483}$ | (2.29) |
| Bi and Fan (1992) [80] | $\mathrm{Re}_{tr} = 2.28 Ar^{0.419}$ | (2.30) |
| Adanez et al. (1993)[81] | $\mathrm{Re}_{tr} = 2.078 Ar^{0.458}$ | (2.31) |
| Tsukada et al. (1994) [82] | $\mathrm{Re}_{tr} = 1.806 Ar^{0.458}$ | (2.32) |
| Chehbouni et al. (1995) [83] | $\mathrm{Re}_{tr} = 0.169 Ar^{0.545} (D_t / d_p)^{0.3}$ | (2.33) |

At gas velocity over the transport velocity, $U_{tr}$, three solid concentration distributions can be described: a constant dilute profile in the dilute regime, an S-shaped profiled (as shown in Figure 2.5) in the fast fluidization regime and a constant and dense profile in the dense regime ($1-\varepsilon \approx 0.2$). When the gas velocity through the fast fluidization is increased, the gas velocity reaches a critical value known as the minimum pneumatic velocity, $V_{mp}$. At this velocity, the fast fluidization transforms to a homogeneous dilute bed which S-shaped profile of solid concentration in the column is absent. It is difficult to detect this minimum pneumatic velocity experimentally. A Correlation was proposed by Bi (1995) [70] to estimate this velocity given by:

$$V_{mp} = 10.1(gd_p)^{0.347}\left(\frac{G_s}{\rho_s}\right)^{0.310}\left(\frac{d_p}{D_t}\right)^{-0.139} Ar^{-0.021} \qquad (2.34)$$

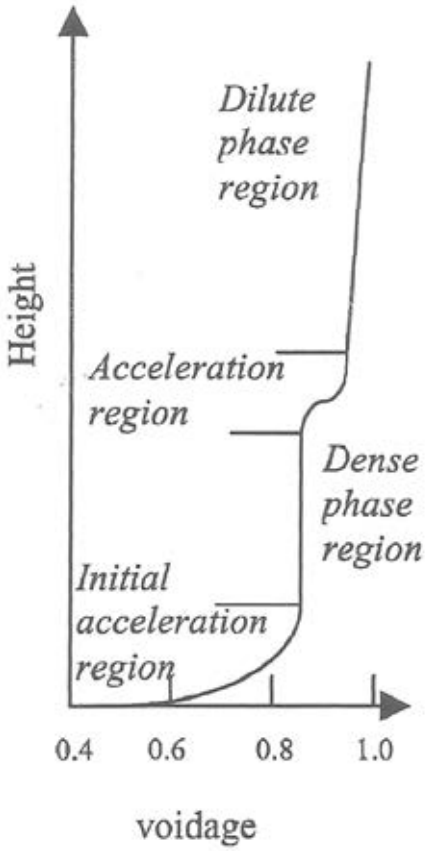


**Figure 2.15 S-shaped axial solid concentration profile of fast fluidization regime** [72].

## 2.5 Solid Properties

Geldart (1973) [84] classified powders into four groups according to their fluidization properties at ambient conditions. Figure 2.16 shows Geldart's classification of the fluidization behavior of powders. As seen in Figure 2.16, there are 4 major groups:

**Group A or aeratable**: it is characterized by particle with diameter range of 30-100 μm and the density is lower than 1.4 g/cm$^3$. This particle is smoothly and easily fluidized. The onset gas velocity of bubble fluidization is considerably larger than minimum fluidization velocity. The bed expands considerably before bubbling occurs. The bubble size depends on the particle size distribution and average particle diameter. There is maximum bubble size. Gross solid circulation is occurs. Major example is the FCC catalyst, milk flour.

**Group B or bubbling**: the particle diameter is in the range of 100-1000 μm and the density is about 1400-4000 kg/m$^3$. The Group B particles can produce large bubbles or may form slugs. The bubbles fluidization velocity and minimum fluidization velocity are almost identical. The bubble size is almost independent of the mean particle diameter and the particle size distribution. The maximum bubble size is no observable. Gross solid circulation is occurs. Main example is sand, glass bead.

**Group C or cohesive**: these particles are considered very fine powder less than 30 μm. Normal fluidization is difficult for these solids because of high interparticle force influence. These particles may form only channels. Examples: Face powder, flour, and starch.

**Group D or spoutable:** the particles are either large and/or dense particles ($d_p$ ~ > 1000 μm). The bubbles coalesce rapidly and become large. Examples include drying grains, peas, roasting coffee beans, gasifying coals and roasting of metal ores.

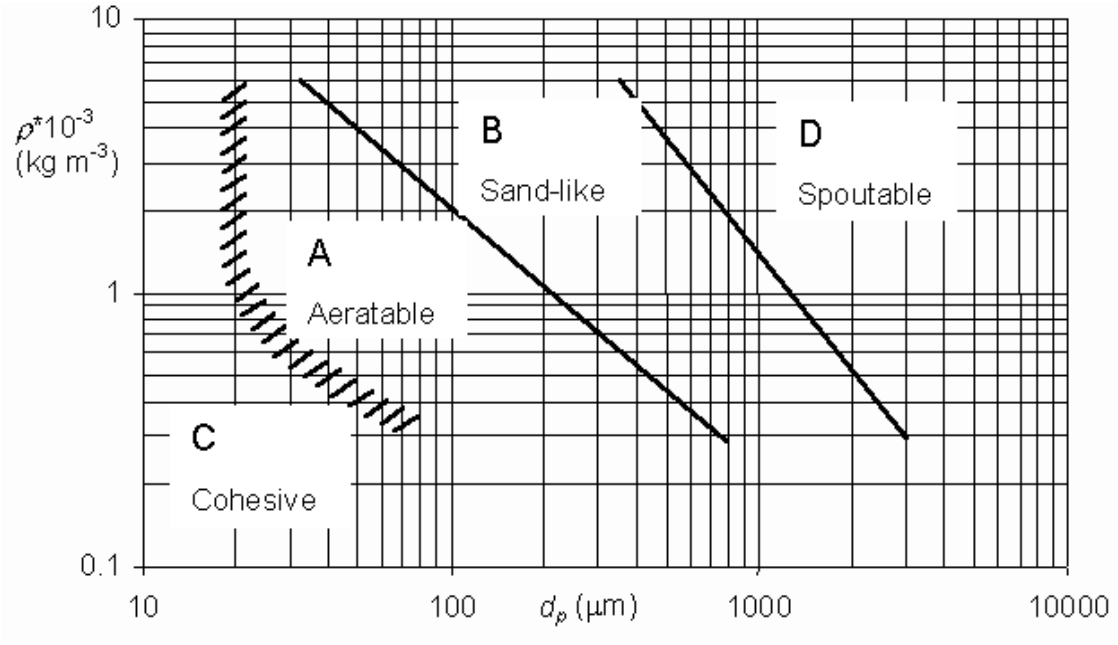


**Figure 2.16. Geldart's classification diagram of powder** [85]**.**

## 2.6 Literature Reviews

There are many research works devoted to $CO_2$ sorption and hydrodynamics in a circulating fluidized bed.

**$CO_2$ capture**

**Sharonov V. et al., (2004)** [86] studied the kinetics of the $CO_2$ sorption by a composite sorbent of $K_2CO_3$ on $Al_2O_3$ in gradientless adsorber with a diameter of 0.006 m and a height of 0.07 m at 297 K. It can be found that the order of the sorption rate with respect to the $CO_2$ concentration is n = 1.04± 0.07. The sorption rate constants were calculated for the sorbent grains of various sizes. It was shown the

dynamic sorption capacity was obtained as function of the $CO_2$ concentration. The maximum sorption capacity was found to be 83 mg of $CO_2$ per 1 g of the sorbent.

**Lee S.C. et al., (2005)** [87] studied the $CO_2$ capture capacities and regeneration properties of several $K_2CO_3$-based sorbents and the change in the physical properties of the sorbents before/after $CO_2$ adsorption. The $K_2CO_3$-based sorbent were prepared by impregnation of $K_2CO_3$ on several supporter such as activated carbon (AC), $TiO_2$, $Al_2O_3$, MgO, CaO and $ZrO_3$. The $CO_2$ capture capacity and regeneration property were measured in fixed-bed reactor. It can be concluded that the $K_2CO_3/Al_2O_3$, $K_2CO_3$/CaO and $K_2CO_3$/MgO sorbent formed new structures such as $KAl(CO_3)_2(OH)_2$, $K_2Ca(CO_3)_2$, $K_2Mg(CO_3)_2$, and $K_2Mg(CO_3)_2 \bullet 4(H_2O)$, which were not completely converted to the original $K_2CO_3$ phase at temperature below 200 °C, during $CO_2$ adsorption. In case of $K_2CO_3$/AC, $K_2CO_3/TiO_2$ and $K_2CO_3/ZrO_3$, a $KHCO_3$ was formed during $CO_2$ adsorption. It was possible to regenerate them even within a low temperature range (130-150 °C). In particular, the $K_2CO_3/TiO_2$ sorbent showed excellent characteristics with respect to $CO_2$ adsorption and regeneration.

**Seo Y. et al (2007)** [88] studied the effect of $H_2O$ pretreatment on $CO_2$ adsorption using $K_2CO_3$ solid sorbent for understanding $CO_2$ capture characteristics of solid sorbent. The bubbling fluidized bed with an inner diameter of 0.05 m and a height of 0.8 m was used in this research. A dry sorbent sorbKX35, consists of $K_2CO_3$ for adsorption and supporters for mechanical strength. It can be observed that $H_2O$ pretreatment before reacting with simulated flue gas reveal increasing $CO_2$ removal. When $H_2O$ pretreatment time was long enough to covert $K_2CO_3$ into $K_2CO_3 \bullet 1.5H_2O$, $CO_2$ removal was excellent.

**Yi C-K. et al., (2007)** [89] investigated continuous operation of the potassium carbonate-based dry sorbent (Sorb KX35) $CO_2$ capture process with two fluidized-bed reactor included a fast fluidized carbonator of 6 m height and a bubbling fluidized regenerator . The parameters such as gas velocity, solid circulation rate, carbonation temperature, and water vapor content were carried out during several continuous operations. The performance of the dry sorbent $CO_2$ capture process was also investigated. It can be reported that the $CO_2$ removal increased as gas velocity decreased and as solid circulation rate was increased. The $CO_2$ removal range from 26% to 70% was rather sensitive to the water vapor content among other parameters.

**Park Y.C. et al. (2009)** [90] examined the effect of bed height on $CO_2$ capture in a bubbling fluidized bed reactor with a inner diameter of 0.05 and a height of 0.8 m. Potassium-based solid sorbent, SorbKX35T5 which consists of 35% $K_2CO_3$ and 65% supporters was used in this study. Four different ratio between length and diameter (L/D ratio) such as 1, 2, 3 and 4 were performed. As L/D ratio increased, the amount of $CO_2$ captured increased until L/D ratio was 3. However, $CO_2$ sorption capacity was decreased when L/D ratio further increased. The amount of $CO_2$ captured decreased when the number of cycles increased.

**Zhao C. et al., (2009)** [91] studied the effect of crystal structure of potassium carbonate on $CO_2$ capture characteristics in a TherMax 500 high-pressure thermogravimetric apparatus. There are two type of $K_2CO_3$ such as $K_2CO_3$ with structure of monoclinic crystal and $K_2CO_3$ with structure of hexagonal crystal in this study. Compared with hexagonal crystal structure, the particle morphology of monoclinic crystal structure is better for the carbonation reaction. However, the carbonation reaction activity of hexagonal crystal structure is better than that of

monoclinic crystal one. The crystal structure of $K_2CO_3$ with monoclinic structure and $K_2CO_3 \bullet 1.5H_2O$ are similar, while $K_2CO_3$ with hexagonal structure is same as $KHCO_3$. As observed with the difference in crystal structure, the conversion of monoclinic crystal to $K_2CO_3 \bullet 1.5H_2O$ is easier, whereas hexagonal crystal is easy to produce $KHCO_3$.

**Fluidized bed**

**Cui H. and Chaouki J. (2004)** [92] studied effect of bed temperature on the local two-phase flow structure FCC particles in 0.20 m-ID fluidized beds with bed temperature ranging from 25° to 420°C, covering both the bubbling and turbulent fluidization regimes. FCC particle has 78 μm of diameter and 1760 kg/m$^3$ of density. The results show that fluidization and fluctuations of the local two-phase flow structure become more intense with the increasing of bed temperature. At constant superficial gas velocities, the averaged local particle concentration, the dense phase fraction and particle concentration in the dense phase decrease with increasing bed temperature, whereas both the frequency of the dilute/dense duration ratio increase. In addition, fluidization behaviors of the FCC particles tested gradually shift from the Geldart A towards B with increasing temperature due to a decrease of the interparticle attractive forces and a increase of interparticle repulsive forces.

**Monazam E. R. et al., (2005)** [93] conducted a 0.3 m diameter and 10 m height circulating fluidized bed (CFB) cold model to evaluate the operating flow regimes and their transitions. Experiments were carried out at gas velocities from turbulent, through fast fluidization, and up to dilute-phase regimes. B Geldart Type, cork was used as solid bed. Transition velocities were found by analyzing the time required to empty out all solids from the riser of the CFB after cutting off solids flow.

The lowest transition velocity marked the transition between the dense-phase turbulent and the fast fluidization flow regimes, while a higher transition represented the transition between the fast fluidization and the dilute-phase flow regimes. Based on the results, the axial pressures along the riser exhibited markedly distinct profiles in each of the three different operating flow regime regions as defined by two transport velocities.

**Ellis N. et al., (2004)** [94] studied the effect of the columns diameter on the hydrodynamics of gas-solid turbulent fluidized beds with height of 4.5 m for FCC particles. The columns diameter used were; 0.26, 0.61 and 1.56 m. The FCC particle has diameter of 78 μm and density of 1560 kg/m$^3$. The superficial gas velocity, $U_c$, at which the onset of the turbulent fluidization flow regime occurs, was found to depend on the aspect ratio, H/D. The bed expansion depends on the configuration of the solid collection and return system. The normalized radial profile of time-mean voidage was less affected by column diameter than by the normalized superficial gas velocity, ($U/U_c$). For the local measurements, the breaks down of two phase flow structure occurred when $U>U_c$, however, the extent of this breaks down depends on the column diameter.

**Zhu H. and Zhu J. (2008)** [95] presented a comparison of flow structures in a newly designed circulating-fluidized bed (C-TFB), which has a high solids hold up and solids flux, with two commonly used fluidized beds reactors: circulating fluidized bed (CFB) and turbulent fluidized bed (TFB). Particles used in experiments were FCC catalysts with a diameter of 65 μm and a particle density of 1780 kg/m$^3$. Results indicated that the flow behaviors in C-TFB were different from both TFB and the bottom region of high flux CFB. The axial and radius flow structure of C-TFB are

high-density and uniform. This is one of the key advantages of C-TFB over the conventional CFB and TFB. It was also presented that gas-solid contracting in C-TFB is better because of vigorous interaction between the gas and sold phases.

# CHAPTER III

# MATERIALS, EXPERIMENTAL SETUP AND PROCEDURES

In this chapter, materials and equipments used in this dissertation are shown in section 3.1 and section 3.2, respectively. Experiment procedure can be divided into 5 parts: $K_2CO_3/Al_2O_3$ solid sorbent preparation, flow pattern characterization, Method of pressure fluctuation analysis, $CO_2$ adsorption and regeneration capacity and solid sorbent characteristics, as considered in section 3.3.

## 3.1 Materials

### 3.1.1 Chemicals

- Anhydrous potassium carbonate ($K_2CO_3$), M.W. = 138.21 g $mol^{-1}$ from Sigma-Aldrich
- Activated Alumina ($\gamma$-$Al_2O_3$), M.W. = 101.9 g mol-1 from Sigma-Aldrich

### 3.1.2 Gases

- Gases: 12%v $CO_2$ in $N_2$ from Praxair (Thailand) Co., Ltd.
- Ultra high purity (99.999%) $N_2$ from Praxair (Thailand) Co., Ltd.

## 3.2 Equipments and Apparatus set-up

### 3.2.1 Equipments

- Gas flow rate controller : K-1013 and K-1014 series glass rotameters nitto instruments. The accuracy of K-1013 and K-1014 rotameter are ±5. The range of flow rate of K-1013 and K-1014 series are 1-10 and 2-20 l/min, respectively.

- Heater tape : Fiberglass heating tape. The max temperature is 250 °C. The insulating resistance is more than 2 $m\Omega^3$

- Temperature controller : TCL series Digital temperature controller. Input is TC or RTD/PT108 types. The control output is relay or SSR (Solid state relay). Control type is ON/OFF control/PI. The operation conditions are 0-200 °C of temperature and 45-85 Relative humidity%.

- Tube and valve (Brass)

- Glass fluidized bed reactor: The operation condition is 500 °C of temperature.

- Pressure transducer : Fourier DT015. The range of pressure is 150-1150 mbar. The accuracy is ±1 over entire range. The resolution (12-bit) is 0.25 mbar. Default sample rate is 10 samples per second. Response time (for 90% change in reading) is 1 ms. The operating temperature is 0-85 °C.

- Temperature transducer : E52-CA1D temperature Sensor E52. The range of temperature is 0-400 C. Element type is J(IC). Conductor type is Grounded type.

- Data logger : Multilog data logger DB 526. Temperature range is -25-110 °C. The pressure range 0-700 kPa.

- Gas bag : Tedlar gas sampling bags. The maximum volume is 2 l. The maximum temperature is 100 °C.

3.2.2 Apparatus set-up

The experiments were conducted in a lab-scale semi-circulating fluidized bed unit as shown in Figure 3.1. There were 4 main parts such as a gas mixer system, a bubbler, a lab-scale semi-circulating fluidized bed and measuring system of temperature, pressure and carbon dioxide concentration.

The lab-scale semi-circulating fluidized bed included 4 main parts: a riser, a downcomer, a transferline and solid output storage. The riser made from glass had inside diameter of 0.025 m and height of 0.80 m. The downcomer was made of 0.05 cm I.D poly-chloride (PVC) column. The transfer line was made of 0.025 cm I.D poly-chloride column. The ball valve in the transferline was used to control the solid flow feed rate from downcomer to riser. Ten pressure taps were mounted along the height of the riser to measure the pressure signal of the system. The pressure probes were made from stainless steel tube. To prevent the probes to be blocked by fine particles, all pressure and temperature probe tips were covered with filter net of 400 mesh and were inserted inside the wall of the riser. The temperature measurements

were set up 3 points; bottom, middle and top of the riser or 0.075, 0.40 and 0.70 m above the gas distributor.

The gas feed flow rates were measured by a rotameter. The gas entered the riser through the 400 mesh porous plate distributor. The gas bubbler was used to produce water vapor in feed gas before entering the riser. The gas bubbler includes 3 mains parts which were the temperature controlled vessel, dried feed gas input tube and wet feed gas output tube. The dried feed gas input tube penetrated below the level of the water and delivered a feed gas. The other tube extracted a feed gas/vapor mixture from the “headspace” above the liquid. The water vapor content in feed gas was determined by the temperature of liquid in gas bubbler.

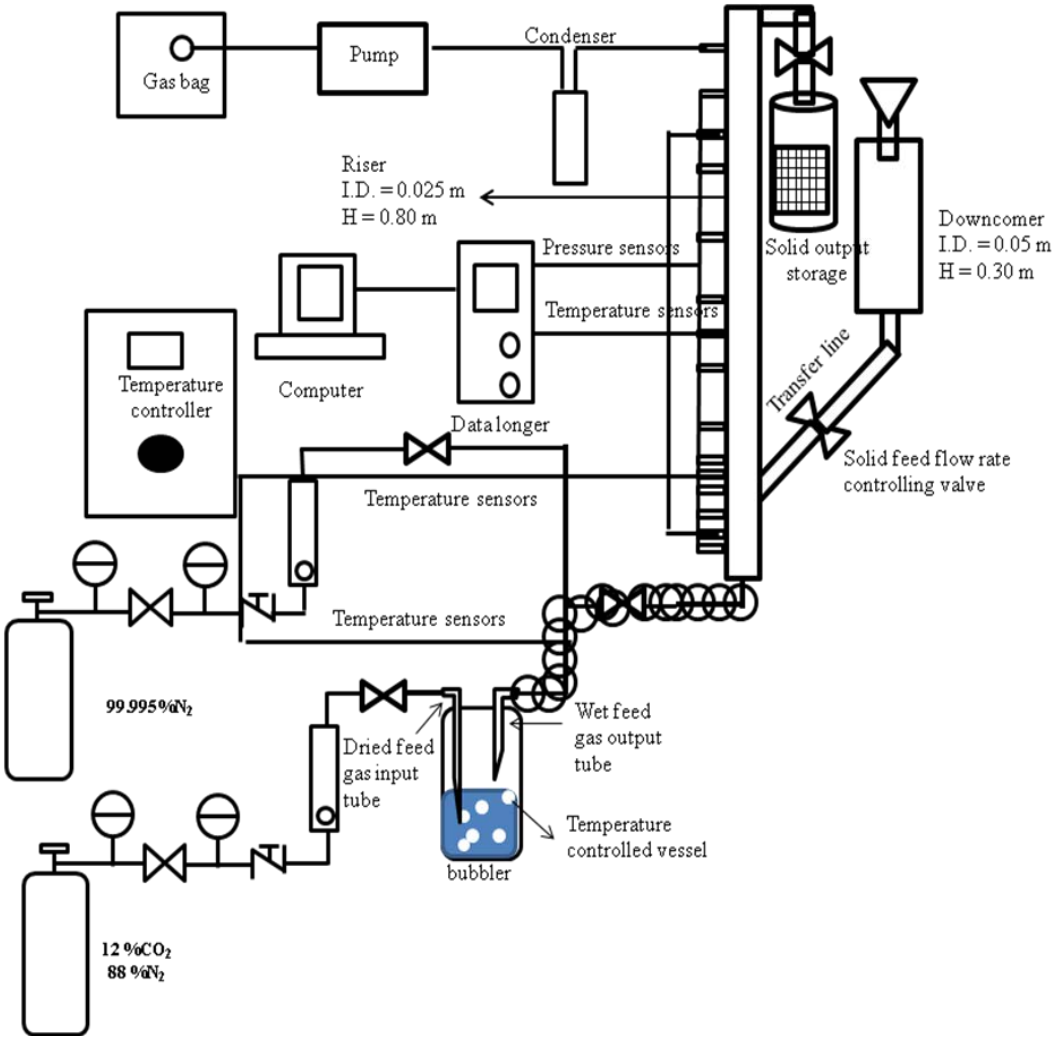


**Figure 3.1 Schematic diagram of the fluidized bed/circulating system used in this research.**

3.2.3 Riser Design

In order to conduct experiments on a small unit, which would be representative of large ones, the dimensionless scaling parameters were used for designing the riser diameter in this study to ensure hydrodynamic similitude in different scale fluidized bed reactors [96]. Four dimensionless group proposed by Glickman et al. (1993) [97] were applied. The complete set can be expressed in dimensionless form as

$$\frac{G_s}{\rho_s U_g}, Fr = \frac{U_g^2}{gD_t}, \frac{U_g}{U_{mf}}, \frac{\rho_g}{\rho_s} \quad (3.1)$$

Where $G_s$ is solid circulation rate, $U_g$ is gas velocity, $\rho_s$ is solid density, Fr is the Froude number, g is gravity, $D_t$ is riser diameter, $U_{mf}$ is minimum fluidization velocity and $\rho_g$ is gas density.

The collected data for large fluidized bed scale used for $CO_2$ capture with $K_2CO_3$ solid sorbent were determined from the following authors analysis: Abanades J.C. et al. (2003) [32], Yi C-H. et al. (2007) [89], Seo Y. et al, (2007) [88], and Park Y.C. et al. (2009) [90]. Four different riser diameters were used as input parameters for small fluidized scale including 0.01, 0.025, 0.04 and 0.05 m. The input parameters of the large fluidized bed are listed in Table 3.1, column 2. Column 3-4 of Table 3.1, shows scale down equivalent of a large fluidized bed of column 2, according to dimensionless scaling parameter as shown in equation (3.1). The gas velocity ($U_g$) of small scale unit was equivalent to the transport velocity, $U_{tr}$ (the onset of fast fluidization regime). The $U_{tr}$ of each case was calculated from the Chehbouni et al. correlation defined as $Re_{tr}=0.169Ar^{0.545}(D_r/d_p)^{0.3}$. Table 3.2 shows the dimensionless parameters for experimental studies listed in Table 3.1.

It can be seen that the $G_s/\rho_p U_g$ and $U_g/U_{mf}$ of four small riser diameter unit were in accordance with the large scale unit, while Fr number and $\rho_g/\rho_p$ of small scale unit differed from large scale. Especially, the Fr number was not having any same value for both large and all small scales. The Fr number of small scale II, corresponding with 0.025 m of riser diameter, was the closest to the large scale unit. Therefore, diameter of 0.025 was chosen to be constructed for studying the $CO_2$ capture in this study.

**Table 3.1 Parameters of a large fluidized bed, with small-scale according to dimensionless scaling parameters. Values in bold are (those values which the dimensional analysis demands are satisfied to ensure similarity) and values in italics are independent input parameter.**

| Parameters | Large Scale | Small Scale I | Small Scale II | Small Scale III | Small Scale IIII |
|---|---|---|---|---|---|
| $U_g$ *(m/s) | 6.00 | 1.72* | 2.26* | 2.61* | 2.79* |
| $G_s$ (kg/m$^2$ s) | 10.20 | **4.39** | **5.77** | **6.65** | **7.11** |
| $d_p$ (m) | 0.0002 | *0.00015* | *0.00015* | *0.00015* | *0.00015* |
| $\rho_p$ (kg/m$^3$) | 2600 | *3900* | *3900* | *3900* | *3900* |
| $D_t$ **(m) | 0.20 | 0.010** | 0.025** | 0.040** | 0.050** |
| $\rho_g$ (kg/m$^3$) | 1.20 | *1.20* | *1.20* | *1.20* | *1.20* |
| $g$ (m/s$^2$) | 9.81 | *9.81* | *9.81* | *9.81* | *9.81* |
| $U_{mf}$ (m/s) | 0.016 | **0.005** | **0.006** | **0.007** | **0.007** |

*The gas velocity ($U_g$) is caluculated by Chehbouni et al. (1995) correlation defined as $Re_{tr}=0.169Ar^{0.545}(D_t/d_p)^{0.3}$.

**The riser diameter is variable parameter.

**Table 3.2 Dimensionless parameters for experimental studies listed in Table 3.1**

| Unit description | $G_s/\rho_p U_g$ | Fr | $U_g/U_{mf}$ | $\rho_g/\rho_p$ |
|---|---|---|---|---|
| **Large Scale** | 0.0007 | 19.35 | 375 | 0.0001 |
| **Small Scale I** | 0.0007 | 30.15 | 375 | 0.0003 |
| **Small Scale II** | 0.0007 | 20.90 | 375 | 0.0003 |
| **Small Scale III** | 0.0007 | 17.32 | 375 | 0.0003 |
| **Small Scale IIII** | 0.0007 | 15.84 | 375 | 0.0003 |

## 3.3 Experiment Procedure

In this study, the experiment procedure can be divided into 5 main parts including $K_2CO_3/Al_2O_3$ solid sorbent preparation, flow pattern characterization, $CO_2$ adsorption, regeneration capacity and solid sorbent characteristics as described in section 3.3.1, 3.3.2, 3.3.3, 3.3.4 and 3.3.5, respectively.

### 3.3.1 $K_2CO_3/Al_2O_3$ Solid Sorbent Preparation

Potassium-based sorbents used in this study were prepared by the conventional impregnation of $K_2CO_3$ on porous supports $\gamma$-$Al_2O_3$. The summarized $K_2CO_3/Al_2O_3$ solid sorbent preparation procedure is shown in the Figure 3.2. Five (5.0) grams of support were added to an aqueous solution containing 5.0 g of anhydrous potassium carbonate ($K_2CO_3$,) in 25 ml of de-ionized water. Then, it was mixed with a solution shaker at room temperature for 24 h [98]. After mixing, the mixture was dried in vacuum oven at 105°C. The dried sample were grained and sieved for collecting the solid sorbent particle size in the range 75-150 μm. Then, the samples were calcined in a furnace for 4 hours at 300 °C. The ramping rate of the temperature was maintained at 3 °C/min. The amount of alkaline metal impregnated was determined by using a Shimadzu AA 6800 atomic absorption spectrophotometer.

The properties of prepared solid sorbent operated in this research is presented in Table 3.3.

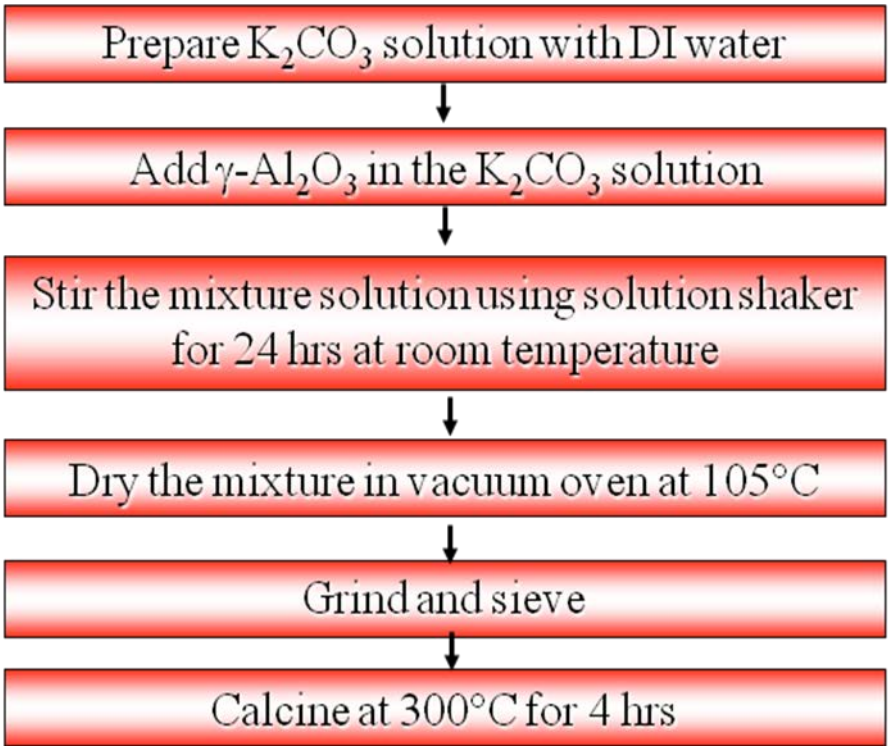


**Figure 3. 2 Workflow chart for preparation of adsorbent by impregnation method.**

**Table 3.3 Prepared $K_2CO_3/Al_2O_3$ solid sorbent properties.**

| Solid properties | Values |
|---|---|
| BET surface area ($m^2/g$) | 80.92 |
| Actual weight of $K_2CO_3$ impregnated on $Al_2O_3$ (% wt.) | 35 |
| Diameter (μm) | 150 |
| Density ($kg/m^3$) | 3900 |

### 3.3.2 Fluidization Flow Pattern Characterization

In this study, gas-solid fluidization system were used to study $CO_2$ capture and regeneration capacity because this system provides high contact level between gas and solid sorbent and high heat and mass transfer rates. Generally, the capacity of reaction between gas and solid strongly depends on performance of the contact

between gas and solid. The performance of the gas-solid contacting in the fluidized bed/circulating fluidized bed strongly depends on the flow pattern/regime operated within fluidized bed/circulating fluidized bed reactor due to different of hydrodynamic behavior in each flow pattern/ regime. There are wide ranges of flow pattern/regimes including multiple-bubbling, slugging, turbulent, and fast fluidizing to homogeneous dilute transport regimes. Therefore, before studying the effect of flow pattern on $CO_2$ capture in fluidized bed/circulating fluidized bed, the flow pattern required to be characterized. In this study, the $K_2CO_3/Al_2O_3$ solid sorbent flow pattern fluidized bed/circulating fluidized bed were investigated by measuring voidage and pressure fluctuation in the system due to easy handling of conducting this measurement, even under difficult operating industrial conditions.

To characterize flow pattern/regime in a fluidized bed/circulating fluidized bed, gas velocity is the main important parameter for this research. For each gas velocity set, two types of pressure measurements were collected: pressure drop to determine the axial solid concentration profile and pressure fluctuations for the gas-solid behavior. The pressure transducers of Fourier DT015 were used to monitor the pressure signals in this study. They were connected to pressure taps and MultiLog data logger (DB-526) which was used to record and store the data. For the pressure drop measurement, the pressure transducers were sampling at the frequency of 10 Hz collecting for 1 minute. In order to detect the strong gradients in solid concentration in the lower part of the riser, pressure taps were densely inserted in this region. For the pressure fluctuation, sampling rate used for pressure drop measurement was found inappropriate. Therefore, the sampling frequency was changed to 100 Hz, collecting for 20 seconds.

Solid volume fraction ($\varepsilon_s$) was calculated by processing the differential pressure or pressure drop, $\Delta P$, measured at successive pressure taps. When acceleration contribution and friction effects at the riser walls were discarded, the relationship $\Delta P=\rho_s(\varepsilon_s)gH$ was used; $\rho_s$, g and H being the solid density, the gravity acceleration and distance between the two pressure taps, respectively [99, 100].

Table 3.4 lists the experimental operating conditions at different gas velocities. Wide ranges of superficial gas velocity from 0.01 to 3.04 m/s were used in this study. Two fluidization systems were operated in this research including non-circulating fluidization and circulating fluidization systems. Non-circulating fluidization was operated at low superficial gas velocity in the range of 0.01-1.02 m/s. For superficial gas velocity higher than 1.02 m/s, the fluidization system was changed from non-circulating fluidization to circulating fluidization system.

**Table 3. 4 Experimental operating conditions used in this research.**

| Range of gas velocity (m/s) | Fluidization system | Solid loading (grams) |
|---|---|---|
| 0.01 -1.02 | Non-circulating | 60 |
| 1.02- 3.04 | Circulating | 300 |

For the non-circulating fluidization system, 60 grams of $K_2CO_3/Al_2O_3$ solid sorbent was fed into the riser as initial bed condition.

For higher superficial gas velocity or circulating fluidization system, 300 grams of $K_2CO_3/Al_2O_3$ solid was operated in the system in order to keep a constant bed: at higher gas flow rates, the solids were carried out over the riser column. Consequently, for circulating fluidization system, at initial condition the bed was composed by 60 grams of $K_2CO_3/Al_2O_3$ solid sorbents (remaining 240 grams being in the downcomer

and transfer line). In this research, the circulating fluidized bed system could not be completely set up. In order to simulate the behavior similar to a conventional circulating fluidized bed systems as close as possible, solid sorbent was recovered at the top of the riser and then fed back manually into the downcomer again. The amounts of solid sorbent accumulated in the downcomer was sufficient to feed them back into the riser without disturbing circulating system even if some solid sorbents were lost at the top of the riser.

### 3.3.3 Method of Pressure Fluctuation Analysis

- **Time-series Analysis.**

All analyses were conducted on time-series data points x(n), with n = 1,2,3…., N, measured at equidistant time intervals, $\Delta t$, with a sampling frequency of $f_s = 1/\Delta t$. N is the total number of samples and x is the pressure signal.

The amplitude of the signal, x, is expressed by the standard deviation (square root of second order statistics, $\sigma$):

$$\sigma = \sqrt{\frac{1}{N-1}\sum_{n-1}^{N}\left(x(n)-\bar{x}\right)^2} \qquad (3.2)$$

With the average,

$$\bar{x} = \frac{1}{N}\sum_{n-1}^{N} x(n) \qquad (3.3)$$

- **Frequency Domain Analysis**

Spectral analysis is commonly used to reveal the periodic signal in a time-series. The power spectral density represents the frequency domain characteristic of a time series and is appropriate for the detection of frequency composition in a

stochastic process [101]. The PSD can be performed using Fast Fourier Transform (FFT). The time signal x(n) estimated as the Fourier transform of the autocorrelation sequence is expressed by [102, 103]:

$$F(f)=\sum_{x=1}^{N} x(n)e^{-j2\pi mf} \tag{3.4}$$

The PSD defined by FFT is calculated from:

$$P_{xx}^{i}(f)=\frac{1}{\sum_{n=1}^{N} w^{2}(n)}\left[\sum_{n-1}^{N} x_{i}(n)w(n)e^{-j2\pi mf}\right]^{2} \tag{3.5}$$

The average PSD frequency becomes:

$$f_{av}=\frac{\sum_{i=1}^{L} P_{xx}^{i} f^{i}}{\sum_{i}^{L} P_{xx}^{i}} \tag{3.6}$$

The averaged PSD intensity becomes:

$$P_{xx}(f)=\frac{1}{L}\sum_{i=1}^{L} P_{xx}^{i}(f) \tag{3.7}$$

### 3.3.4 $CO_2$ Adsorption

Considering $CO_2$ adsorption experiments, there are three main parameters that seem to strongly affect the $CO_2$ capture capacity such as adsorption temperature, water content in feed gas and flow pattern/regime in fluidized bed/circulating fluidized bed. In this $CO_2$ capture study, the $CO_2$ concentration in feed gas remained constant for all experiments as 12 vol.% dry basis. The $K_2CO_3/Al_2O_3$ solid sorbents of 60 and 300 grams respectively for non-circulating and circulating fluidization systems were placed into the riser. In order to simulate real flue gas the water vapor needed for carbonation was fed by passing the mixture gas of $CO_2$ and $N_2$ through a temperature

controlled gas bubbler, and the feed line was heated to avoid water vapor condensation. The gas mixture from the bubbler was assumed to be saturated with $H_2O$, which was confirmed by measuring the relative humidity. The flue gas at the output was kept in gas bags for measuring $CO_2$ concentration by Gas Chromatography.

For the effect of adsorption temperature, 60 grams of $K_2CO_3/Al_2O_3$ solid sorbent was placed into the riser. The solid sorbent was operated at low gas velocity of 0.01 m/s resulting in a fixed bed hydrodynamic behavior practically observed. Four different adsorption temperatures were used to study the $CO_2$ capture capacity such as 60, 70, 80 and 90 °C. Table 3.5 shows experimental conditions of adsorption temperature effect on $CO_2$ adsorption.

**Table 3. 5 Experimental conditions of adsorption temperature effect on $CO_2$ adsorption.**

| **Conditions** | **$CO_2$ adsorption** |
|---|---|
| Adsorption Temperature (°C) | 60, 70, 80 and 90 |
| Pressure (atm) | 1 |
| Flow pattern/regime | Fixed bed |
| Gas velocity (m/s) | 0.01 |
| Flow rate (l/min) | 1 |
| Solid loading (g) | 60 |
| Gas composition (vol.%) | $CO_2$: 12 dry basis with $H_2O$: 18.5, $N_2$ Balance |
| Mole fraction of vapor to $CO_2$ ($x_V/x_C$) | 1.50 |

For the effect of water content in feed gas, 60 grams of $K_2CO_3/Al_2O_3$ solid sorbent was placed into the riser. Solid sorbent was operated at low gas velocity of 0.01 m/s or in fixed bed. Three different water vapor contents were used to study the $CO_2$ capture capacity including 7.4, 13.5, 18.4 and 22.5 vol.%. Table 3.6 shows experimental condition of water vapor content effect on $CO_2$ adsorption.

**Table 3.6 Experimental conditions of water vapor content effect on $CO_2$ adsorption.**

| Conditions | $CO_2$ adsorption |
|---|---|
| Adsorption Temperature (°C) | 60 |
| Pressure (atm) | 1 |
| Flow pattern/regime | Fixed bed |
| Gas velocity (m/s) | 0.01 |
| Flow rate (l/min) | 1 |
| Solid loading | 60 |
| Gas composition (vol.%) | $CO_2$: 12 dry basis with $H_2O$: 7.4, $N_2$ balance<br>$CO_2$: 12 dry basis with $H_2O$: 13.5, $N_2$ balance<br>$CO_2$: 12 dry basis with $H_2O$ 18.4, $N_2$: Balance<br>$CO_2$: 12 dry basis with $H_2O$ 22.5, $N_2$: Balance |
| Mole fraction of vapor to $CO_2$ ($x_V/x_C$) | 0.58 (7.4 % vol. $H_2O$)<br>1.08 (13.5 % vol. $H_2O$)<br>1.50 (18.5 % vol. $H_2O$)<br>1.88 (22.5 % vol. $H_2O$) |

For flow pattern/regime effect on $CO_2$ capture capacity, five different flow patterns/regimes were investigated including fixed bed, multiple-bubbling fluidization, slugging fluidization, turbulent fluidization and fast fluidization. 60 grams of $K_2CO_3/Al_2O_3$ solid sorbent were used for the non-circulating fluidization, including fixed bed, multiple-bubbling fluidization, slugging fluidization and turbulent fluidization. 300 grams of $K_2CO_3/Al_2O_3$ solid sorbent were applied for circulating fluidization, including fast fluidization. The operating method of each regime was explained in fluidization flow patterns/regimes characteristic in section 3.2. The experimental conditions of flow pattern/regime in fluidized bed/circulating fluidized effect on $CO_2$ adsorption was shown in Table 3.7.

**Table 3.7 Experimental conditions of flow pattern/regime in fluidized bed/circulating fluidized bed effect on $CO_2$ adsorption**.

| Conditions | CO2 adsorption |
|---|---|
| Adsorption Temperature (°C) | 60 |
| Pressure (atm) | 1 |
| Flow pattern/regime | Fixed bed, Multiple-bubbling fluidization, Slugging Fluidization Turbulent Fluidization and Fast fluidization. |
| Gas velocity (m/s) | 0.01-2.64 |
| Flow rate (l/min) | 1-30 |
| Solid loading (g) | 60 and 300 |
| Gas composition (vol.%) | $CO_2$: 12 dry basis with $H_2O$: 18.4, $N_2$: Balance |
| Mole fraction of vapor to $CO_2$ ($x_V/x_C$) | 1.50 |

### 3.3.5 Regeneration Capacity

In this section, the effect of regeneration temperature on the $CO_2$ adsorption during multiple-cycle adsorption-regeneration was studied. 60 grams of solid sorbent was placed into the riser and was operated in multiple-bubbling fluidization regime at gas velocity 0.2 m/s. The regeneration was carried out at three different temperatures: 150°C, 250°C and 350 °C for 60 minutes. Since $CO_2$ released during regeneration could not be monitored and there was no simple way to determine when regeneration was complete. After regeneration, the regenerated solid sorbent was used in the multiple bubbling fluidization under 12 vol.% $CO_2$ dry basis with 18.4 vol.% $H_2O$ at 60°C of adsorption temperature for a new adsorption cycle. Table 3.8 shows the experimental conditions for adsorption and regeneration of $K_2CO_3/Al_2O_3$ solid sorbent.

**Table 3.8 Experimental conditions for adsorption and regeneration of $K_2CO_3/Al_2O_3$ solid sorbent.**

| Conditions | $CO_2$ adsorption | Regeneration |
|---|---|---|
| Temperature (°C) | 60 | 150, 250 and 300 |
| Pressure (atm) | 1 | 1 |
| Flow pattern/regime | Multiple-bubbling fluidization | Multiple-bubbling fluidization |
| Gas velocity (m/s) | 0.2 | 0.2 |
| Flow rate (l/min) | 3 | 3 |
| Solid loading (g) | 60 | 60 |
| Gas composition (vol.%) | $CO_2$: 12 dry basis with $H_2O$: 18.4, $N_2$: Balance | $N_2$: 99.999 |
| Mole fraction of vapor to $CO_2$ ($x_V/x_C$) | 1.50 | - |

### 3.3.6 $CO_2$ Evaluation

- $CO_2$ removal fraction (F)

The $CO_2$ adsorption efficiency was evaluated by investigating the $CO_2$ removal fraction. The $CO_2$ removal fraction was expressed as follows:

$$F = \frac{[CO_2]_{input} \bullet Fr_{input} - [CO_2]_{output} \bullet Fr_{output}}{[CO_2]_{input} \bullet F_{r,input}} \quad (5.2)$$

Where $[CO_2]$ is $CO_2$ concentration (%vol.) and $F_r$ is gas flow rate (l/min). Output flow rate ($Fr_{out}$) is calculated from different between input flow rate ($Fr_{input}$) and flow rate of $CO_2$ adsorbed by $K_2CO_3$.

- $CO_2$ capture capacity

In this study, the $CO_2$ capture capacity on the sorbent was determined by integration of the area under the breakthrough curves of weight of $CO_2$ adsorbed by $K_2CO_3$ and time (the data shown in appendix A). This $CO_2$ capture capacity means that the amount of $CO_2$ adsorbed on 1 gram of $K_2CO_3$ when the sorbent was saturated.

### 3.3.7 Solid Sorbent Characterization

- Brunauer-Emmett-Teller (BET) surface is: a method for determining the surface area of a solid material by using $N_2$ adsorption/desorption at -196 °C (Micromeritics ASAP 2020)

- X-ray diffraction (XRD): A Rigaku XRD system equipped with a RINT 2000 wide-angle goniometer employing $CU_{K\alpha}$ radiation ($\lambda$ = 1.54 °A) and X-ray power of 40 kV/30 mA was used to examine the crystalline structure.

- Thermogravimetric analysis (TGA) and Differential Thermal Analysis (DTA) : TGA/DTA were carried out to measure the actual weight of $K_2CO_3$ supported on $Al_2O_3$ using a Mettler TG/SDTA $851^e$ analyser. $N_2$ was used as the carrier gas and the heating rate was 10 °C/min.

- Temperature-programmed desorption (TPD): TPD was used to investigate the desorption temperature of the $K_2CO_3/Al_2O_3$ solid sorbent. The $K_2CO_3/Al_2O_3$ solid sorbents were pretreated in a U-shaped quartz reactor under an Ar flow rate of 40 cm3 min-1 at 60 °C for 1 hour. After this pretreatment, the $K_2CO_3/Al_2O_3$ solid sorbents were cooled to the room temperature. An Ar was then introduced into the reaction at a flow rate of 40 cm3 min-1 and the $K_2CO_3/Al_2O_3$ solid sorbent were heated up to 500 °C at a rate of 10 °C min-1. A thermal conductivity detector (TCD) was employed to determine the amount of $CO_2$ desorbed.

- Atom absorption (AA) : AA is used to investigate the actual weight of $K_2CO_3$ supported on $Al_2O_3$. The $K_2CO_3$ solutions after impregnation were diluted into part per million unit (ppm). The $K_2CO_3$ solution in ppm unit was measured K ion using potassium hollow cathode lamp (Shimadzu AA 6800).

# CHAPTER IV

# FLOW PATTERN/REGIME CHARACTERIZATION RESULTS AND DISCUSSION

In this chapter, various flow patterns/regimes of $K_2CO_3$ based solid sorbent in fluidized/circulating fluidized riser such as bubbling, slugging, turbulent, fast fluidization and homogeneous dilute transport were identified with increasing gas velocity by using several transitions between the hydrodynamic regimes. This result is dicussed in section 4.1. For each flow pattern/regime was then investigated the solid holp up profile along the height of the riser. These results were dicussed in section 4.2. Fluidized bed fluctuations of each flow pattern/regime was also described and dicussed in section 4.3 to study the fluidized quality.

## 4.1 Flow Pattern/Regime in the Fluidized/Circulating Fluidized Riser

A number of regime transitions were used to determine the flow pattern/regimes in fluidized/circulating riser including minimum fluidization velocity ($U_{mf}$), transition velocity ($U_c$), transport velocity ($U_{tr}$) and minimum pneumatic velocity ($V_{mp}$).

### 4.1.1 The Transition from Fixed Bed to Bubbling Fluidization Regimes (Minimum Fluidization Velocity $U_{mf}$)

The minimum fluidization velocity represents the minimum gas velocity required to move particles from fixed-bed to fluidized-bed condition. Solid used in this study is characterized as group B of Geldart particle classification. Therefore, minimum fluidization velocity can be used as the onset velocity for the transition from fixed bed to bubbling fluidization regime.

In this research, the $U_{mf}$ is evaluated by using Puncochar's method which is based on the relationship between standard deviations of pressure fluctuations ($\sigma_p$) measurement and the gas velocity. The pressure fluctuation were measured at height of 0.1 m above the distributor. Figure 4.1 shows the standard deviation of pressure fluctuation at different gas velocity. $U_{mf}$ was defined at the interception of the extrapolated line on the $U_g$ axis ($\sigma_p = 0$). The least squared method was used to calculate the linear relationship between $\sigma_p$ and $U_g$ [103,104]. Its R-square greater than 0.95 were obtained. Therefore, the minimumu fluidized velocity, $U_{mf}$, was found to be 0.02 m/s.

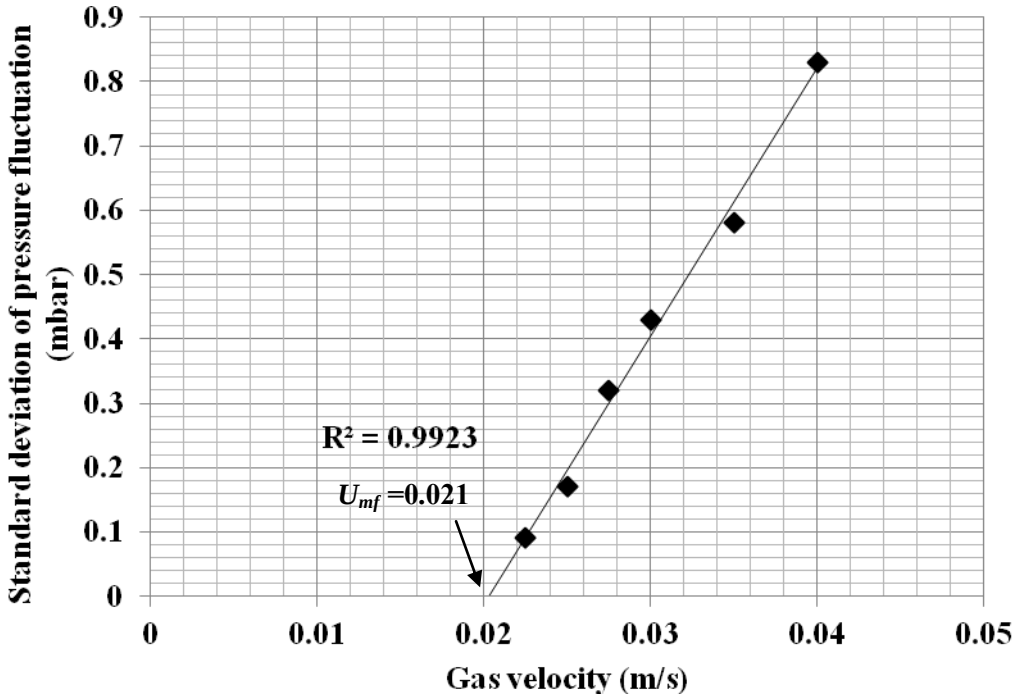


**Figure 4.1 Minimum fluidization velocity by standard deviation of pressure fluctuations-gas velocity curve, position of the pressure measurement: 0.1 m above the gas distributor.**

The accuracy of this method was verified by simple comparison between obtained $U_{mf}$ and the empirical correlation based on the following expressions of Wen and Yu [105], (Equation.(4.1)). Following this equation, the minimum fluidization velocity was calculated to be 0.02 m/s. It can be seen that the the minimum fluidized velocity obtained by observing the standard deviation of pressure fluctuation at the bottom of the riser in this study is consistent with minimum fluidized velocity values calculated from the Wen and Yu correlations.

$$\mathrm{Re}_{mf} = \frac{U_{mf} d_p \rho_g}{\mu} = \left[27.2^2 + 0.0408 Ar\right]^{0.5} - 27.2 \qquad (4.1)$$

### 4.1.2 The Transition from the Bubbling to Turbulent Fluidization Velocity (Transition Velocity Determination, $U_c$)

Turbulent fluidization is generally characterized by low-amplitude fluctuation of voidage and pressure which correspond to the absence of large bubbles or voids. There are two transition criterion proposed to quantify the transition from bubbling/slugging to turbulent fluidization. The first transition criterion is transition velocity, $U_c$, at which the standard deviation of pressure fluctuation reached a maximum. $U_c$ was said to mark the beginning of the transition to turbulent fluidization. The other transition criterion is critical velocity, $U_k$, where the standard deviation of the pressure fluctuation levels off. It was said to denote the end of the transition. Turbulent fluidization is now widely accepted as extending from transition velocity to the onset of fast fluidization [59] and consequently, this study proposed only transition velocity. In the literature, there are several measurement methods available to evaluate transition velocity [61]. In this study, the transition velocity was estimated by observing the standard deviation of pressure fluctuation at the bottom of the riser with different gas velocities using pressure probes located at axial position of 0.15 m as shown in Figure 4.2. As gas velocity was increased in bubbling flow regime, the standard deviation of pressure fluctuation increased rapidly due to coalescence of small bubbles into large bubbles/slugs. The transition velocity is corresponding to the gas velocity at which this standard deviaton reached a maximum. Therefore, the transition velocity in this study was found to be 0.88 m/s. Above transition velocity, the standard deviation decreased gradually as the gas velocity increased due to eruption of large bubbles/slugs into small gas voids which fast coalesed and split alernately.

In addition, the obtained transition velocity was compared with the predicted values based on the available correlations given in Table 4.1. From Table 4.1, it can be seen that the transition velocity obtained by observing the standard deviation of pressure fluctuation at the bottom of the riser in this study is consistent with the range of transition velocity values calculated from the correlations.

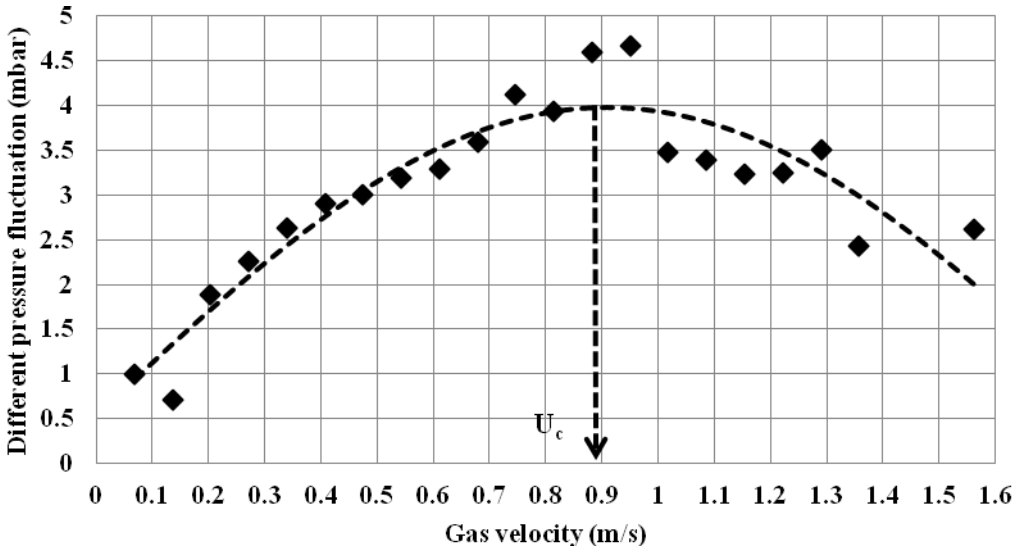


**Figure 4.2 Transition velocity by standard deviation of pressure fluctuation-gas velocity curve, position of the probe: 0.15m.**

**Table 4.1 Comparison between transition velocity from correlations and velocity determined in this research.**

| References | Correlation of $U_c$ | $U_c$ (m/s) | No. |
|---|---|---|---|
| Jin et al. [106] | $U_c / \sqrt{gd_p} = \left( f \frac{D_t}{dp} \frac{\rho_p - \rho_g}{\rho_g} \right)^{0.27}$ <br> $fD_t = 0.00367$ (for bed without internal) | 0.81 | (4.2) |
| Damham et al. [78] | $Re_c = 1.201 Ar^{0.386} (H / D_t)^{0.128 \ln(\rho_p d_p) + 0.264}$ | 0.70 | (4.3) |
| Chehbouni et al. [83] | $U_c / \sqrt{gD_t} = 0.463 Ar^{0.145}$ | 0.65 | (4.4) |
| Lee and Kim [106] | $Re_c = 0.7 Ar^{0.455}$ | 1.00 | (4.5) |
| Nakajima [68] | $Re_c = 0.663 Ar^{0.467}$ | 1.20 | (4.6) |
| This work | - | 0.88 | |

### 4.1.3 Transition from Turbulent to Fast Fluidization (Transport Velocity, $U_{tr}$)

The transport velocity determines the minimum gas velocity required to bring the flow in the riser from the turbulent flow regime to a stable fast fluidization regime [72]. There is more than one technique to measure the transport velocities of solid in the fluidized bed including determination of the flooding point [61], determination of the pressure drop at the bottom of the column as a function of solids circulation rate and superficial gas velocities [74] and determination of the emptying times of a fast-fluidization column [107,108]. Among these methods, the empty-time technique is the most interesting technique because of its simple and quick measurement [81]. Consequently, this technique has been selected to estimate transport velocity in this study. The emptying-time technique is based on measurements of the time required for all solids to leave the bed at different settings of the superficial gas velocity. No

fresh solid was fed to the column and the feed flow control valve at the transfer line was closed. The measurement was not sensitive to the initial solid mass in the column; all experiments were conducted with the sample of 60 grams. From Figure 4.3, at low gas velocities, there was no significant particle entrainment so that the time required to empty the bed was long. As gas velocity is increased, the bed solid could be emptied in a shorter period of time due to sharp increase of particle carryover in the absence of solid recycle. The transport velocity was taken to be the intersection of the lines of low and high accelerations and was found to be 2.20 m/s.

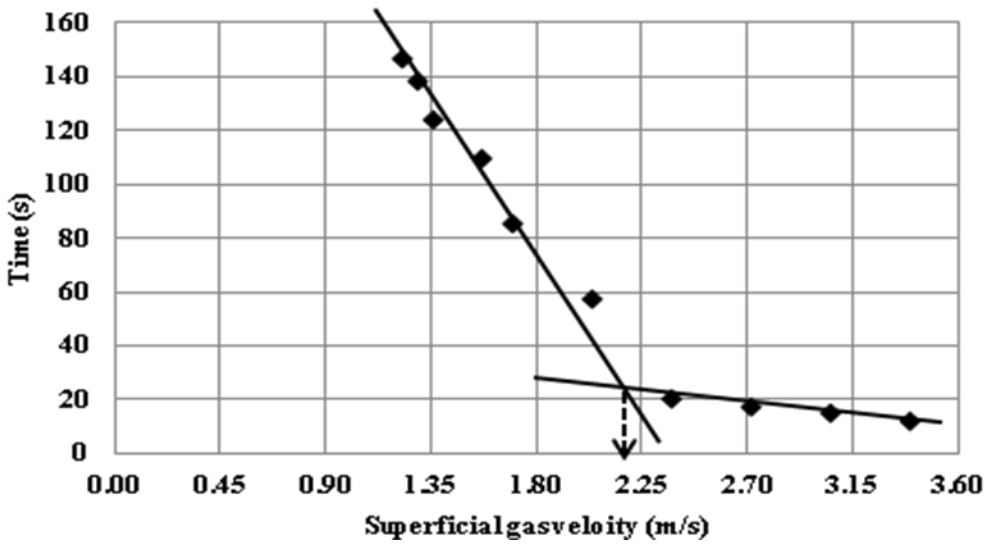


**Figure 4.3 Emptying–time of solid used in this study at various superficial gas velocities for solid loading of 60 grams.**

Several studies have developed correlations for transport velocity as shown in Table 4.2. In addition, the obtained transport velocity was compared with the available correlations given in Table 4.2. It can be observed that the transport velocity

deducted from emptying-time technique was in agreement with correlations as shown in Table 4.2

.

**Table 4.2 Comparison between transport velocity from correlations and velocity determined in this research.**

| References | Correlations of $U_{tr}$ | $U_{tr}$ (m/s) | *No.* |
|---|---|---|---|
| Lee and Kim [109] | $\mathrm{Re}_{tr} = 2.916Ar^{0.356}$ | 2.50 | (5.8) |
| Parales et al. [75] | $\mathrm{Re}_{tr} = 1.41Ar^{0.483}$ | 2.40 | (5.9) |
| Bi and Fan [80] | $\mathrm{Re}_{tr} = 2.28Ar^{0.356}$ | 2.45 | (5.10) |
| Bi et al. [83] | $\mathrm{Re}_{tr} = 1.53Ar^{0.5}$ | 2.50 | (5.11) |
| Chehbouni et al. [83] | $\mathrm{Re}_{tr} = 0.169Ar^{0.545}\left(D/d_p\right)$ | 2.00 | (5.12) |
| This research | - | 2.20 | (5.13) |

In order to define the region of fast fluidization, the transition from fast fluidization to homogeneous dilute transport were studied. It is difficult to detect this transition point experimentally [70]. A Correlation proposed by Bi (1995) [75] is currently available to estimate this velocity. An empirical relation for minimum pneumatic velocity is given by:

$$V_{mp} = 10.1(gd_p)^{0.347}\left(\frac{Gs}{\rho_g}\right)^{0.310}\left(\frac{d_p}{D}\right)^{-0.139} Ar^{-0.021} \qquad (4.7)$$

The minimum pneumatic velocity in this study was 2.64 m/s.

A summary of the regime transition and possible solid flow is provided in Table 4.3. There are 5 different ranges of gas velocity corresponding with various flow patterns. At the gas velocity lower than minimum velocity ($U_{mf}$), fixed bed was

identified. For gas velocity ($U_g$) between minimum fluidization velocity ($U_{mf}$) and transition velocity ($U_c$) or 0.02-0.88 m/s, bubbling fluidization including multiple bubbling and slugging regimes were characterized. When gas velocity was in between transition velocity and transport velocity ($U_{tr}$) or in the range of 0.88-2.20 m/s, the flow pattern changed from bubbling fluidization to turbulent fluidization regime. For gas velocity in the range between transport velocity and minimum pneumatic velocity ($V_{mp}$) (2.20-2.64 m/s), fast fluidization regime was observed. When increasing gas velocity higher than the minimum pneumatic velocity (> 2.64 m/s), flow pattern was described as the homogeneous dilute transport regime. The proposed solid flow patterns for different ranges of superficial gas velocity summarized in Table 4.3 were then used for characterizing the time average solid volume fraction and PSD pattern in the following section.

**Table 4. 3 Possible potassium carbonated impregnated on γ-alumina flow pattern in this research.**

| Velocity range | Ranges of $U_g$ (m/s)in this study | Flow patterns |
|---|---|---|
| $U_{mf} < U_g$ | < 0.02 | Fixed bed |
| $U_{mf}<U_g<U_c$ | 0.02-0.88 | Bubbling fluidization (multiple and slugging bubble) |
| $U_c<U_g<U_{tr}$ | 0.88-2.20 | Turbulent fluidization |
| $U_{tr}<U_g<V_{mp}$ | 2.20-2.64 | Fast Fluidization |
| $V_{mp}<U_g$ | >2.64 | Homogeneous dilute transport |

After the flow pattern/regime characterisation, the pressure fluctuation of each regime was measured during 5 minutes. Figure 4.4 shows the pressure fluctuation in function of time at the bottom of the riser of multiple-bubbling (a), slugging (b),

turbulent (c), circulating turbulent (d) and fast fluidization (e) homogeneous dilute transport regimes (f). It can be seen that the pressure fluctuation were stable during operating in both of fluidization and circulating fluidization systems.

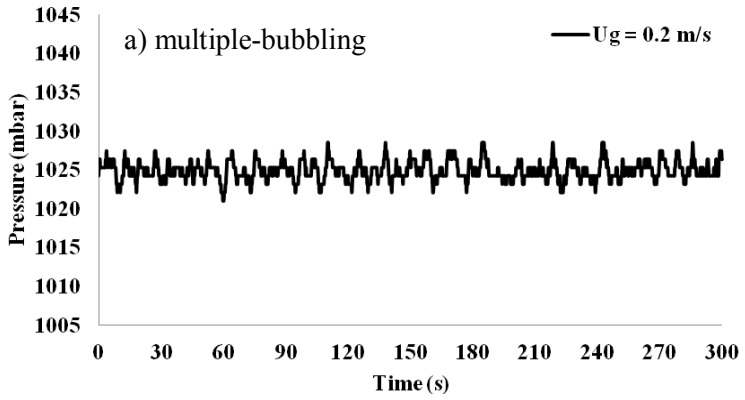


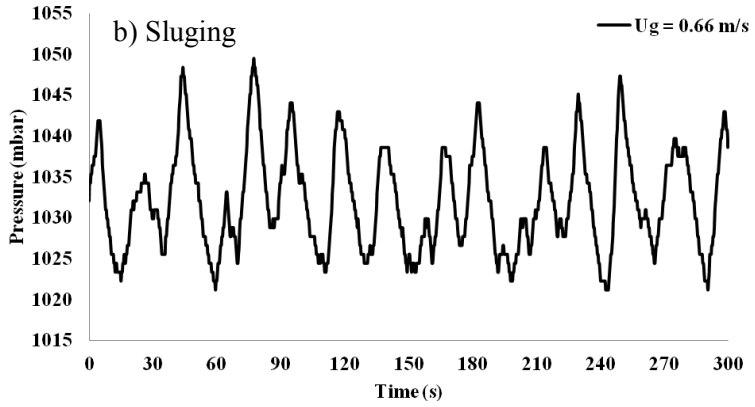


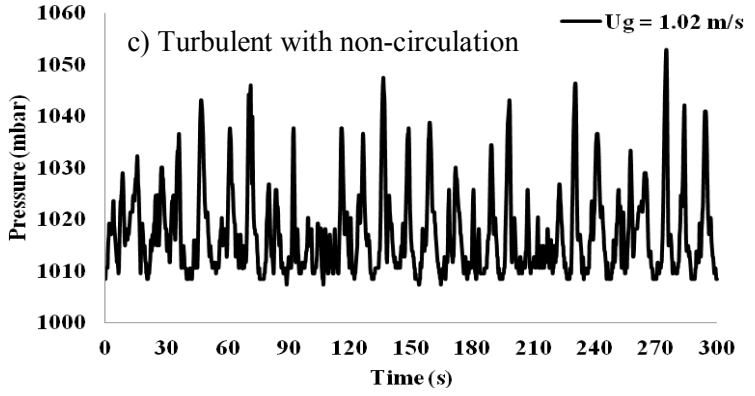

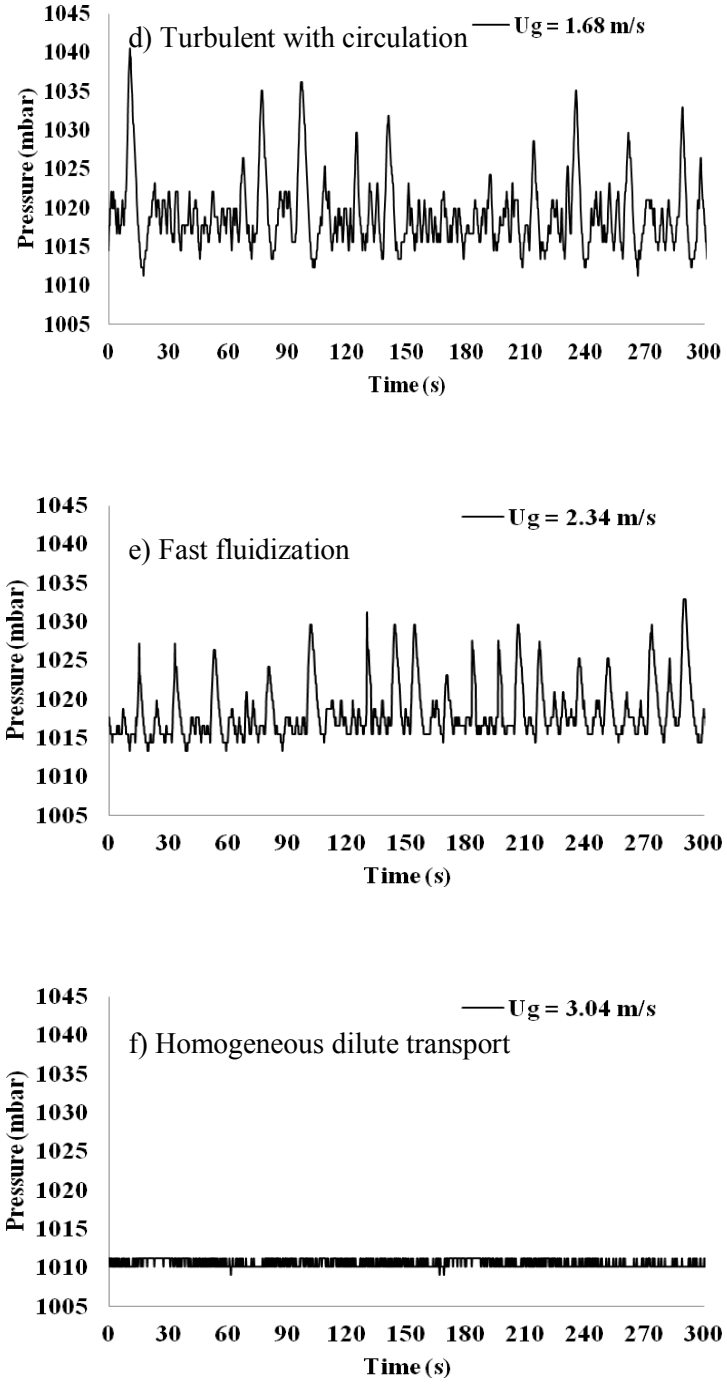


**Figure 4.4 Pressure fluctuations in function of time at the bottom of the riser at five different flow patterns/regimes: a) multiple-bubbling, b) slugging, c) turbulent, d) circulating-turbulent, e) fast fluidization and f) homogeneous dilute transport regime during 300 seconds.**

## 4.2 Time Average Solid Volume Fraction in the Fluidized/Circulating Fluidized Riser

For each operating condition, axial profiles of the pressure in the riser were measured along the height by pressure transducers. Consequently, axial pressures were used to calculate solid volume fraction as explained in the experimental part. The axial solid volume fraction profiles along the riser are shown in Figure 4.5. As expected, the solid volume fraction decreases when superficial gas velocity increases. For the bubbling fluidization regime including multiple-bubbling ($U_g$ = 0.2 m/s) and slugging ($U_g$ = 0.66 m/s), the solid volume fractions were nearly the same for all the heights of the bed and then was suddenly decreasing to zero at position higher that 0.15 cm, because there was no solid left in this region. It can also be seen that when the gas velocity increases, the solid volume fraction decreases due to increasing of drag force. As a result, the solid volume fraction in this regime was in the range of 0.35-0.57.

When increasing the superficial gas velocity higher than transition velocity or superficial gas velocity being in the range of 1.02-1.68 m/s, the flow pattern in the riser became turbulent fluidization regime. From Figure 4.5, it can be seen that the solid volume fraction of turbulent regime at the bottom was lower than that of multiple-bubbling regime because solid in the bed could be easily distributed by gas. Therefore, the solid volume fraction profile along the height with this regime were gradually decreasing before reaching a constant value above 0.35 m of the distributor.

For fast fluidization regime or at superficial gas velocity of 2.34 m/s, the solid volume fraction profile became S-shaped as is typical of a riser operated in the fast

fluidization flow regime with a bottom dense region ($0.15<\varepsilon_s<0.2$), a transition region ($\varepsilon_s$~0.1), and an upper dilute region ($\varepsilon_s$~0.05). This observation was similar to previous conclusions in the literature [95, 100, 111].

At gas velocity being higher than the minimum pnenumatic transport ($U_g$ = 3.04 m/s), the axial solid volume fraction profile expressed better homogeneity because the solid entering into the riser was immediately entrained and no particle accumulation was observed at the bottom of the riser. The solid volume fraction was lower than 0.05 and its pattern, at this gas velocity, was similar to homogeneous dilute transport regime pattern as reported in Smolder et al. [72].

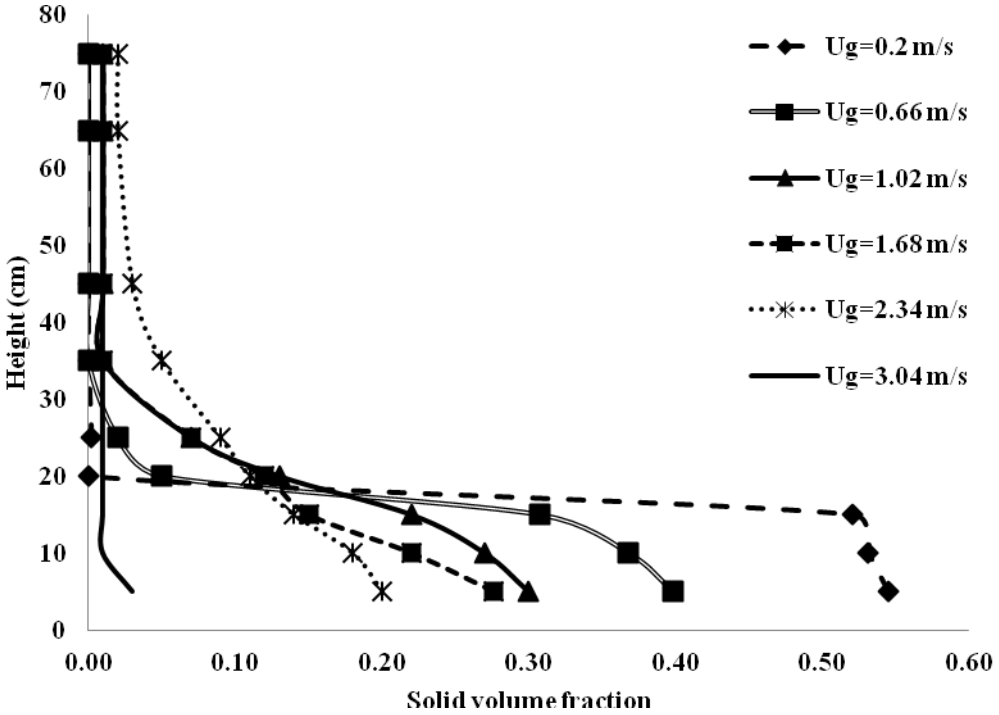


**Figure 4.5 Solid volume fraction profiles along the height of the riser at different superficial gas velocities ($U_g$).**

## 4.3 Power Spectral Density (PSD) Pattern of Different Flow Regimes in the Fluidized/ Circulating Fluidized Riser.

### 4.3.1 Determination of Power Spectral Density (PSD) Characterization of a Multiple-Bubbling Fluidization Regime.

Figure 4.6 shows the PSD patterns obtained by FFT analysis of the pressure fluctuation along the height of the riser in the multiple-bubbling fluidization regime at two different superficial gas velocities of 0.20 m/s (Figure 4.5 (a-c)) and 0.45 m/s (Figure 4.6 (d- f)) with solid loading of 60 grams. The heights of the bed in this regime during the operation were at 0.15 and 0.17 m for gas velocity of 0.2 and 0.45 m/s, respectively. The PSD patterns were observed at three different axial position along the hight of the riser: 0.05, 0.10 and 0.15 m above the gas distributor corresponding to respect ratio or Height/Diameter ratio (H/D ratio): 2, 4 and 6, respectively. From Figure 4.6 (a-c), it can be observed that the multiple-bubbling fluidization regimes, at low gas velocity of 0.2 m/s, had a broad band of peak frequencies between 1 and 4 Hz with a pronounced peak around 1.5 to 3 Hz due to the multitude of bubbles in the bed [112]. For multiple-bubbling regime at higher gas velocity or 0.45 m/s as shown in Figure 4.6 (d-f), the PSD patterns were similar to PSD pattern of gas velocity 0.20 m/s. However, the widths of band were narrower than that of gas velocity 0.20 m/s due to formation of large bubbles. The broad bands of peak frequencies were between 1-3 Hz with the pronounced peak aroud 1.5-2.5 Hz.

Moreover, for all PSD patterns, along the bed height of multiple-bubbling fluidization regime, it can also be observed dominant frequency at about 1.7 Hz. The

dominant frequency is the highest power intensity in the PSD patterns. In agreement with literature reviews, the dominant frequency is found to correspond with different mechanisms or hydrodynamic behavior variation including bubbles formation and eruption. From Figure 4.6 (a-c) and (d-f), the dominant frequencies were observed as a clear distinct peak when the bed height or H/D ratio increased. It can be explained by the fact that bubbles, generated close to the distributor, were growing mostly by coalescence and rising until the bed surface. Therefore, the effect of bubbles formation oscillation on the pressure signal could be noticed clearly at the higher position of the riser. However, the intensities of dominant frequencies of PSD pattern at low gas velocity or 0.2 m/s were around 0.08 $mbar^2$ and lower than that of higher gas velocity or 0.45 m/s with 0.24 $mbar^2$ of dominant frequencies intensities. It means that effect of bubbles formation oscillation on the pressure signal for gas velocity of 0.45 m/s was stronger because the gas bubbles become larger with increasing of gas velocity.

Effect of superficial gas velocity on the PSD patterns of multiple-bubbling fluidization regimes has been investigated as also shown in Figure 4.6. Figure 4.6 (a-c) is the PSD patterns at lower gas velocity or 0.20 m/s and Figure 4.6 (d-f) represents the PSD patterns at higher gas velocity or 0.45 m/s. It can be seen that when superficial gas velocity increased the PSD patterns had narrower peaks. Also, the appearance of dominant peak for higher superficial gas velocity (at 0.45 m/s) was more obvious than that for superficial gas velocity of 0.20 m/s. As an explanation, when the superficial gas velocity is increased, gas bubbles become larger and consequently the effect of gas bubble on the PSD patterns can be observed more clearly for higher superficial gas velocity.

From the PSD patterns results, it can be concluded that PSD pattern of multiple-bubbling regime has board band peak around 1-4 Hz with the dominant frequency of bubble formation of 1.7 Hz. Also, the bubble formation has a strong effect on the pressure signal in fluidization system.

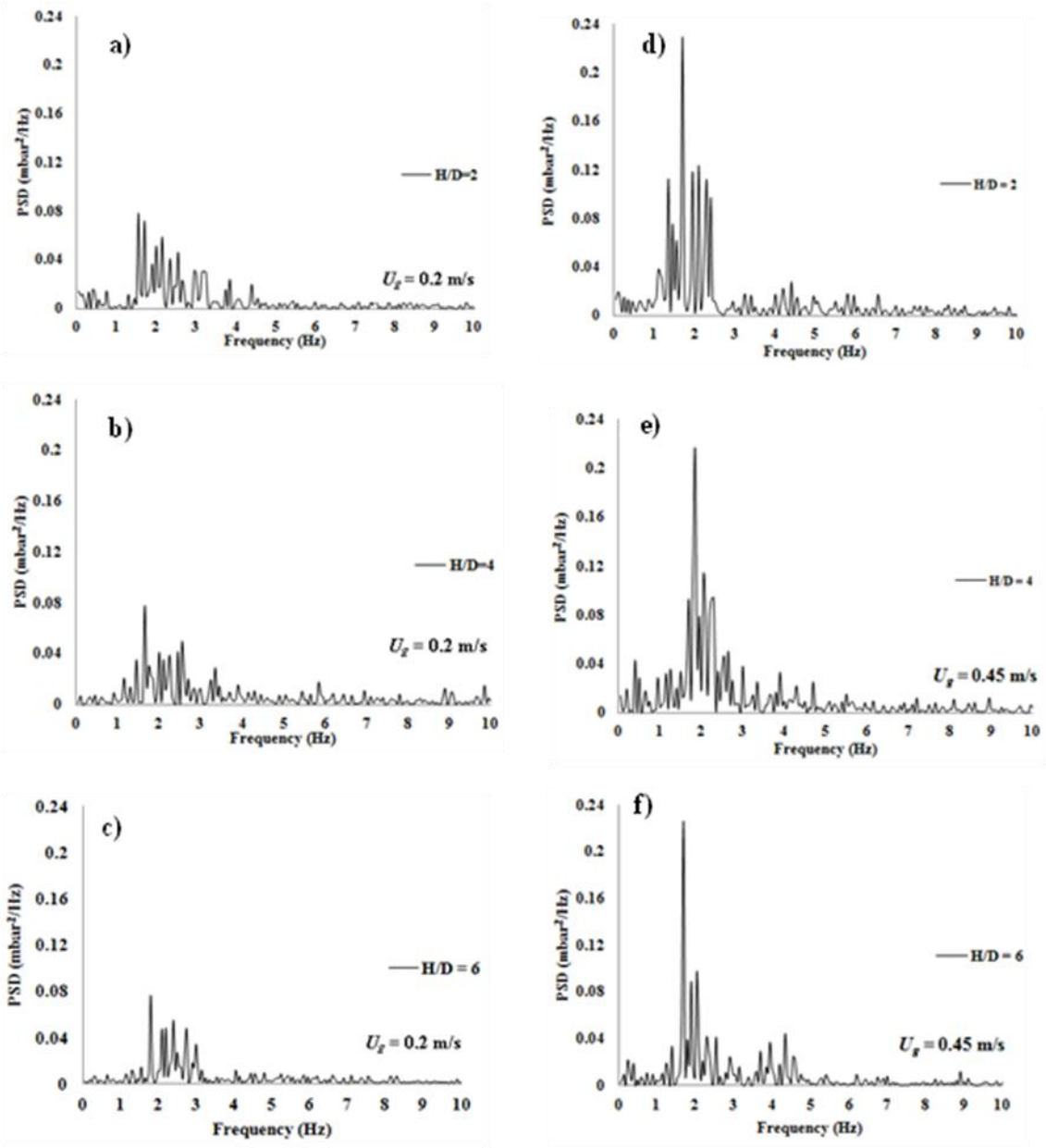


**Figure 4.6 Power spectral density of multiple-bubbling fluidization regime at two different superficial gas velocities 0.2 m/s and 0.45 m/s with various aspect ratios 2, 4 and 6 (a-c) for superficial gas velocity 0.2 m/s and (d-f) for superficial gas velocity ($U_g$).**

### 4.3.2 Determination of Power Spectral Density (PSD) Characterization of a Slugging Fluidization Regime.

Figure 4.7 shows the PSD patterns of a slugging fluidization regime obtained by FFT analysis of the pressure fluctuation along the riser at superficial gas velocity of 0.66 m/s and solid loading of 60 grams. In the slugging regime, bubbles diameter, being close to riser diameter, fills most of the column cross-sectional area. When the bubbles were rising to the top of the surface, they would eventually break [57]. The height of the bed in this regime during the operation was 0.25 m above the gas distributor (H/D ratio 10). Therefore, the PSD patterns at the height of the bed from 0.05 m to 0.25 m or H/D ratio 2 to 10 have been presented only for this regime. From Figure 4.7 (a-d), it can be observed that the PSD patterns had strong narrow peaks with the dominant frequency of 1.7 Hz representing the formation of bubbles. Figure 4.7 (a) shows a wider peak at H/D ratio 2 due to the existence of multiple bubbles. When the H/D ratio was increased to 4, small bubbles agglomerated to be larger bubbles resulting in a significant effect on the pressure fluctuation with narrower bandwidth of the PSD patterns (Figure 4.7 (b)). When the H/D ratio was increased to 6, bubbles were growing even larger and their passage produced large fluctuation inside the bed. Finally, when the H/D ratio was increased to 10, the PSD patterns had not displayed narrow peak as shown in Figure 4.7 (f) which proved that after rising to the top of the surface, the bubbles eventually break. The PSD patterns in slugging fluidization regime can be used to explain and confirm more precisely that the PSD peak at frequency about 1.5-2 Hz with the dominant frequency 1.7 Hz is the

characteristic peak of fluctuation of pressure signal due to the oscillation of bubble formation.

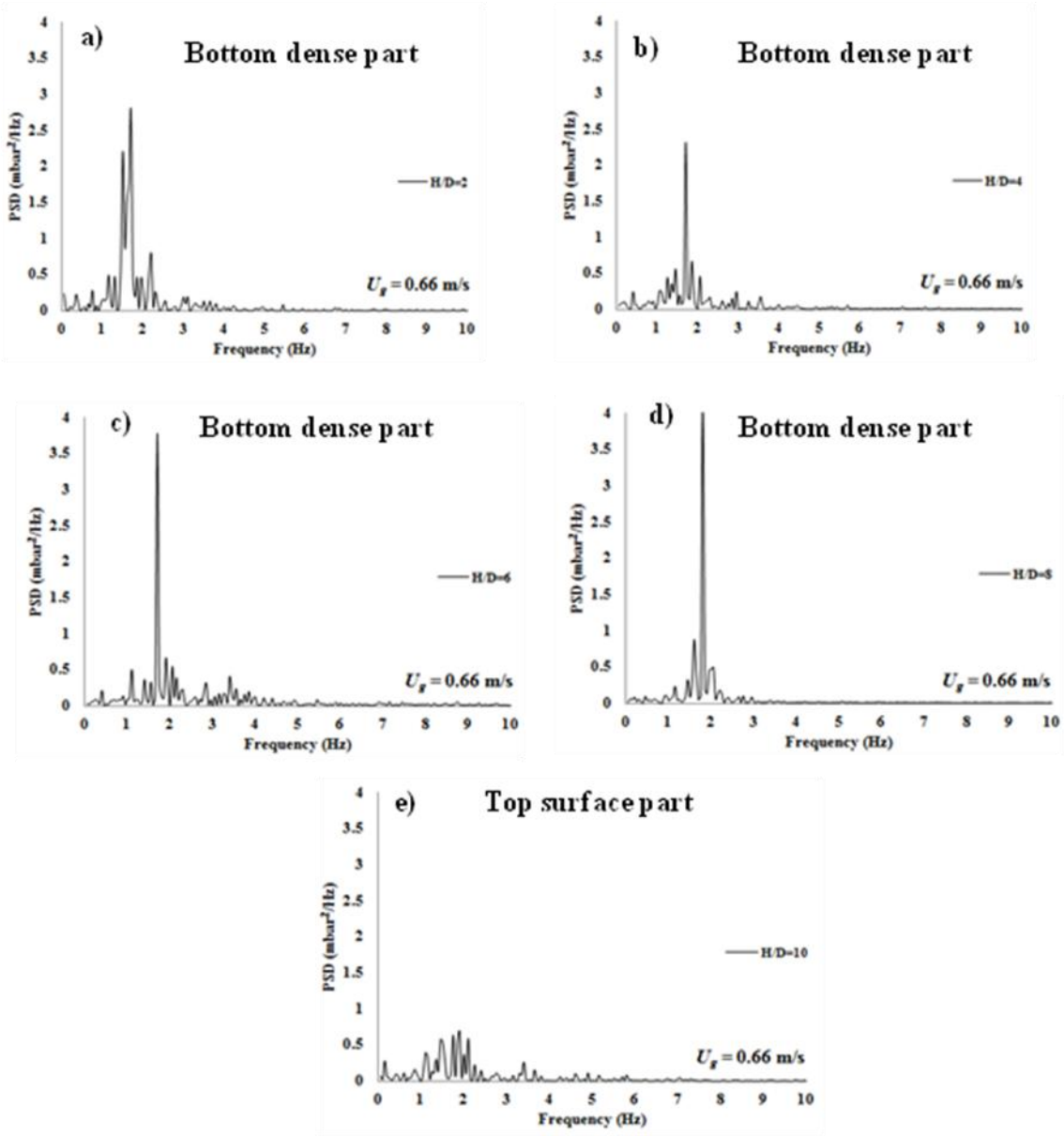


**Figure 4.7 Power spectral density of slugging fluidization regime at superficial gas velocity ($U_g$) 0.66 m/s with different aspect ratios (a) 2 (b) 4 (c) 6 (d) 8 and (e) 10.**

### 4.3.3 Determination of Power Spectral Density (PSD) Characterization of a Turbulent Fluidization Regime.

Figures 4.8 and 4.9 show the PSD patterns obtained by FFT analysis of the pressure fluctuation along the riser in the turbulent fluidization regime with non-circulating (superficial gas velocity 1.02 m/s) and circulating conditions (superficial gas velocity 1.68 m/s), respectively. The turbulent fluidization regime is characterized by the mixing of small bubbles and solid clusters. Solid clusters are going up and down along the height of the riser. This flow pattern is more complex than the bubbling fluidization [50, 113]. For the turbulent fluidization regime with non-circulating, the average bed height while operating was 0.35 m or H/D ratio 14. In the range of H/D ratio from 2 to 10 or dense bottom part, the solid volume fraction was higher than 0.10 and for H/D ratio of 14 or freeboard part, the solid volume fraction was lower than 0.05 (as shown in Figure 4.8). At freeboard part, it can be concluded that only small fine solid particles were distributed by gas.

From Figure 4.8 (a-e) or H/D ratio 2,4,6,8 and 10, the PSD patterns show two distinctive peaks at about 0-0.5 and 1.5-2.0 Hz. They are corresponding with two main hydrodynamics behavior: solid clusters and small bubbles. They have affected on the pressure fluctuation time series signal in the turbulent fluidization regime. From the observation and results of the multiple-bubbling and slugging fluidization regime (as shown in Figures 4.6 and 4.7), it has been concluded that the dominant frequency representing the bubble formation oscillation in this research occurs at 1.7 Hz. Therefore, the PSD narrow peaks with 1.7 Hz dominant frequency in this turbulent flow regime can be explained by the hydrodynamic behavior variation of

time series of pressure fluctuation as a result of bubble formation. The PSD peaks at lower frequency (0-0.5 Hz) represent the variation of pressure signals due to the movement of solid clusters dart close to the wall. At the freeboard or H/D ratio 14 (Figure 4.8 (f)), there were some fine solid particles, resulting from clusters destruction and separation by the gas, projected to the freeboard position. However, the amount of fine solid particles in the freeboard zone was not sufficient to affect the pressure signal and consequently, the pattern at H/D ratio above 14 could not be observed as shown in Figure 4.8 (f).

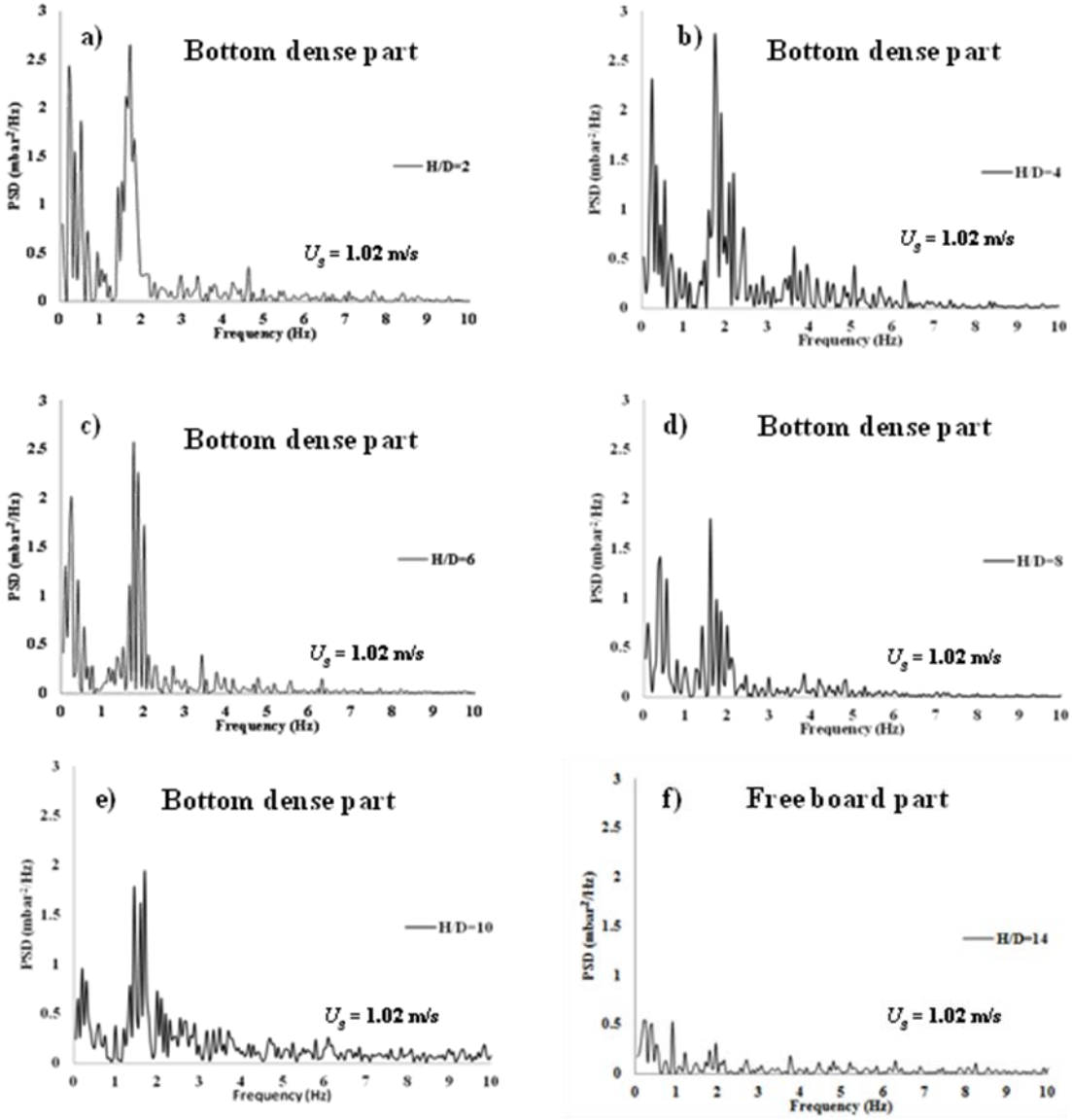


**Figure 4.8 Power spectral density of turbulent fluidization regime with non-circulating operating condition at superficial gas velocity ($U_g$) 1.02 m/s with different aspect ratios (a) 2 (b) 4 (c) 6 (d) 8 (e) 10 and (f) 14.**

Figure 4.9 shows the PSD patterns of the turbulent fluidization regime with circulating conditions along the riser at superficial gas velocity of 1.68 m/s and solid loading of 300 grams. For turbulent fluidization regime with circulating conditions, there were three different sections along the height of the riser including dense bottom section, splash section and free board section. Figure 4.9 (a-d) shows the PSD patterns of dense bottom section. The PSD patterns of splash section and free board are presented in Figure 4.9 (e) and Figure 4.9 (f), respectively.

From Figure 4.9, it can be seen that the PSD patterns were similar to the turbulent fluidization regime patterns with non-circulating operating conditions. At the dense bottom part of the riser (H/D = 2, 4, 6 and 14), there were two significant narrow peaks at about 0-0.5 Hz and 1.5-2 Hz as observed in Figure 4.8 (a-d).

At the splash section (H/D = 18), it can be seen that PSD patterns were different from the PSD patterns of the dense bottom part as shown in Figure 4.9 (e). The PSD patterns of this section had broad band peak with frequency in the range of 0-2 Hz. The dominant frequency peak of bubble formation of 1.7 Hz could not be observed in this section showing that the effect of bubble formation was decreasing in the splash section. For the free board part or at H/D ratio 22, the PSD patterns presented a narrow peak at very low frequency (0-0.25 Hz) and the peak reflecting bubble formation at frequency 1.5-2 Hz was not observed as shown in Figure 4.9 (f) because in this part, there were only some fine solid particles oscillating.

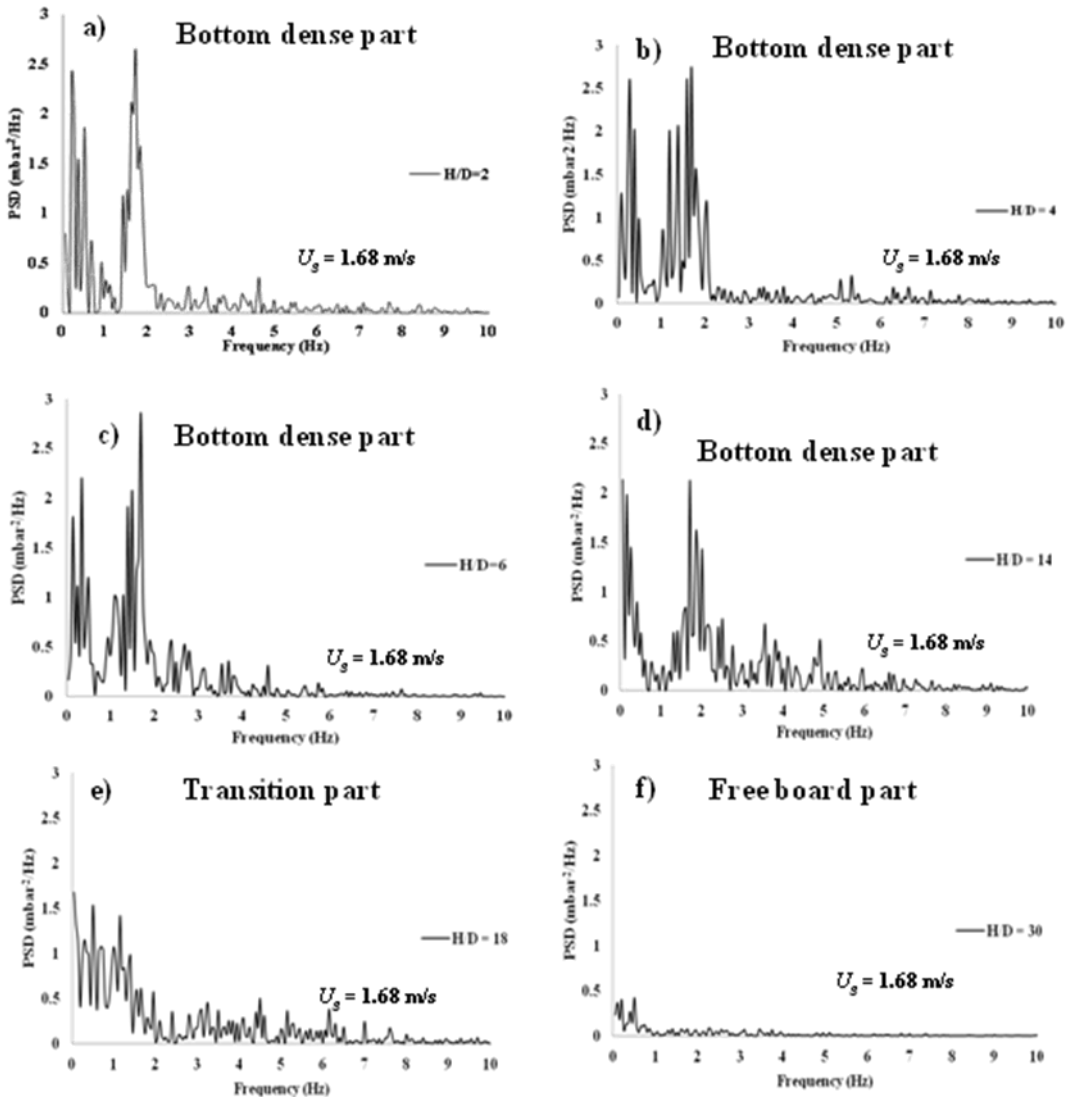


**Figure 4.9 Power spectral density of turbulent fluidization regime with circulating operating condition at superficial gas velocity ($U_g$) 1.68 m/s with different aspect ratios (a) 2 (b) 4 (c) 6 (d) 14 (e) 18 and (f) 30.**

### 4.3.4 Determination of Power Spectral Density (PSD) Characterization of a Fast Fluidization Regime.

Figure 4.10 shows the PSD patterns along the riser in the fast fluidization regime at superficial gas velocity of 2.34 m/s and solid loading of 300 grams. Under this regime, the riser can be divided into 3 parts: the dense bottom part with the mixing of small bubbles and solid clusters, the transition part with the core-annular flow and the dilute part with the uniform solid distribution [67, 95, 100, 111, 112]. The PSD patterns of dense bottom part are shown in Figure 4.10 (a-b) and for transition and dilute parts, PSD patterns are presented in Figure 4.10 (c-d) and Figure 4.10 (e-f), respectively.

In the dense bottom part (Figure 4.10 (a-b)), the PSD patterns for fast fluidization regime had two different narrow peaks as observed for PSD patterns in dense bottom part of turbulent fluidization flow regime. The narrow peak at low frequency in the range of 0-0.5 Hz represents the fluctuation of pressure signal as a result of the oscillation of solid cluster movement mostly close to the wall. The narrow peak at the higher frequency 1-2 Hz with dominant frequency at 1.7 Hz shows the effect of bubbles formation on the pressure fluctuation signal in the fast fluidization regimes. From Figure 4.10 (a-b), it can be concluded that, for dense bottom part, two different hydrodynamic behaviors, including bubble formation and cluster movement, occur.

When the H/D ratio is increased from 4 to10 or in the transition part, the flow structure at the wall of the riser is influenced by clustered solids that move downward while gas and entrained widely-dispersed particles move upward in the interior of the

riser. Following this behavior, the PSD patterns show narrower peak with lower frequency (0.-0.5 Hz) and with the absence of high frequency peak at about 1-2 Hz as shown in Figure 4.10 (c-d). The absence of high frequency peaks proves that the effect of bubble formation disappears on the spontaneous pressure fluctuation time series signal in this transition part. For the narrow peak at low frequency, it is due to fluidized clustered solid oscillations effect [114] as explained in previous section.

In the dilute part (Figure 4.10 (e-f)), it was found that the PSD patterns have narrow peak with frequency range lower than 0.25 Hz. It can be explained by the fact that the pressure signal had low fluctuation due to the presence of only fine solid particles distributed in this part (no clusters and no gas bubbles). It means that the oscillation of fine solid particles have a strong effect on pressure signal in this region [116].

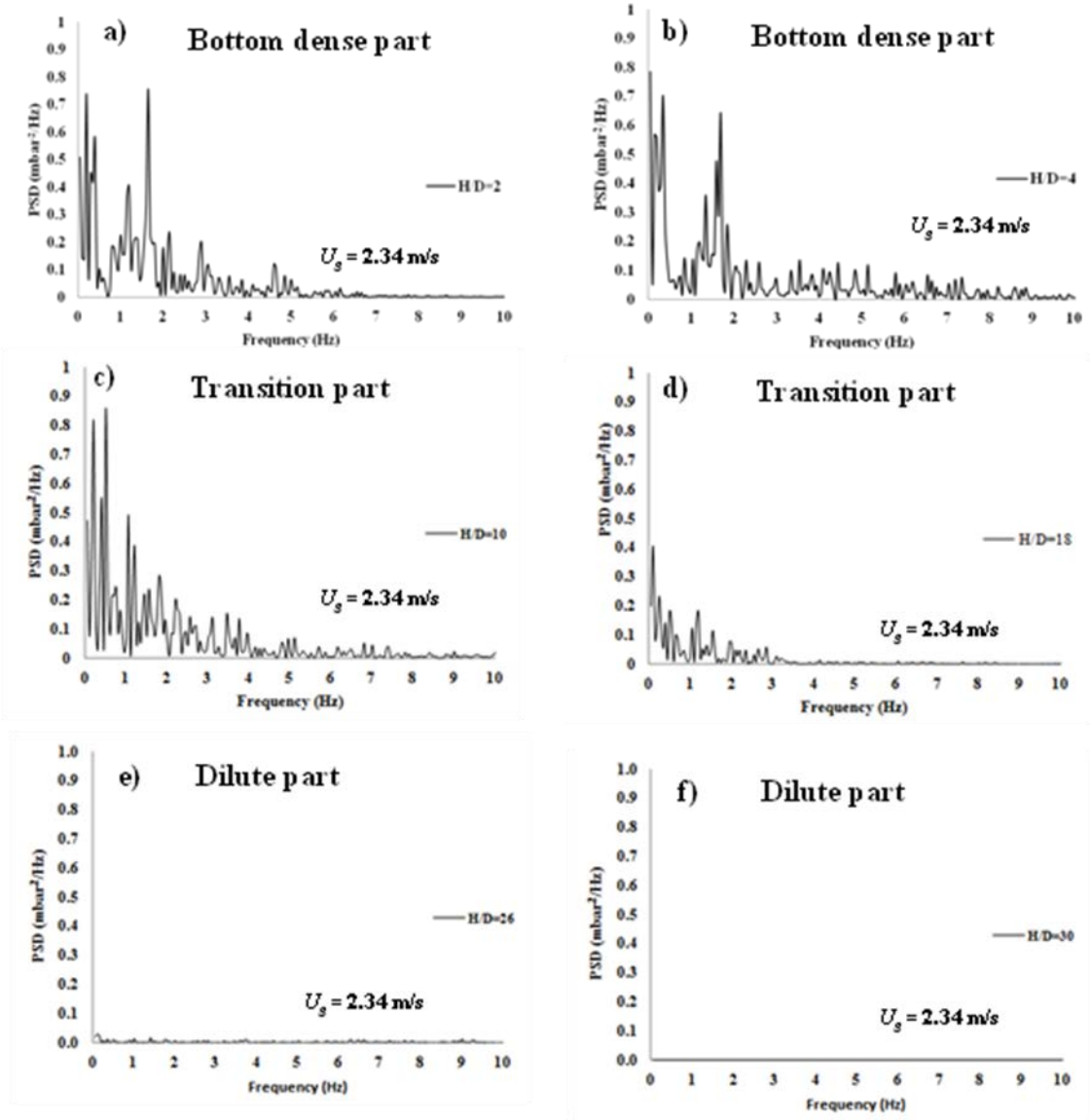


**Figure 4.10 Power spectral density of fast fluidization regime at superficial gas velocity ($U_g$) 2.34 m/s with different aspect ratios (a) 2 (b) 4 (c) 10 (d) 18 (e) 26 and (f) 30.**

### 4.3.5 Determination of Power Spectral Density (PSD) Characterization of a Homogeneous Dilute Transport Regime.

Figure 4.11 shows the PSD patterns of the homogeneous dilute transport regime along the riser at superficial gas velocity of 3.04 m/s and solid loading of 300 grams. It can be seen that, under the homogeneous dilute transport regime, the PSD patterns had a sharp narrow peak at frequency lower than 0.5 Hz and the maximum intensity of PSD remains similar along the height as shown in Figure 4.11 (a-f). In consequence, for velocity above the pneumatic transport velocity, the PSD patterns are corresponding to the oscillations of the fine solid particles.

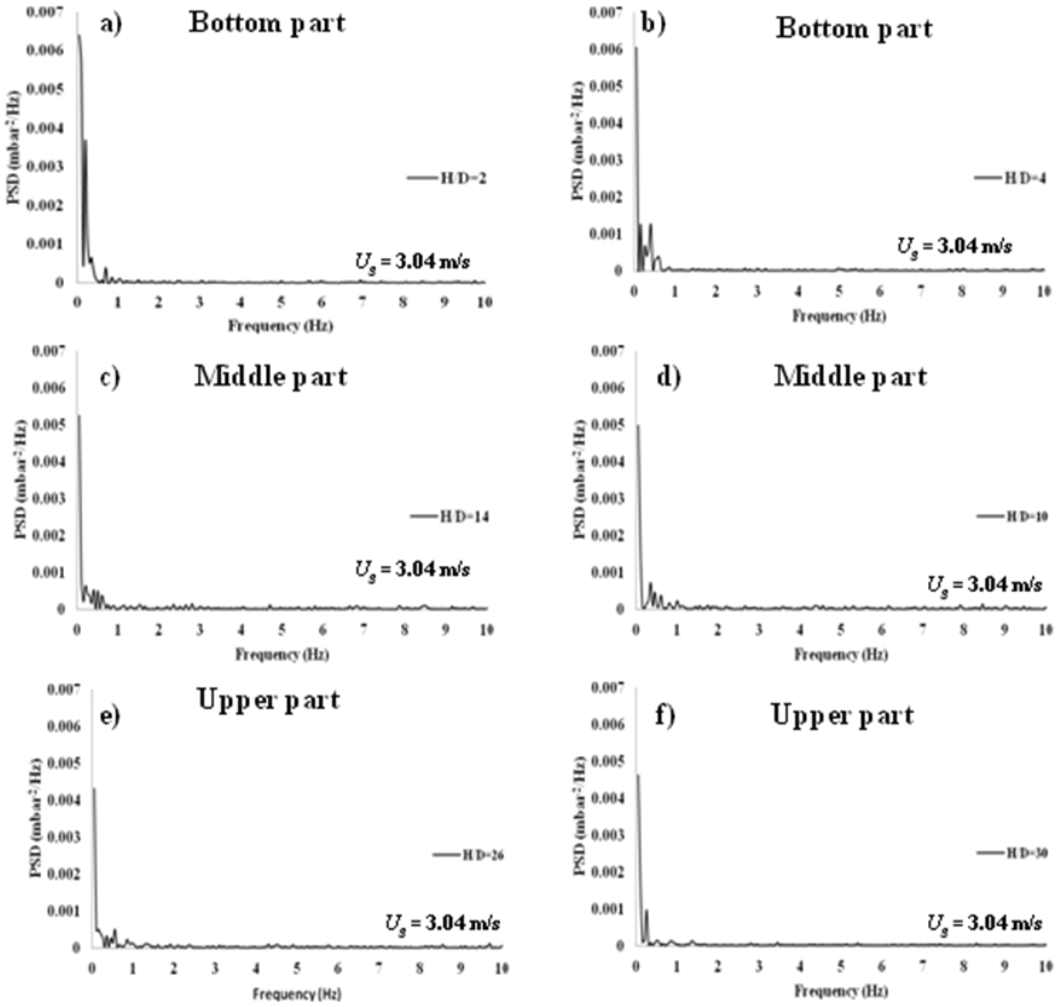


**Figure 4.11 Power spectral density of homogeneous dilute transport regime at superficial gas velocity ($U_g$) 3.04 m/s with different aspect ratios (a) 2 (b) 4 (c) 10 (d) 14 (e) 26 and (f) 30.**

### 4.3.6 Effect of Superficial Gas Velocity on the Power Spectral Density (PSD).

Figure 4.12 shows average PSD frequency ($f_{av}$) against ratio of superficial gas velocity to minimum fluidization velocity ($U_g/U_{mf}$) at different ratios for the bottom part of the riser (H/D = 2, 4 and 6). The average PSD frequency was calculated using Eq. (3.6). From Figure 4.12, it can be seen that the average PSD frequency gradually decreased when increasing $U_g/U_{mf}$ ratio. There are two possible reasons for explaining the reduction of average PSD frequency as a function of gas velocity. As the first explanation, for gas velocity lower than $U_c$ ($U_g/U_{mf} < 44$), the bubbles formation, bubbles eruption and bubbles coalescence are attributed to the pressure fluctuation signal. Van der Schaaf et al. [114] proposed that the large gas bubbles or slug predominantly generated low frequency waves and thus excited low-frequency modes, while small gas bubbles generated high-frequency waves and excited the high-frequency modes. As the second explanation, for gas velocity above $U_c$, the gas void and cluster phenomena are attributed to the pressure fluctuation signal. Clusters oscillation is lower than that of gas void. At high gas velocity ($U_g/U_{mf} > 136$), the pressure fluctuation results from the oscillation of fine solid particles. The oscillation of fine solid particles is lower than that of the clusters. Therefore, the average frequency for $U_g/U_{mf} >136$ could be observed at lower frequency. From these experimental results, it can be also summarized that the frequency corresponding with bubble formation was at the highest frequency. The average frequency representing the effect of fine particles distributed by gas was at the lowest frequency. For the particle clusters movement, the average frequency was observed at the frequency between bubble formation and fine particles flowing.

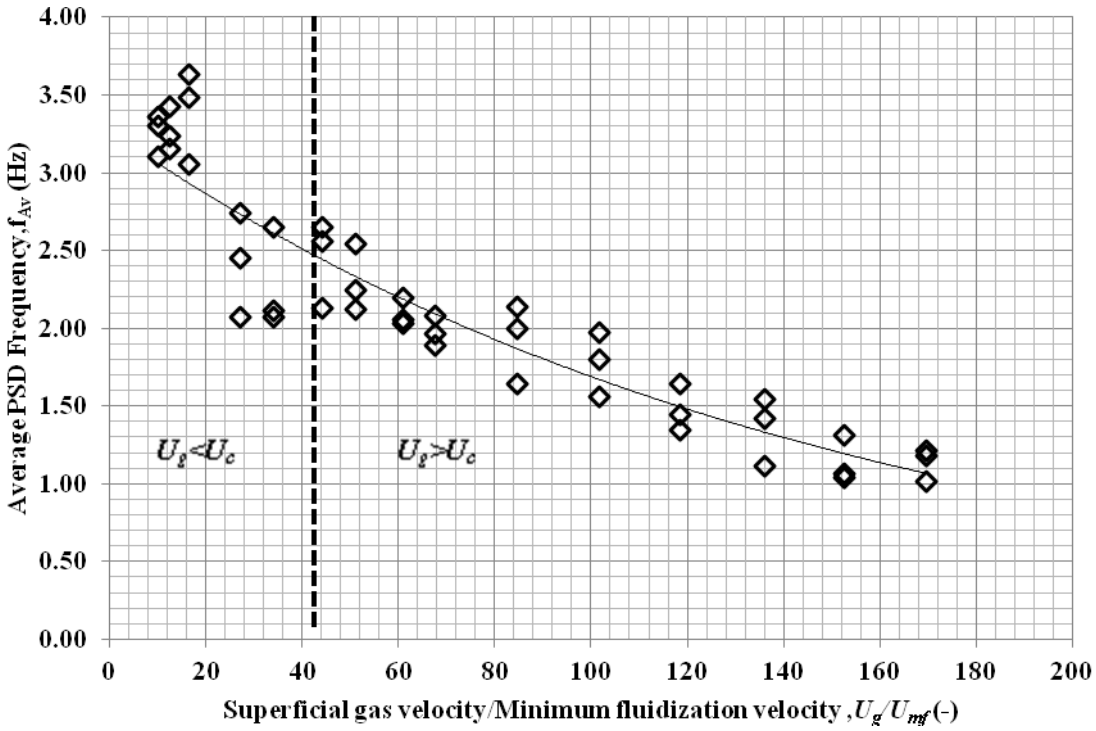


**Figure 4.12 Average power spectral density frequency ($f_{av}$) against ratio of superficial gas velocity to minimum fluidization velocity ($U_g/U_{mf}$) at three different aspect ratios in the bottom of the riser (H/D = 2, 4 and 6).**

Figure 4.13 shows average PSD intensity ($P_{xx}$) against ratio of superficial gas velocity to minimum fluidization velocity ($U_g/U_{mf}$) at different ratios at the bottom part of the riser (H/D = 2, 4 and 6). The average PSD intensity was calculated using Eq. (3.7). The intensity of the power spectral is related to the magnitude of pressure fluctuation. From Figure 4.13, two trends could be observed as a function of $U_g$. When $U_g$ was lower than $U_c$ ($U_g/U_{mf}$ ratio < 44), the intensity of the PSD increased with the superficial gas velocity because of the formation and coalescence of bubbles and slugs. Above $U_c$, the intensity of PSD decreased with increasing superficial gas velocity due to the reduction of bubble effect.

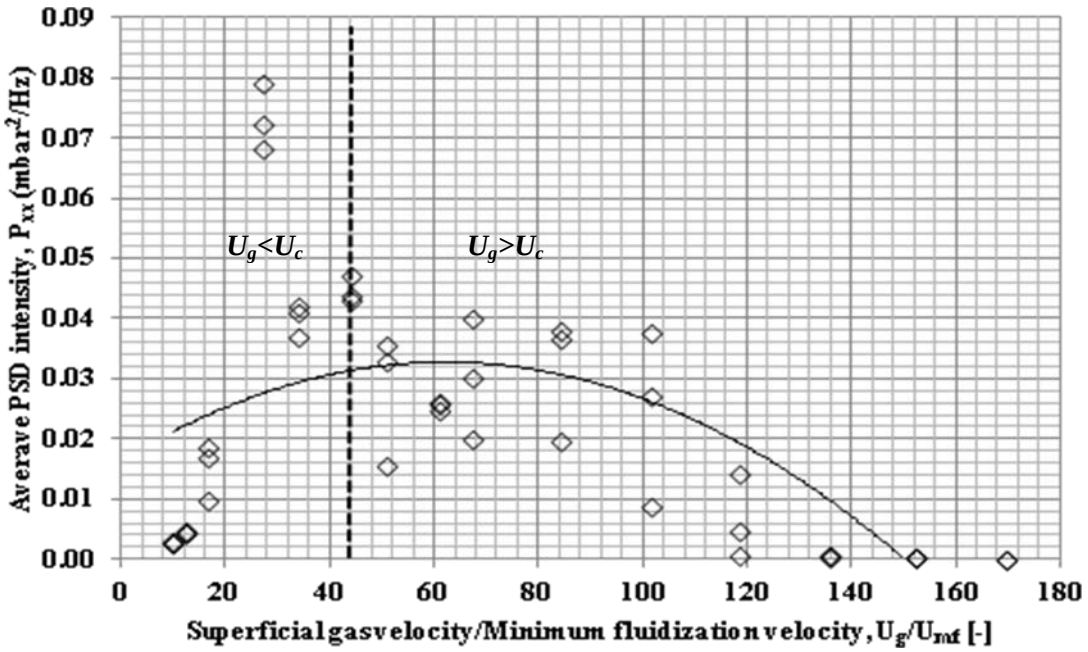


**Figure 4.13 Average power spectral density intensity ($P_{xx}$) against ratio between superficial gas velocity and minimum fluidization velocity ($U_g/U_{mf}$) at three different aspect ratios in the bottom of the riser (H/D = 2, 4 and 6).**

# CHAPTER V

# EFFECT OF FLOW PATTERN ON $CO_2$ ADSORPTION RESULTS AND DISCUSSION

In this chapter, the single-cycle $CO_2$ adsorption using $K_2CO_3/Al_2O_3$ solid sorbent were investigated following 2 main sections. The first part of this study is dealing with $CO_2$ capture testing and the effect of flow patterns on $CO_2$ adsorption. Section 5.1 presents the effect of adsorption temperature, water vapor content on $CO_2$ adsorption and structure of $K_2CO_3/Al_2O_3$ solid sorbent before/after $CO_2$ adsorption by using XRD as discussed in sections 5.1.1, 5.1.2 and 5.1.3, respectively. Finally, the effect of flow patterns/regimes in fluidized bed/circulating fluidized bed on $CO_2$ adsorption is described in section 5.2.

## 5.1 $CO_2$ capture Testing

The reaction involved in the $CO_2$ capture using $K_2CO_3/Al_2O_3$solid sorbent is

$$K_2CO_3(s) + CO_2(g) + H_2O(g) \leftrightarrow 2KHCO_3(s) \quad (5.1)$$

The reaction is reversible and the forward reaction is highly exothermic. Several parameters, such as adsorption temperature and water vapor content in feed gas, have affected on kinetics and thermodynamic of $CO_2$ adsorption reaction using $K_2CO_3/Al_2O_3$ solid sorbent.

### 5.1.1 Effect of Adsorption Temperature on $CO_2$ Adsorption Process

Adsorption temperature affects both kinetics and thermodynamics of the reaction. The effect of adsorption temperature on $CO_2$ capture characteristics using $K_2CO_3/Al_2O_3$ solid sorbent was investigated in a fixed bed reactor. In this study, five different adsorption temperatures were carried out as 50, 60, 70, 80 and 90 ºC at the $CO_2$ concentration of 12 vol.% with dry basis and water concentration of 18.4 vol.%.

Figure 5.1(a) shows the effect of adsorption temperature on the $CO_2$ removal fraction and $CO_2$ capture capacity of potassium-based solid sorbent at 18.4 vol.% water. Two trends of $CO_2$ removal fraction could be observed. For temperature range of 50-60 °C, $CO_2$ capture capacity increased with the increasing temperature while for temperature range of 60-90 ºC, $CO_2$ adsorption decreased with the increasing temperature. Theoretically, low temperature is thermodynamically favorable for higher conversion of $CO_2$ adsorption using solid sorbent because adsorption reaction is highly exothermic. However, adsorption temperature, at 50ºC, shows poor $CO_2$ capture capacity which may be explained by the condensation of water vapor at this temperature. On the other hand, for temperature range of 60-90 °C, the highest $CO_2$ adsorption capacity was observed at 60 °C and its capacity was declined when the temperature was increased to 70°C. The $CO_2$ adsorption capacity was sharply decreased when the temperature was increased to 80°C. The observation implies that $K_2CO_3/Al_2O_3$ solid sorbent may not be effective to capture $CO_2$ above the carbonation temperature of 80°C. Low temperature is of advantage to adsorption reaction. However, the system should be operated above the dew point of the feed gas stream to prevent water condensation. It suggested that the optimal carbonation temperature for

potassium-based sorbent could be about 60ºC, taking into account water vapor condensation at lower temperature and poor $CO_2$ removal at higher temperature.

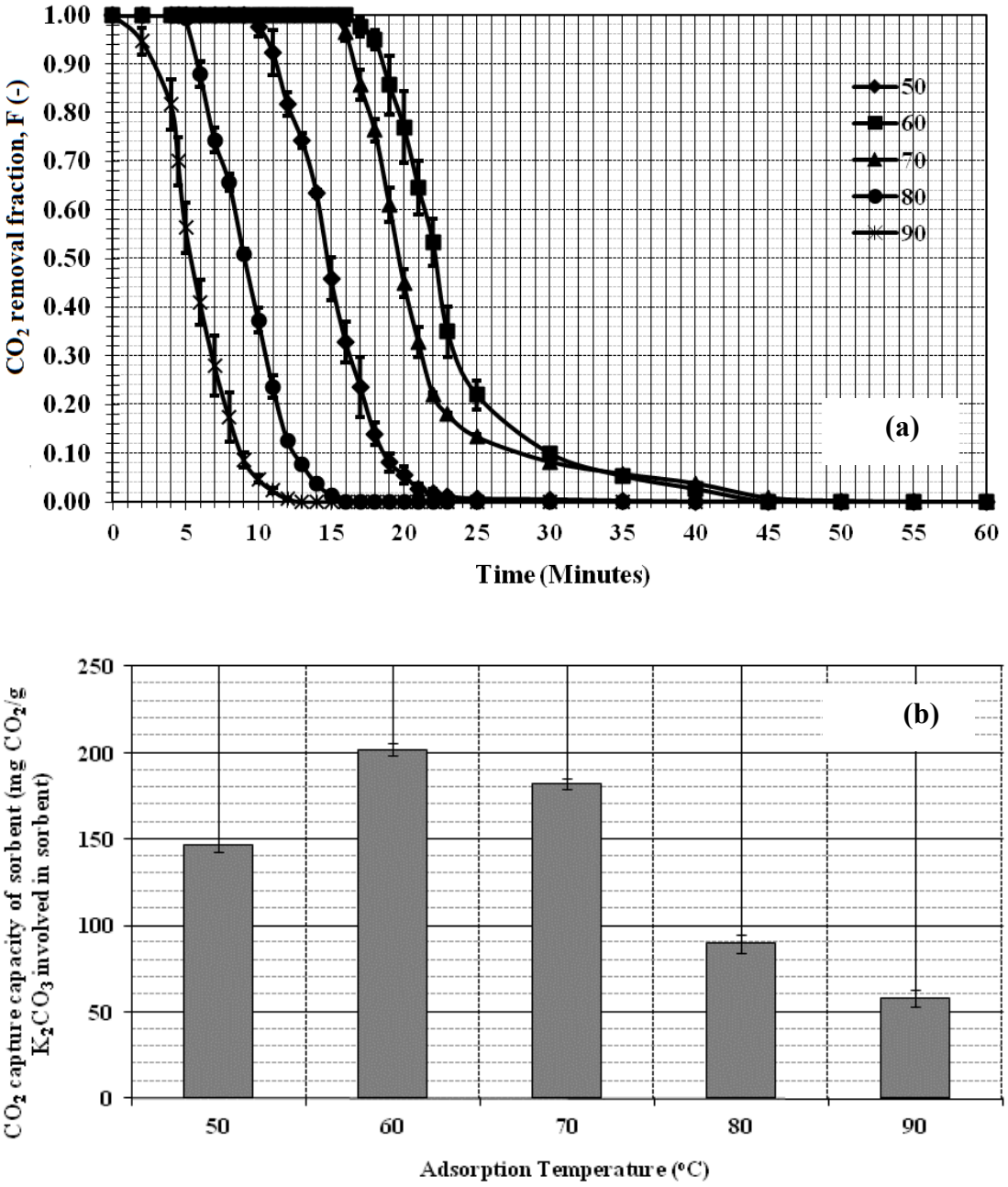


**Figure 5. 1 Effect of adsorption temperature on the $CO_2$ removal fraction (a) and the $CO_2$ capture capacity of $K_2CO_3/Al_2O_3$ solid sorbent (b) in fixed-bed with 12 vol.% $CO_2$ at dry basis and 18.4 vol.% $H_2O$.**

### 5.1.2 Effect of Water Vapor Content in Feed Gas on $CO_2$ Adsorption Process

The effect of water content in feed gas on $CO_2$ capture characteristics using $K_2CO_3/Al_2O_3$ solid sorbent was investigated in a fixed bed reactor. In this study, four different water contents were carried out as 7.0, 13.5, 18.4 and 22.5 vol.%. The mole fractions of vapor content to $CO_2$ concentration are 0.58, 1.08, 1.50 and 1.88, respectively. Figure 5.2(a) shows the $CO_2$ removal fraction at various concentrations of water vapor in the presence of 12 vol.% at dry basis $CO_2$ at 60 °C. Two trends of $CO_2$ removal fraction could be observed. For water content range of 7.0-18.4 vol.%, $CO_2$ adsorption increased with the increasing water content while for water content range of 18.4-22.5 vol.%, $CO_2$ adsorption decreased with the increasing water content. Figure 5.2 (b) shows the $CO_2$ capture capacity as a function of concentration of water vapor in feed gas. In the case of 7.0 vol.% $H_2O$, $CO_2$ capture capacity was about 49 mg $CO_2$/g $K_2CO_3$ involved in sorbent. This value was equivalent to about 15 percent of the theoretical value of the sorbent. Stoichiometically, one mole of $K_2CO_3$ could adsorb one mole of $CO_2$ and one mole of $H_2O$, ($K_2CO_3+H_2O+CO_2 \leftrightarrow 2KHCO_3$). It will produce two moles of potassium hydrogencarbonate ($KHCO_3$). This low capture capacity, under water vapor shortage, could be explained by the above stoichiometric reaction mechanism. As the water vapor concentration increased to 18.4 vol.%, the $CO_2$ capture capacity increased to 195 mg $CO_2$/g $K_2CO_3$ sorbent. However, when the water vapor concentration increased to 22.5 vol.%, the $CO_2$ capture capacity decreased. It can be explained that in this study, the water content in the feed gas was controlled by the temperature of bubbler. However, needed water quantity is injected depending on adsorption reaction temperature. As the adsorption

temperature is increased, water content at saturated condition increases. Therefore, when 22.5 vol.% of water content at 70 °C adsorption temperature, which is higher than adsorption temperature (60 °C), was injected, real water content in feed gas was smaller since condensation occurred. Water drops can decrease solid sorbent activation at the surface of the sorbent [88, 89]

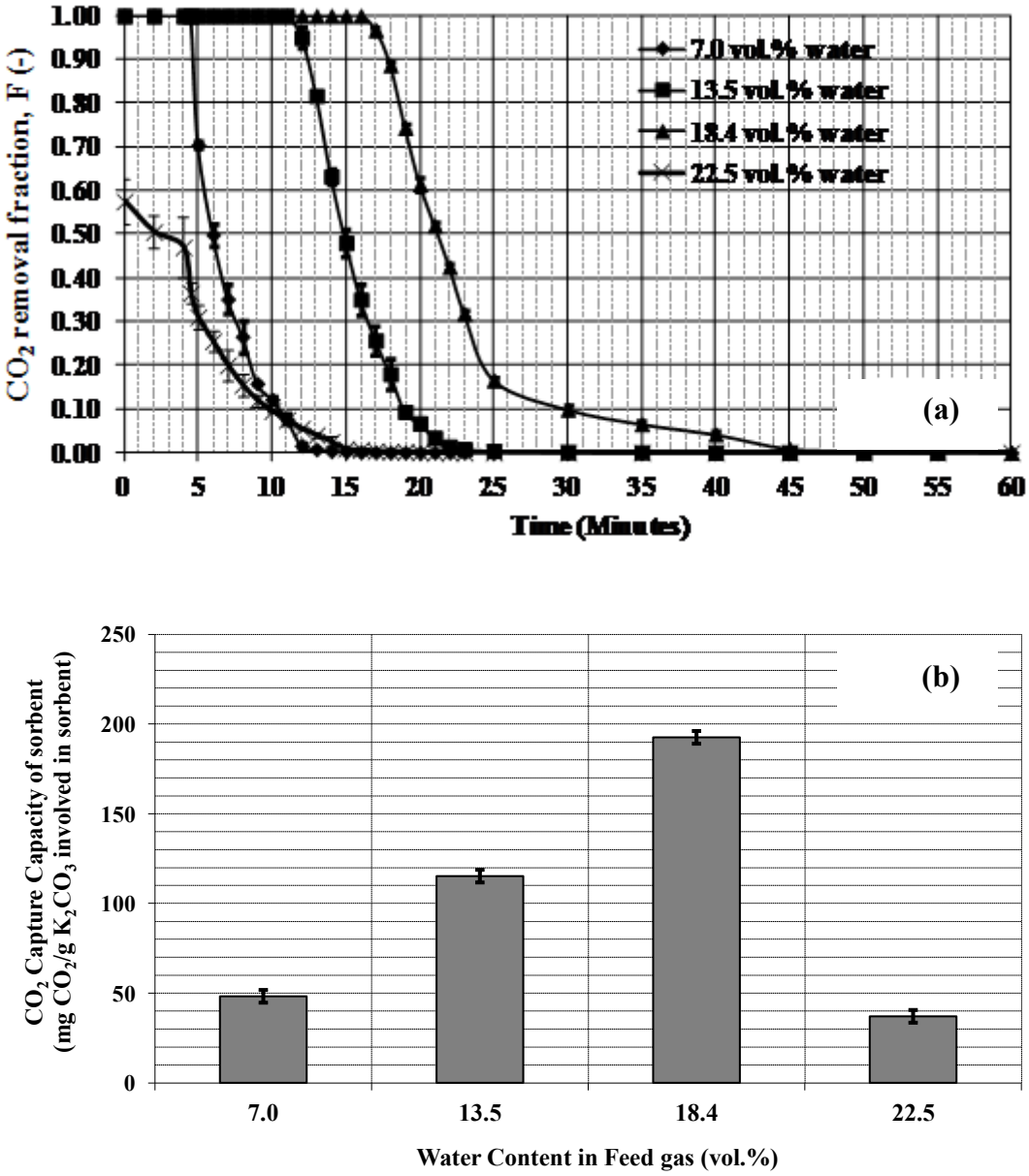


**Figure 5.2 Effect of water vapor content in feed gas on the $CO_2$ removal fraction (a) and the $CO_2$ capture capacity of potassium-based solid sorbent (b) in fixed-bed with 12 vol.% at dry basis CO2 at 60°C.**

### 5.1.3 Structure Identification of the Sorbents Before/after $CO_2$ Adsorption by XRD

In order to investigate the adsorption properties of $K_2CO_3/Al_2O_3$ solid sorbent, the changes of sorbent structure before/after the adsorption were examined by using XRD analysis. Figure 5.3 shows the XRD patterns of $K_2CO_3/Al_2O_3$ solid sorbent before/after adsorption.

It was found that the XRD results of the fresh sorbent before adsorption, which were calcined at 300°C under nitrogen, showed two phases such as $K_2CO_3$ and $KAl(CO_3)_2(OH)_2$ phases. The new diffraction lines appeared with 2θ of 15.9, 21.6, 26.7, 28.4, 31.8, 41.9 and 45.7, which were assigned to the $KAl(CO_3)_2(OH)_2$ phase (JCPDS no. 21-0979) [86, 88]. It was obvious that $KAl(CO_3)_2(OH)_2$ was formed by the reaction of the alumina support with $K_2CO_3$ during calcination at 300 °C.

After the sorbent was used for adsorbing $CO_2$ from simulated flue gas with 12 %vol. of $CO_2$ and 18.4 %vol. of $H_2O$ at 60 °C, the XRD patterns of this sorbent showed two phases including $KHCO_3$ (JCPDS no. 70-0095) and $KAl(CO_3)_2(OH)_2$ [87 and 88]. The increase of the $KAl(CO_3)_2(OH)_2$ peak intensity after $CO_2$ adsorption was observed as shown in Figure 5.3 as a result of higher concentration of this structure.

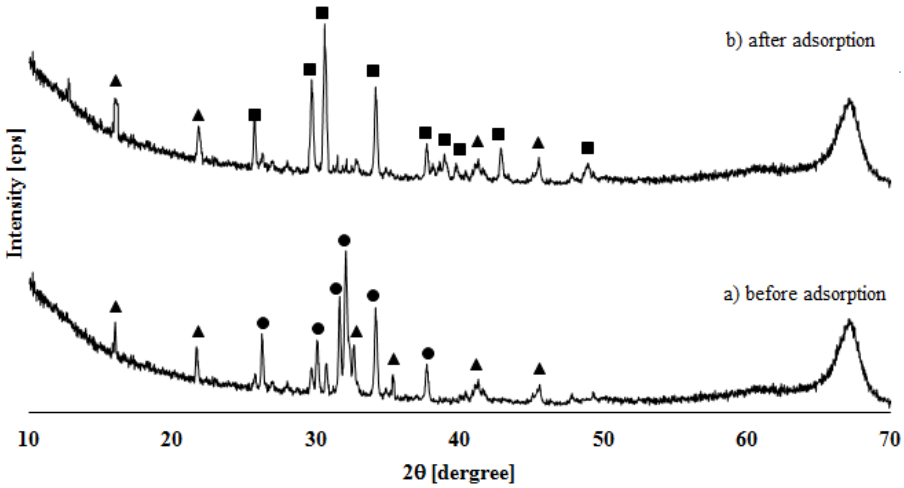


**Figure 5.3 XRD patterns of $K_2CO_3/Al_2O_3$ a) before adsorption (b) after adsorption at 60 °C in 12 vol.% of $CO_2$ at dry basis and 18.4 vol.% of $H_2O$; (●) $K_2CO_3$; (▲) $KAl(CO_3)_2(OH)_2$; (■ ) $KHCO_3$.**

## 5.2 Effect of Flow Patterns/Regimes in Fluidized bed/Circulating Fluidized Bed on $CO_2$ Adsorption

The effect of flow patterns/regimes in fluidized bed/circulating fluidized bed on $CO_2$ removal fraction using prepared $K_2CO_3/Al_2O_3$ solid sorbent is shown in Figure 5.4. Flow pattern regimes investigated in this section includes fixed bed, multiple-bubling, slugging, turbulent and fast fluidization.

It can be seen that, in case of fixed-bed regime, the gas velocity fed to the system was lower than $U_{mf}$. The $K_2CO_3/Al_2O_3$ solid sorbent could adsorb all the $CO_2$ available in the feed gas for 17 minutes. The $CO_2$ breakthroug curve then gradually decreased with increasing adsorbing time. Eventually, the sorbent could not adsorb $CO_2$ longer than 40 minutes.

For multiple-bubbling fluidization regime, the sorbent started to be suspended by gas as a result from the increase of gas velocity. The $CO_2$ removal fraction under multiple-bubbling regime was similar to that under fixed bed regime. However, the

adsorbing time in multiple-bubbling was shorter than that in fixed-bed. The $K_2CO_3/Al_2O_3$ solid sorbents could adsorb all $CO_2$ available in feed gas for 10 minutes and then gradually decreased to 0 at 15 minutes. It can be explained by the fact that the gas velocity used to operate the multiple-bubbling fluidization regime was higher than that of the fixed-bed resulting in higher amount of $CO_2$ passing through sorbent. Therefore, $K_2CO_3/Al_2O_3$ solid sorbent in multiple-bubbling bed have more opportunity to contact with $CO_2$ molecule in feed gas. Yet, the amounts of $K_2CO_3$ sorbent in the bed for both regimes were the same.

When the gas velocity through the bed was increased to 0.66 m/s, the bed change from multiple-bubbling to slugging fluidization regime. It can be seen that the $K_2CO_3/Al_2O_3$ solid sorbent could adsorb all $CO_2$ concentration in feed gas at 0 minute or beginning period when the gas contact with solid sorbent. And then the $CO_2$ removal fraction decreased sharply with the increase of adsorbing time. In the case of slugging regime, the $CO_2$ removal fraction showed different pattern compared to fixed-bed and multiple-bubbling regimes where the S-shape profile of the $CO_2$ removal fraction could not be observed. It can be explained by the fact that in the case of slugging regime, the residence time of gas flowing through the bed is shorter than those for both fixed bed and multiple-bubbling regimes. According to the result, the 0.45 seconds (calculated from the relation between bed hight and gas velocity) of reaction time is not enough for the mass transfer of water into surface of the sorbent.

For turbulent fluidization regime (at gas velocity 1.02 m/s), the $CO_2$ removal fraction of $CO_2$ removal was similar to that of slugging regime. The solid sorbent could not adsorb all $CO_2$ available in feed gas. The maximum removal fraction was 0.95. Then the $CO_2$ removal fraction gradually decreased with the increase of

adsorbing time. The slope of the $CO_2$ removal fraction for turbulent fluidization regime was not as steep as that for slugging regime which was corresponding to lower adsorbing rate. Even though the residence time of gas in turbulent regime was shorter than the slugging regime, the $CO_2$ adsorption on solid sorbents under turbulent regime was better. It means that the turbulent regime has better mixing between gas and $K_2CO_3/Al_2O_3$ solid sorbent. Theoretically, the gas-solid contact in this regime is known to be better compared to previous regimes and the reactor performance approaches the one of the ideal back-mix reactor [53, 62]. However, the solid sorbent could not remove all the $CO_2$ concentration in feed gas which can be explained by the fact that the gas-solid contact time was too short. It can also be highlighted that the $CO_2$ removal fractions observed when sorbent nearly stoped to adsorb after about 5 minutes for turbulent regime were lower than the slugging ones. It shows that the solid sorbent in this regime was very active at the very beginning of the adsorption, and most probably, all active sites were promptly occupied by the $CO_2$ and no $CO_2$ remains to be captured further.

When the solid sorbent was operated in fast fluidization regime, it was elutriated by the fluidizing gas, recovered, and returned to the bottom of the riser at the rate sufficiently high to ensure a minimum level of pressure uniformity in the bed riser. Therefore, the amount of solid sorbents used for this regime were larger than that used for previous regimes. In this regime 300 grams of solid sorbent was used in order to provide sufficient time for determining the $CO_2$ capture capcity. All solid sorbent was fed to the riser via the donwcomer and then $N_2$ pure (> 99.995 vol.%) gases were first supplied to generate the stable state of fast fluidization. Finally, the feed gas was switched to mixture gases of $N_2$ and $CO_2$ to study the $CO_2$ capture. For all fast

fluidization operations, the pressure fluctuation and solid circulation rate were measured for observing the stable state of fast fluidization. The average solid circulation rate is about 30 grams/minute. It tooks 8 minutes for all the 300 grams solid sorbent to get involved and pass through the riser: this is considered to be the first cycle of adsorption completed by all the 300 grams passing initially fed into the system. Continuously, thanks to recirculation, $K_2CO_3/Al_2O_3$ solid sorbents can be operated for adsorption for further cycles. For a fresh initial 300 grams solid sorbent fed into the system, solid sorbent was observed to adsorb $CO_2$ continuously for 4 cycles until adsorption reaction stopped.

From Figure 5.4, it can be seen that during first cycle or 0-8 minutes, the fresh solid sorbent adsorbed 70 percent (F = 0.70) of $CO_2$ available in feed gas. After 8 minutes, the adsorption of solid sorbent gradually decreased. It can be concluded that in the fast fluidization operation, the solid sorbent can remove 70 percent of $CO_2$ in feed gas since the operating gas velocity is very high. Furthermore, it may be explained by the fact that the length of the riser in this study is not very long. If the riser were longer, the $CO_2$ removal may reach 100% percentage.

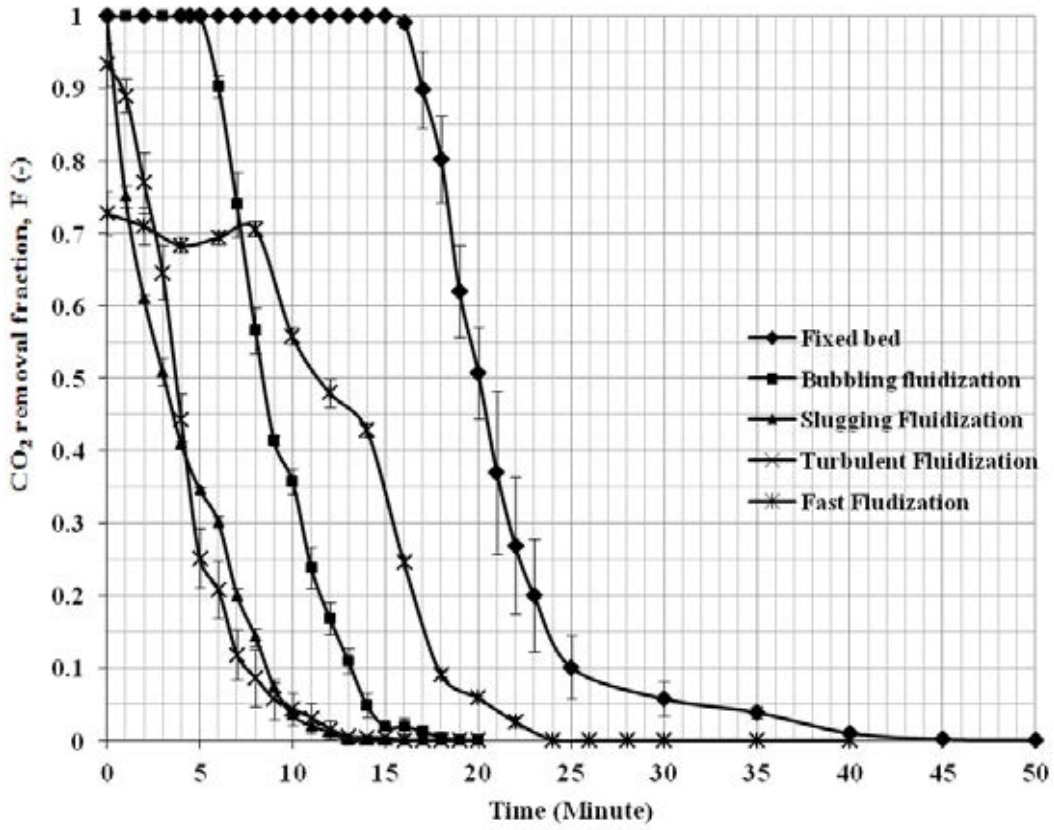


**Figure 5.4 $CO_2$ removal fractional in function of reaction time at different $K_2CO_3/Al_2O_3$ solid sorbent flow patterns/regimes in fluidized bed/circulating fluidized bed at 60 °C of adsorption temperature in 12 vol.% of $CO_2$ at dry basis and 18.4 vol.% of $H_2O$.**

Figure 5.5 shows the effect of flow pattern on the $CO_2$ removal fraction (a) and $CO_2$ capture capacity of $K_2CO_3/Al_2O_3$ solid sorbent (b) for various ratios between $CO_2$ volume in feed gas (G) and $K_2CO_3$ weight involved in bed sorbent (S) (G/S ratio). In the case of fixed-bed, multiple-bubbling fluidization, slugging fluidization and turbulent fluidization patterns/regimes, the amount $K_2CO_3/Al_2O_3$ solid sorbent in the riser was constant at 60 grams. It means that the $K_2CO_3$ involved in solid sorbent was about 21 grams (35 %wt. $K_2CO_3$). The theoretical volume of $CO_2$ to be adsorbed by 21 grams of $K_2CO_3/Al_2O_3$ solid sorbent was estimated to be 4.2 liters. As shown earlier, one mole of $K_2CO_3$ adsorbs one mole of $CO_2$ and one mole of

$H_2O$ ($K_2CO_3+H_2O+CO_2 \leftrightarrow 2KHCO_3$) to form potassium hydrogen carbonate ($KHCO_3$). Thus, the theoretical G/S ratio is 0.2 l/g. Also, for the same amount of $K_2CO_3$ solid sorbent, an increase of G/S ratio means that the $CO_2$ volume in feed gas increased. For fast fluidization pattern/regime, the $K_2CO_3/Al_2O_3$ solid sorbents were entrained from riser by gas. Therefore, the G/S ratio was calculated as a function of the entrained rate of $K_2CO_3/Al_2O_3$ solid sorbent measured during operation. The G/S ratio was defined as a variable parameter for this study in order to observe its effect on the $CO_2$ removal capacity for each different flow regime and in order to eventually conclude precisely on the effect of flow pattern on $CO_2$ removal fraction.

From Figure 5.5 (a), it can be seen that in the case of fixed bed regime, the $K_2CO_3/Al_2O_3$ solid sorbent removed all $CO_2$ (F=1) in feed gas at the G/S ratio lower than 0.10. The $CO_2$ removal fraction was then reduced to 0.3 (30% removal) at G/S ratio of 0.4 l/g. Moreover, 100% $CO_2$ removal can be observed in fixed bed regime which means that the gas residence time in fixed bed regime was sufficient for $CO_2$ adsorption. However, 100% $CO_2$ removal is not observed when the G/S ratio is higher than 0.10 l/g. The $CO_2$ removal fraction for G/S ratio over 0.10 l/g was sharply decreased. Since the theoretical $CO_2$ adsorption capacity of the sorbent was 0.20 l/g, the sharp decline of $CO_2$ removal fraction beyond 0.10 l/g expresses the fact that some of the fresh sorbent does not adsorb $CO_2$ in the feed gas. In order to prove and confirm this explanation, the $CO_2$ capture capacity of $K_2CO_3/Al_2O_3$ solid sorbent was calculated and shown in Figure 5.5 (b). It can be seen that the $CO_2$ capture capacity of $K_2CO_3$ solid sorbent gradually increased as the G/S ratio increased until reaching the equilibrium at G/S ratio of 0.10 l/g. The maximum of $CO_2$ capture capacity of fixed bed regime is about 195 mg $CO_2$/g of $K_2CO_3$. It is only 48% of theoretical value

which is about 320 mg $CO_2$/g of $K_2CO_3$ (the amount of $K_2CO_3$ was 21 grams as established as 35 % wt. of 60 grams of solid sorbent in fixed bed. Therefore, the theoretical weight of $CO_2$ to be stoichiometrically adsorbed by 21 grams of $K_2CO_3/Al_2O_3$ solid sorbent was estimated to be 0.32 grams or 320 milligrams). This result is corresponding to the $CO_2$ removal fraction as shown in Figure 5.5 (a) and highlights the fact that some of fresh solid sorbents do not adsorb $CO_2$ gas. This behavior, in the fixed bed regime, can be reflecting the fact that $K_2CO_3/Al_2O_3$ solid sorbents are not in suspension with the feed gas since the gas velocity is lower than minimum fluidization velocity. As a consequence, most of $K_2CO_3/Al_2O_3$ solid sorbent are immobile, resting on each other and creating small voidage among solid sorbent where the gas can flow through, as described in Figure 5.6 (a). Consequently, some active sites of the sorbent were blocked by other sorbent and not available for $CO_2$ capture.

In the case of multiple-bubbling regime, it can be seen that the $CO_2$ removal fraction profile at various G/S ratios was similar to the fixed bed one as shown in Figure 5.5 (a). The $K_2CO_3/Al_2O_3$ solid sorbent could remove all $CO_2$ in feed gas at the G/S ratio lower than 0.10 l/g. $CO_2$ removal fraction then gradually decreased to 0.4 (or 40 % removal) at G/S ratio of 0.40 l/g. It can also be found that after G/S ratio higher than 0.1 l/g, the $CO_2$ removal fraction of $K_2CO_3/Al_2O_3$ solid sorbent operated in multiple-bubbling fluidized bed was higher than that in the fixed bed regimes at the same G/S ratio. The $CO_2$ removal in multiple-bubbling fluidization regime is more effective than the one observed in fixed bed mostly due to more available contact area between gas and solid. The $CO_2$ capture capacity of the $K_2CO_3/Al_2O_3$ solid sorbents operated in multiple-bubbling fluidized bed at different G/S ratios is shown in Figure

5.5 (b). It can be seen that, as the G/S ratios increased, the $CO_2$ capture capacity of sorbent in the multiple-bubbling fluidized bed gradually increased to maximum capacity of 230 mg $CO_2$/g $K_2CO_3$ at G/S ratio of 0.40 l/g. which was higher than that of fixed bed $CO_2$ capture capacity (195 mg $CO_2$/g $K_2CO_3$). It can be explained that in the multiple-bubbling fluidization patterns/regimes, the reaction occurred by exchanges phenomenon between bubble phase and solid emulsion phase as shown in Figure 5.6(b). Such bubble behavior makes particle circulation in the bed very intensive and efficient around the bubbles and between themselves and even more with particles moving downwards next to the walls. Bubble intense movements as described here consequently promote intensive gas and particle axial mixing in the system.

For slugging fluidization regime, the $K_2CO_3/Al_2O_3$ solid sorbents could not remove all the $CO_2$ in the feed gas, as shown in Figure 5.5 (a). The maximum $CO_2$ removal was 0.85 or 85% removal and it then decreased to 0.3 or 30% removal at G/S ratio of 0.30 l/g. As a comparison with the fixed bed, the $CO_2$ removal fraction, in slugging fluidization regime, was lower for G/S ratio lower than 0.25 l/g because of shorter gas residence time. However, at G/S ratio higher than 0.25 l/g, the $CO_2$ removal fraction in slugging fluidization regime was slightly higher than in fixed bed. It shows that, even if the gas residence time for slugging fluidization is shorter, the mixing between gas and solid in slugging fluidization is better and brings higher efficiency. As a comparison with the multiple-bubbling fluidization, for the same G/S ratio, $CO_2$ removal fraction for slugging fluidization was lower than that observed in multiple-bubbling fluidization. It shows that the multiple-bubbling fluidization provides better gas-solid mixing than slugging fluidization. Indeed, the bubbles

formed in slugging fluidization regime are significantly larger than in multiple-bubbling regime due to the higher gas fluidizing velocity as shown in Figure 5.6 (c). The bubbles may increase to a size comparable to the width of the riser as known as slugging. The slug passes through the riser to the bed surface and therefore, the mixing between slug of gas and $K_2CO_3/Al_2O_3$ solid sorbent is very poor.

The $CO_2$ capture capacity of $K_2CO_3/Al_2O_3$solid sorbent in slugging fluidization regime at various G/S ratios is shown in Figure 5.5 (b), it can be seen that the $CO_2$ capture capacity increased as the G/S ratio increased. The maximum $CO_2$ capture capacity of the $K_2CO_3/Al_2O_3$ solid sorbent in slugging fluidization regime was about 200 mg $CO_2$/g $K_2CO_3$. As comparison with fixed bed regime, the $CO_2$ capture capacity of $K_2CO_3/Al_2O_3$ solid sorbent was lower at low G/S ratio due to shorter residence time in the riser. However, at high G/S ratio, the $CO_2$ capture capacity of solid sorbent was observed to be higher for the slugging fluidization regime. It was also found that the maximum $CO_2$ capture capacity of $K_2CO_3/Al_2O_3$ solid sorbent in slugging regime was higher than in fixed bed. It confirms that, even if slugging regime produces and brings the apparition of big bubbles or slug, the mixing of gas-solid in slugging fluidization regime is better than that in fixed bed one. It can be explained by the fact that the gas velocity used to operate slugging regime was much higher than minimum fluidization velocity resulting in better suspension and mixing of solids. Moreover, the solid sorbents suspended in the bed are more individually separated than those in fixed bed regimes. This is brings less loss in active surface available or is blocked by other solid sorbents. As comparison, for the multiple-bubbling fluidization regime, at the same value of G/S ratio, the $CO_2$ capture capacity of $K_2CO_3/Al_2O_3$ solid sorbent was much better than the one observed for slugging.

Consequently, the mixing between gas-solid in slugging fluidization regime is poorer than that in multiple-bubbling fluidization regime.

In the case of turbulent fluidization regime, $CO_2$ removal fraction at different G/S ratios is presented in Figure 5.5 (a). It can be seen that the $CO_2$ removal fraction was equal to 1 or 100% removal at the G/S ratio lower than 0.10 l/g and then gradually decreased as the G/S ratio increased. As comparison with both fixed bed and multiple-bubbling fluidization regimes, the $CO_2$ removal fraction for turbulent regime was lower at low G/S ratio due to shorter gas residence time. When G/S ratio increased over 0.25 l/g, the $CO_2$ removal fraction in turbulent fluidization regime was higher. It implies that there are active $K_2CO_3/Al_2O_3$ solid sorbents available to capture $CO_2$. It indicates that the turbulent fluidization regime can reduce the loss of active sites from surface hidden or blocked by other $K_2CO_3/Al_2O_3$ solid sorbent. It can be explained by the fact that, in turbulent regime, the large bubble/slug erupted into a number of small bubbles, because of rapid coalescence and bubble breaking alternately. Consequently, this is affecting significantly on bed behavior with the increase of individual separate solid sorbent suspension and higher back-mixing due to higher surface area of fine particles which have been split by bubble/slug eruption as shown in Figure 5.6 (d). Therefore, the turbulent fluidization can have more active surface than those of fixed bed and multiple-bubbling fluidization regimes. As comparison with the slugging fluidization regime, it can be seen that, even if the gas residence time in turbulent bed is shorter than in slugging bed, the $CO_2$ removal fraction in turbulent was higher than in slugging bed regime for all the G/S ratios as shown in Figure 5.5 (a). It shows that the formation of large bubble/slug in slugging

regime reduces considerably the performance of mixing between $K_2CO_3/Al_2O_3$ solid sorbent and $CO_2$ gas during $CO_2$ adsorption.

The $CO_2$ capture capacity of solid sorbent in turbulent fluidization regime at different G/S ratios is shown in Figure 5.5 (b). It can be seen that the $CO_2$ capture capacity of solid sorbent sharply increased with the increasing G/S ratios. The maximum $CO_2$ capture capacity of solid sorbent is about 290 mg $CO_2$/g $K_2CO_3$ involved in sorbent which is about 90 % of the theoretical value. As a comparison with the fixed bed, multiple-bubbling fluidization and slugging fluidization regimes, it can be seen that the $CO_2$ capture capacity of solid sorbent in turbulent regime was significantly higher for all G/S ratios. It implies that gas-solid interaction in turbulent fluidization regime is more efficient than those in fixed bed, multiple-bubbling fluidization and slugging fluidization regimes.

For fast fluidization regime, the $CO_2$ removal fraction at various G/S ratios is shown in Figure 5.5 (a). At 0.28 l/g of G/S ratio, for the circulating fluidized bed, all the 300 gram of fresh $K_2CO_3/Al_2O_3$ solid sorbent are involved and passes through the riser to adsorb $CO_2$ for the first time: a first cycle of adsorption is completed by the 300 grams of solid sorbents. Therefore, for G/S ratio over 0.28 l/g, a second cycle of $K_2CO_3/Al_2O_3$ solid sorbent adsorption can be considered. It was found that for the first circulation cycle, the solid sorbents $CO_2$ fraction removal was about 0.7 (or 70%) during operation. After, for the second cycle adsorption of solid sorbents, the $CO_2$ removal fraction started to decrease as the G/S ratio increased due to recirculation of used solid sorbent. Considering first cycle of fresh solid sorbent, the $CO_2$ removal fraction for fast fluidization regime was lower than for fixed bed and slugging fluidization regimes at G/S ratio lower than 0.10 l/g and 0.20 l/g, respectively. As

comparison with multiple-bubbling and turbulent fluidization regimes, the $CO_2$ removal fraction of fresh solid sorbent in the first cycle under fast fluidization regime was lower. It shows that the faster gas velocity used to get to the fast fluidization regime is resulting in a lower contact time between $K_2CO_3/Al_2O_3$ solid sorbent and gas.

$CO_2$ capture capacity of $K_2CO_3/Al_2O_3$ solid sorbent at various G/S ratios in fast fluidization regime is shown in Figure 5.5 (b). It can be seen that the $CO_2$ capture capacity of solid sorbent gradually increased as the G/S ratio increased. The maximum $CO_2$ capture capacity of fresh $K_2CO_3/Al_2O_3$ solid sorbent in fast fluidization regime is 210 mg/g $K_2CO_3$. As a comparison with fixed bed and slugging fluidization regimes, the maximum $CO_2$ capture capacity in fast fluidization is higher than those in both these regimes. It also shows that the mixing behavior between solid sorbent and gas in fast fluidization is better than those in both fixed bed and slugging fluidization regimes, due to higher dispersion of solid and gas along the riser. Moreover, the fast fluidization have more effective surface area of solid sorbent, because each solid sorbent is travelling independently from each other as shown in Figure 5.6 (e). On the other hand, the $CO_2$ capture capacity of $K_2CO_3/Al_2O_3$ solid sorbent in fast fluidization was lower than those in multiple-bubbling and turbulent fluidization regimes due to the gas residence time in fast fluidization being too short.

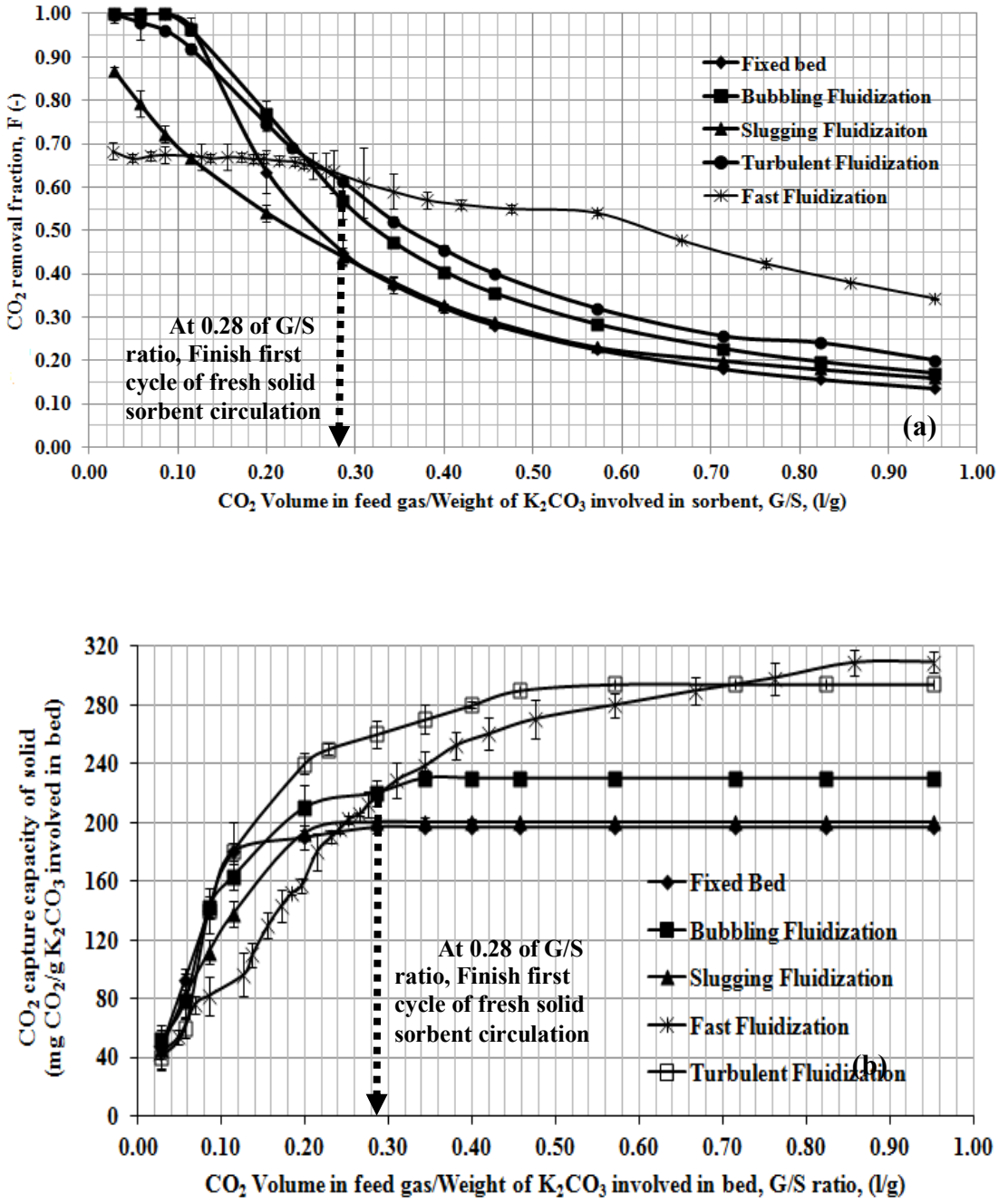


**Figure 5.5 Effect of flow pattern on the $CO_2$ removal fraction and $CO_2$ capture capacity of $K_2CO_3/Al_2O_3$ solid sorbent (b) at various the ratios between $CO_2$ volume in feed gas (G) and $K_2CO_3$ weight involving in bed sorbent (S) (G/S ratio).**

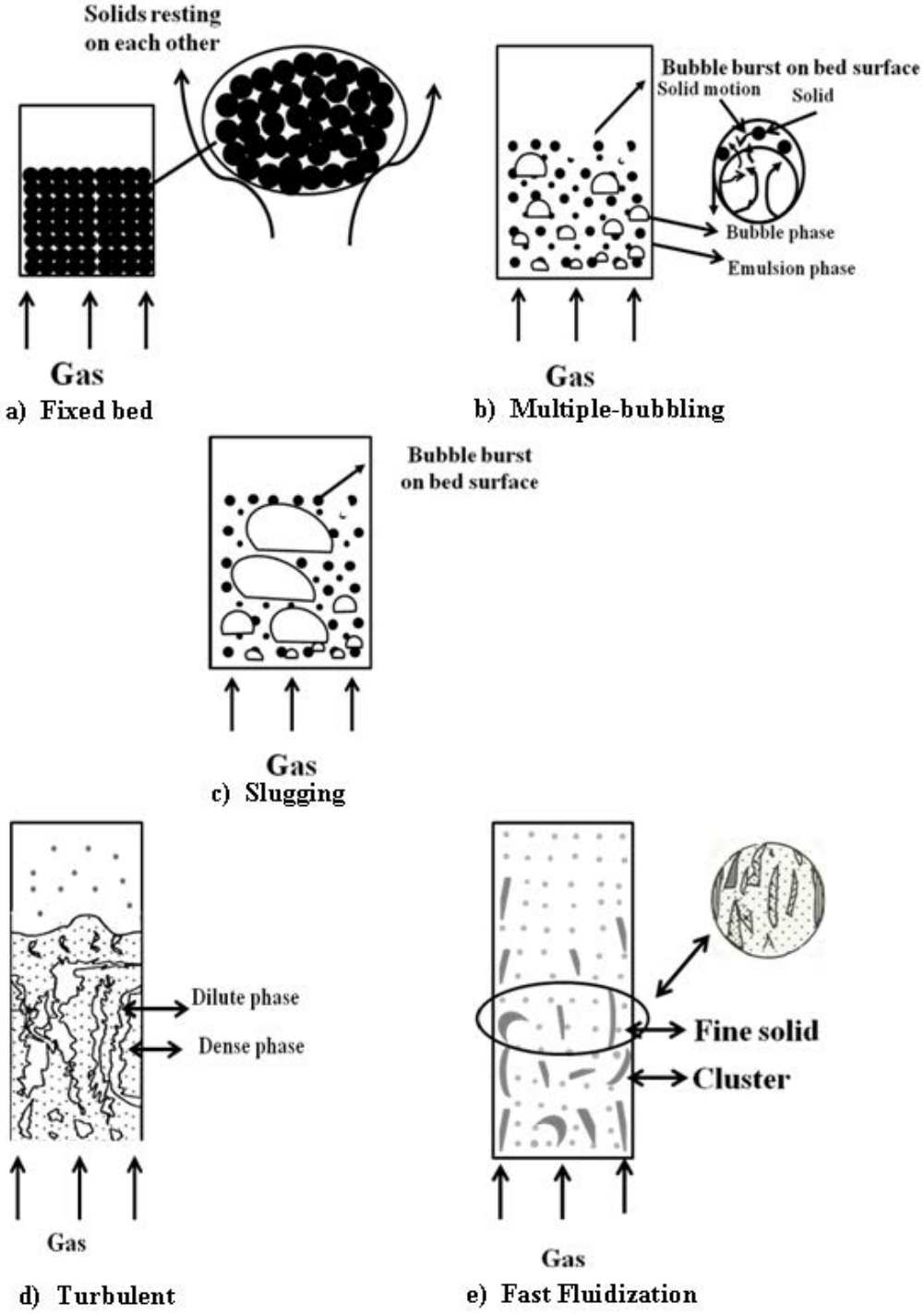


**Figure 5.6 (a) A fixed bed of particles through which gas is flowing (b) A multiple-bubbling fluidization showing gas circulation around bubbles (c) A slugging fluidization regime, (d) A turbulent fluidization regime, (e) fast fluidization showing solid agglomerate.**

As a conclusion on this study concerning to the flow pattern/regime effects in fluidized bed/circulating fluidized bed on $CO_2$ capture by using prepared $K_2CO_3/Al_2O_3$ solid sorbent, the $CO_2$ capture capacities of solid sorbent were highly depending on the flow pattern/regime operated in the reactor. Figure 5.6 shows the maximum $CO_2$ capture capacity at different flow patterns/regimes in fluidized bed/circulating fluidized bed. The fixed bed and slugging fluidization regime show poor $CO_2$ capture capacity. The turbulent fluidization provides advantaged $CO_2$ capture capacity. For multiple bubbling and fast fluidization regimes, results give similar $CO_2$ capture capacity at about 210-230 mg $CO_2$/g $K_2CO_3$. However, considering $CO_2$ removal fraction as shown in Figure 5.3, the fixed bed gives better result, since solid sorbent could removal all the $CO_2$ in feed gas for longer period due to higher gas residence time. It shows that even if the fixed bed have better results for $CO_2$ removal fraction, the capacity of solid sorbents were very poor. The behavior in fixed bed with each solid resting/packing on each other causes the loss of active site of solid sorbent. In the case of multiple-bubbling fluidization regime, the $CO_2$ removal fraction was showing good results even if the gas residence time was lower than for fixed bed. And the $CO_2$ capture capacity of solid sorbent in multiple-bubble was 230 mg $CO_2$/g $K_2CO_3$ or 72 % of theoretical value (about 320 mg $CO_2$/g $K_2CO_3$). It shows that the solid sorbent and gas behavior in multiple-bubbling give better gas-solid sorbent contacting than what is observed for fixed bed. For slugging fluidization, turbulent fluidization and fast fluidization regimes, the $K_2CO_3/Al_2O_3$ solid sorbent could not remove all the $CO_2$ in feed gas or could remove all the $CO_2$ in feed gas only at early beginning of reaction. It means that the gas residence time for these regimes were insufficient. Considering the $CO_2$ capture capacity of solid sorbent, it can be

seen that the $CO_2$ capture capacity in slugging shows very poor as same as fixed bed due to formation of large bubble resulting in losing gas-solid contact area. In the case of fast fluidization for fresh solid sorbent cycle, the $CO_2$ capture capacity results were better than those for fixed bed and slugging regimes, even if the gas residence time was. It implies that the solid sorbent in fast fluidization had more gas-solid contact area due to higher solid dispersion in the bed. In this research, the turbulent fluidization regime provided most promising $CO_2$ capture capacity because of higher back mixing, better surface contact area triggered by the small fine particles, better interaction between gas and solid.

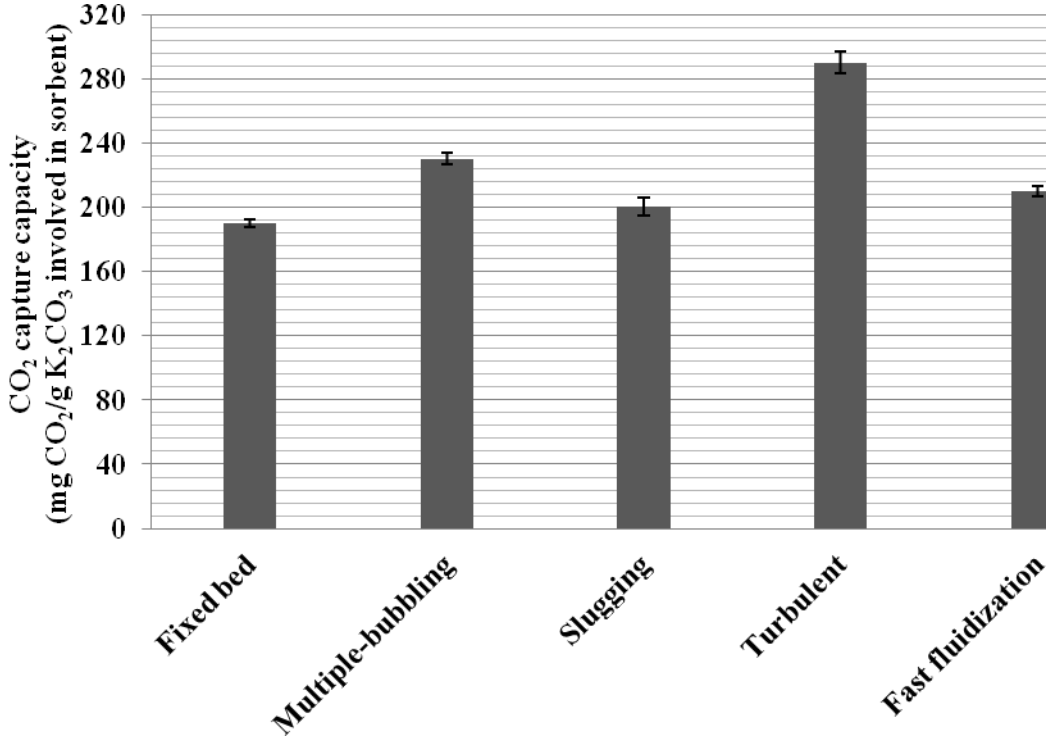


**Figure 5.7 Maximum $CO_2$ capture capacity of $K_2CO_3/Al_2O_3$ solid sorbent at different flow patterns/regimes in fluidized bed/circulating fluidized bed at 60 °C in 12 vol.% of $CO_2$ and 18.4 vol.% of $H_2O$.**

# CHAPTER VI

# REGENERATION CAPACITY RESULTS AND DISCUSSION

In this chapter, the regenerating characteristics are investigated with the temperature of regeneration. $CO_2$ capture capacity of regenerated sorbent is evaluated for multiple cycles of operation.

$CO_2$ adsorption and regeneration process were operated in a multiple-bubbling fluidized bed reactor at constant adsorption temperature of 60 °C and various regeneration temperatures: 150°C, 250°C and 350°C for duration of 60 minutes. $CO_2$ released during regeneration, for these tests, could not be monitored and there was no simple way to determine when regeneration was completed. After regeneration, the $CO_2$ capture capacity of 60 grams regenerated solid sorbents were examined again under 12 vol.% $CO_2$ at dry basis, 18.4 vol.% $H_2O$ and $N_2$ balance being used to evaluate the regeneration capacity of $K_2CO_3/Al_2O_3$. The $K_2CO_3/Al_2O_3$ solid sorbents were used and reused to adsorb $CO_2$ for 5 cycles.

## 6.1 Regeneration Properties

In order to understand the regeneration properties of the $K_2CO_3/Al_2O3$ solid sorbent in details, TPD (Temperature Programmed Desorption) and XRD analyses were performed. Figure 6.1 shows the TPD results of the $K_2CO_3/Al_2O_3$ solid sorbent

directly after $CO_2$ adsorption. TPD tests were carried out by measuring the concentration of $CO_2$ desorbed when the temperature ramping rate was 10 °C/min. Two types of $CO_2$ peaks can be clearly seen and differentiated on the TPD results. One was corresponding to desorption at the initial TPD experiment temperature of 80 °C and the other was corresponding to desorption for temperature above 280 °C. This indicates that there are two kinds of structures observed after $CO_2$ adsorption on $K_2CO_3/Al_2O_3$ solid sorbent as discussed in previous chapter. As shown in the Figure 6.1, the $CO_2$ desorption peak of pure $KHCO_3$ was observed for temperature in the range from 80°C to 150°C. Therefore, the peak observed in TPD results at low temperature above 80°C was probably due to $KHCO_3$ structure as corresponding to temperature range, and the other peak observed above 280 °C was corresponding to the $KAl(CO_3)_2(OH)_2$ formed during $CO_2$ adsorption as mentioned in previous chapter [87,88,91].

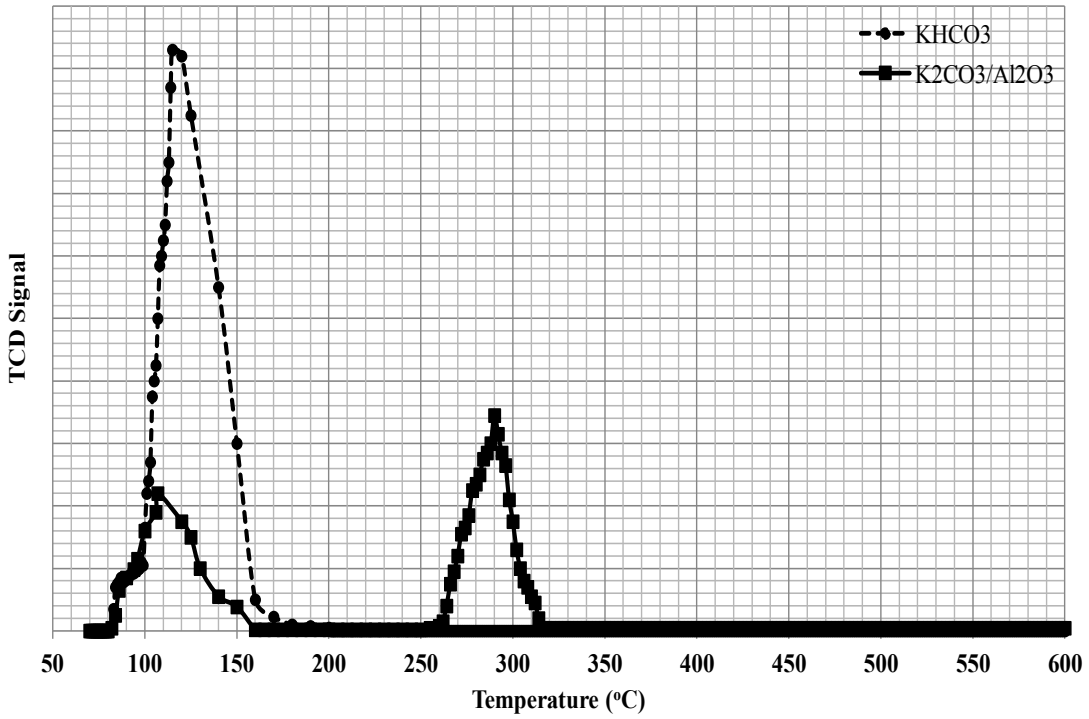


**Figure 6.1. TPD results after $CO_2$ absorption at 60 °C of $KHCO_3$ and $K_2CO_3/AL_2O_3$ solid sorbent.**

## 6.2 Effect of Temperature on Regeneration Property of $K_2CO_3/Al_2O_3$ Solid Sorbent

Five-cycle adsorption tests were conducted with regeneration process operating at various temperatures 150, 250 and 350°C under $N_2$ atmosphere. Figure 6.2 shows the $CO_2$ capture capacity of the five-cycle tests. It can be seen that in the case of 150 and 250 °C of regeneration temperature, the $CO_2$ capture capacity decreased with the increasing cycle number. These results indicate that the $K_2CO_3/Al_2O_3$ solid sorbent could not be completely regenerated at regeneration temperature ragne between 150 °C and 250 °C. However, at 350 °C regeneration temperature, the CO2 capture capacity was maintained during multiple cycles. This means that the spent K2CO3/Al2O3 solid sorbent can be regenerated at 350 °C.

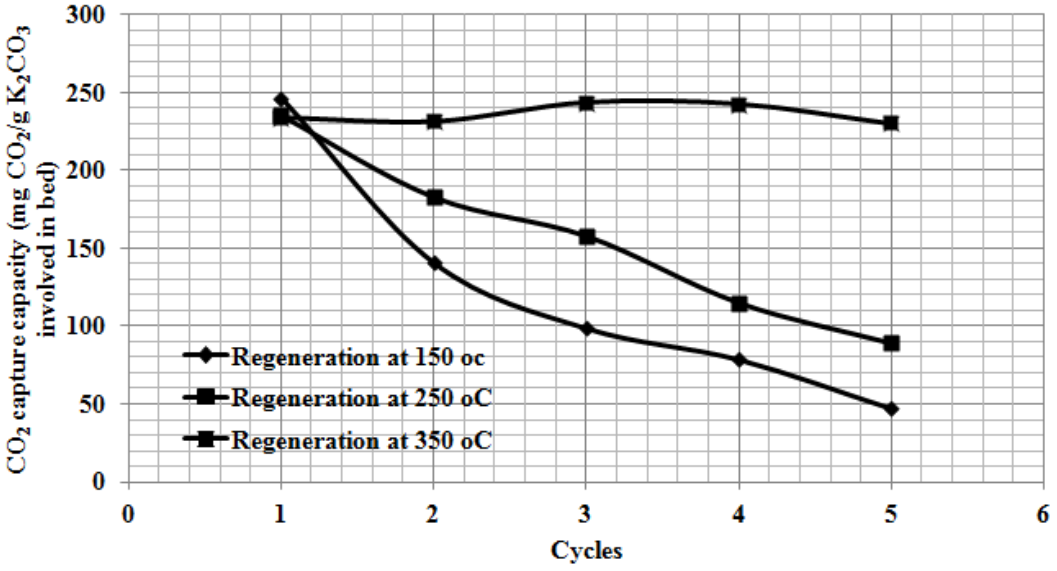


**Figure 6.2 $CO_2$ Capture Capacity of regenerated solid sorbent at various regeneration temperatures: 150 °C, 250 °C and 350 °C for multiple cycles.**

In order to understand the regeneration characteristic of $K_2CO_3/Al_2O_3$ solid sorbent at various regeneration temperature, and evaluate which parameters affect the regeneration, a TPD test of $K_2CO_3/Al_2O_3$ solid sorbent directly after regeneration at three different temperature: 150 °C, 250 °C and 350 °C were carried out to investigate the regeneration characteristic of $K_2CO_3/Al_2O_3$ solid sorbent. The TPD results of $CO_2$ desorption of $K_2CO_3/Al_2O_3$ solid sorbent after regeneration in pure $N_2$ during multiple cycle adsorption/regeneration are shown in Figure 6.3. For $K_2CO_3/Al_2O_3$ solid sorbent after regeneration at 150 °C, it can observe the two different peaks of $KHCO_3$ at temperature at 120 °C and $KAl(CO_3)_2(OH)_2$ at remperature at about 300 °C. It shows that the regeneration capacity of $K_2CO_3/Al_2O_3$ solid sorbent after regeneration at 150 °C decreases due to incompletely regeneration of KHCO3 and $KAl(CO_3)_2(OH)_2$ to original structure like $K_2CO_3$. For solid sorbent after regeneration at 250, it can observe only one peak of $KAl(CO_3)_2(OH)_2$ at about 300 °C of desorption temperature. It implies that the regeneration capacity of solid sorbent after regeneration at 250 °C decreases due to the formation of $KAl(CO_3)_2(OH)_2$, which were not completely. For solid sorbent after regeneration at 350 °C, it observe no desorption peak. It means that solid sorbent can be completely regenerated at 350 °C

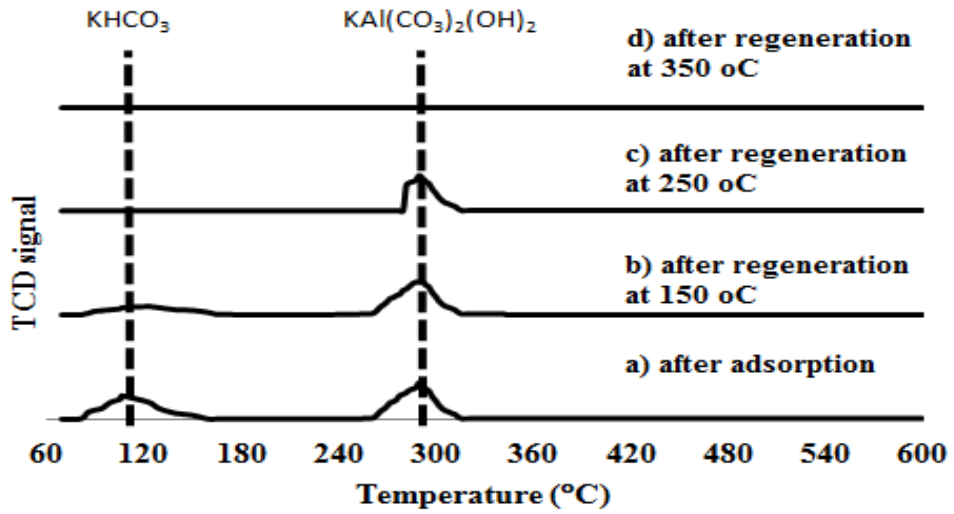


**Figure 6.3 TPD results of $K_2CO_3$ solid sorbent directly after regeneration at various temperatures for a) sorbent after $CO_2$ adsorption, b) after regeneration at 150 °C and c) after regeneration at 250 °C and d) after regeneration at 350 °C.**

To confirm the TPD results, a XRD analysis of the regenerated $K_2CO_3/Al_2O_3$ solid sorbent directly after regeneration was investigated. The XRD results of the regenerated $K_2CO_3/Al_2O_3$ solid sorbent directly after regeneration at various temperatures: 150 °C, 250 °C and 350 °C in $N_2$ is shown in Figure 6.4. It can be seen that the $K_2CO_3/Al_2O_3$ solid sorbent after regeneration at 150 °C in $N_2$ showed the $KHCO_3$ and $KAl(CO_3)_2(OH)_2$ structures. It shows that at 150 °C of regeneration, the capacity of $K_2CO_3/Al_2O_3$ solid sorbent decreased because of mainly two different reasons: firstly, the formation of $KAl(CO_3)_2(OH)_2$ structures occurring during $CO_2$ adsorption and secondly, the $KHCO_3$ was not completely converted to original phase ($K_2CO_3$). In the case of 250 °C, the $K_2CO_3/Al_2O_3$ solid sorbent after regeneration showed only the $KAl(CO_3)_2(OH)_2$ structure. The $KHCO_3$ phase disappeared after regeneration at 250°C compared with results at 150°C. It shows that for regeneration at 250 °C, the capacity of $K_2CO_3/Al_2O_3$ solid sorbent decreased because of the

formation of $KAl(CO_3)_2(OH)_2$ structure occurring during $CO_2$ adsorption [88,89, 91]. For 350 °C of regeneration temperature, it was confirmed that the $KHCO_3$ and $KAl(CO_3)_2(OH)_2$ phase were completely recovered to the $K_2CO_3$ phase at 350 °C by displaying in XRD results of the $K_2CO_3/Al_2O_3$ solid sorbent after regeneration of multiple cycles. This XRD result was also completely consistent with the TPD result mentioned previously.

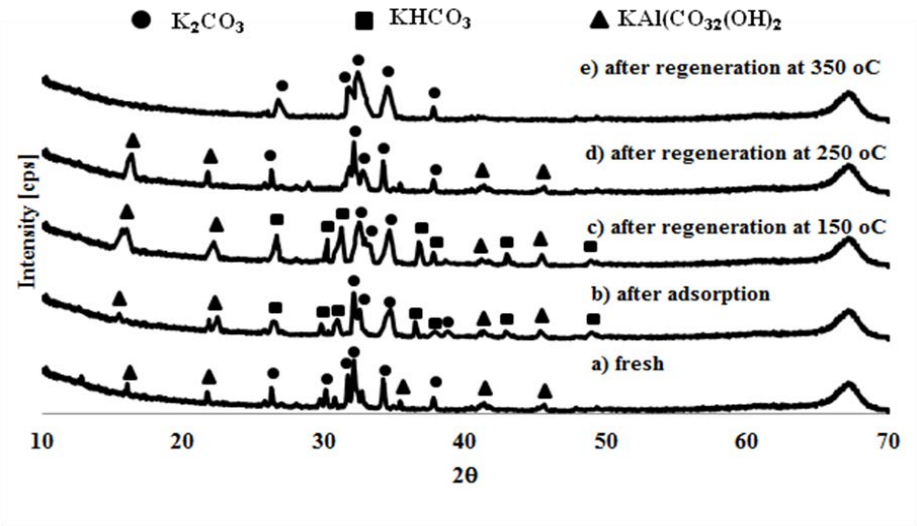


**Figure 6.4 XRD patterns of solid sorbent after regeneration at various regeneration temperature a) fresh sorbent before adsorption b) after $CO_2$ adsorption c) after regeneration at 150 °C, d) after regeneration at 250 °C and e) after regeneration at 350 °C.**

# CHAPTER VII

# CONCLUSIONS AND RECOMMENDATIONS

## 7.1 Flow Pattern/Regime Characterization

In this study, the pressure fluctuation time-series signals at different fluidization regimes were recorded to measure the spontaneous oscillation of hydrodynamic behavior for each regime. From time series analysis, the flow pattern/regime in fluidized bed/circulating fluidized bed can be divided into 6 regimes as the gas velocity increased :

- fixed bed at gas velocity lower than 0.02 m/s,
- multiple-bubbling and slugging fluidization at gas velocity range of 0.02-0.88 m/s,
- Turbulent fluidization at gas velocity range of 0.88-2.20 m/s
- Fast fluidization at gas velocity range of 2.20-2.64 m/s
- Homogenous dilute transport regime at gas velocity higher than 2.64 m/s

However, in order to analyze precisely complex pressure fluctuation time series data, the Fast Fourier Transform method was used to transform time series data into power spectral density in frequency domain. Nowadays with this method, only a few flow regimes have been characterized such as bubbling, turbulent and transition

between bubbling and turbulent regimes. Moreover, the power spectral density characteristic of fluidization was investigated only in a dense bed region at the bottom while flow regimes in different regions were not addressed. Therefore, this study focused to complete the analysis by covering all flow regimes in different part of the riser. From experimental results, it was found that the power spectral density patterns can be used to observe the hydrodynamic behavior in fluidization. The dominant frequency at 1.7 Hz was found to represent the bubble formation action in this research. The oscillation of clusters moving mostly close to the wall had strong effect on the spontaneous pressure fluctuation. The frequency reflecting clusters and fine solid particles moving actions was observed at lower frequency.

In addition, the power spectral density patterns along the riser height of different flow regimes also have been investigated including multiple-bubbling, slugging, turbulent, fast fluidization and homogenous dilute transport regimes. From experimental results, it can be concluded that power spectral density (PSD) pattern is an efficient method to characterize and optimize performances of the flows in different regimes with better understanding of flow behaviors.

For multiple-bubbling fluidization regime, power spectral density patterns had broad band with frequency of 1-4 Hz along the bed height. The power spectral density patterns had narrower peak when the bed height and superficial gas velocity increased. The PSD patterns obtained for a slugging fluidization regime had only one major narrow peak with dominant peak at frequency of 1.7 Hz. This major peak for the slugging regime was observed along the height of the bed and was narrower when the height of the bed increased.

For power spectral density patterns in turbulent fluidization regime, it can be found that there were two different types of power spectral density pattern. At bottom, the dense part, the power spectral density patterns had two distinct peaks with frequency 0-0.50 Hz and 1-2 Hz. At free board part, the power spectral density patterns had narrow peak at frequency lower than 0.25 Hz.

For fast fluidization regime, different patterns were found along the height of the riser. At bottom, the dense part, the power spectral density patterns also had two distinct peaks similar to those in turbulent regime. When increasing the bed height to transition part, there was only single peak at low frequency of 0-0.50 Hz. At the dilute part with the homogeneous flow, the power spectral density patterns had narrow peak at the low frequency 0-0.25 Hz.

For homogeneous dilute transport regime, the power spectral density patterns have narrow peak at the low frequency of 0-0.25 Hz. As the increase of the bed height, the power spectral density peak was narrower.

In this study, the effect of superficial gas velocity on average frequency and average intensity of power spectral density has been investigated. It can be concluded that average frequency decreased when superficial gas velocity was increased. It also can be summarized that the frequency reflecting bubbles formation was at the highest frequency. The average frequency representing the effect of fine particles distributed by gas was at the lowest frequency (0-0.50 Hz). For the particle clusters movement, the average frequency was observed at the frequency between bubbles formation and fine solid particles flowing. The superficial gas velocity has significantly affected the magnitude of power spectral density. At gas velocity lower than transition velocity, the intensity of power spectral density increased with the increase of gas velocity.

Moreover, when gas velocity was increased higher than transition velocity, the intensity of power spectral density decreased with increasing gas velocity.

## 7.2 Effect of Flow Pattern/Regime on $CO_2$ capture

Flow pattern/regime effects in fluidized bed/circulating fluidized bed on $CO_2$ capture by using prepared $K_2CO_3/Al_2O_3$ solid sorbent can be concluded that the $CO_2$ capture capacities of solid sorbent were highly depending on the flow pattern/regime operated in the reactor. The fixed bed and slugging fluidization regimes show poor $CO_2$ capture capacity. The turbulent fluidization provides more advantage on $CO_2$ capture capacity. For multiple bubbling and fast fluidization regimes, results give similar $CO_2$ capture capacity at about 210-230 mg $CO_2$/g $K_2CO_3$ sorbent. However, considering $CO_2$ removal fraction breakthrough, the fixed bed gives better result, since solid sorbent could removal all the $CO_2$ content in feed gas for longer period due to longer gas residence time. It shows that even if the fixed bed have better results for breakthrough curve, the solid sorbent utilization was very poor. The behavior of the fixed bed with each solid resting/packing on each other causes the loss of effective surface area active site on solid sorbent. In the case of multiple-bubbling fluidization regime, the $CO_2$ removal fraction breakthrough curve was showing good results even if the gas residence time was lower than the fixed bed. And the $CO_2$ capture capacity of solid sorbent in multiple-bubble was 230 mg $CO_2$/g $K_2CO_3$ being 72 % of theoretical value (about 320 mg $CO_2$/g $K_2CO_3$). It shows that the solid sorbent and gas behavior in multiple-bubbling give better gas-solid sorbent contacting than what was observed for the fixed bed. For slugging fluidization, turbulent fluidization and fast

fluidization regimes, the $K_2CO_3/Al_2O_3$ solid sorbent could not remove all the $CO_2$ in feed gas or could remove all the $CO_2$ in feed gas only at beginning of reaction. It means that the gas residence time for these regimes were insufficient. Considering the $CO_2$ capture capacity of solid sorbent, it can be seen that the $CO_2$ capture capacity in slugging shows very poor as same as the fixed bed due to the formation of large bubble resulting in loss of gas-solid contact area. In the case of fast fluidization for fresh solid sorbent cycle, the $CO_2$ capture capacity results were better than the fixed bed and slugging regimes, even if the gas residence time was much faster. It means that the solid sorbent in fast fluidization regime had more gas-solid contact area due to higher solid dispersion in the bed. In this study, the turbulent fluidization regime provided most promising $CO_2$ capture capacity because of higher back mixing, better surface contact area triggered by the small fine particles, better exchange contacting between gas and solid.

## 7.3 Effect of Regeneration Temperature on Regneration Capacity of $K_2CO_3/Al_2O_3$ Sorbent

For the regeneration characteristic of $K_2CO_3/Al_2O_3$ solid sorbent at various regeneration temperature such as 150, 250 and 350 °C, it can be concluded that the $CO_2$ regeneration capacity of $K_2CO_3/Al_2O_3$ solid sorbent after regeneration at low temperature less than 150 °C decreased with the number of cycles due to the formation of $KHCO_3$ and $KAl(CO_3)_2(OH)_2$, which were not completely recovered to the original structure, like $K_2CO_3$ phase. When regeneration temperature was increased to 250 °C, the $CO_2$ regeneration capacity of $K_2CO_3/Al_2O_3$ solid sorbent was

still observed to be reducing with the number of cycles, because the $KAl(CO_3)_2(OH)_2$ structure was still not recovered completely to the original structure while $KHCO_3$ structure was completely recovered. At the regeneration temperature of 350 °C, the $CO_2$ regeneration capacity of $K_2CO_3/Al_2O_3$ solid sorbent was maintained during multiple cycle number as a result of the complete desorption of both $KHCO_3$ and $KAl(CO_3)_2(OH)_2$ formation. Therefore, the $K_2CO_3/Al_2O_3$ solid sorbent should be regenerated at temperature higher than 350 °C in order to use the solid sorbent repeatedly.

## 7.4 Recommendation

Although, 35% $K_2CO_3/Al_2O_3$ solid sorbent for $CO_2$ capture prepared by conventional impregnation method in this study exhibited an excellent adsorption performance to remove $CO_2$ from wet flue gas. Nevertheless it was introduced to lab-scale $CO_2$ capture system as shown in this dissertation. To apply the concept to the $CO_2$ capture from flue gas emitted by industries, more parameters need to be investigated. Moreover, the complete regeneration is at very high temperature. However, 35% $K_2CO_3/Al_2O_3$ solid sorbent is one of the potential candidates in $CO_2$ capture from flue gas for a post-combustion system.

# REFERENCES


[1] Metz, B., Davidso, O., de Coninck H.C., Loos M., and Meyer, L. Working Group III of The Intergovermental Panel on Climate Change. Cambridge United Kingdom and New York : Cambridge University Press, 2005.

[2] Kuuskraa, V. Review and Evaluation of The $CO_2$ Capture Project by The Technology Advisory Board. Carbon Dioxide Capture for Storage in Deep Geologic Formations 1(2005) : 37-46.

[3] Liang, Y., and Harrison, D.P. Carbon Dioxide Capture Using Dry Sodium-Based Sorbents. Energy & Fuels 18(2004) : 569-575.

[4] Hayashi, H., Taniuchi, J., Furuyashiki, N., Sugiyama, S., Hirano, S., Shigemoto, N., and Nonaka, T. Efficient Recovery of Carbon Dioxide form Flue Gases of Coal-Fired Power Plants by Cyclic Fixed-Bed Operations Over $K_2CO_3$-on-Carbon. Industrial & Engineering Chemistry Research 37(1998) : 185-191.

[5] Lee, Y., and Harrion, D.P. Carbon Dioxide Capture Dry Sodium-Based Sorbents. Energy & Fuel 18(2004) : 569-575.

[6] Lu, D.Y., Hughes, R.W., and Anthony E.J. Ca-based Sorbent Looping Combustion for $CO_2$ Capture in Pilot-Scale Dual Fluidized Bed. Fuel Processing Techonlogy 89(2008) : 1386-1395.

[7] Lim, K.S., Zhu, J.X. and, Grace, J.R. Hydrodynamics of Gas-Solid Fluidization. Internation Journal of Multiphase Flow 21(1995) : 141-193.

[8] Eimer, D. Post-Combustion $CO_2$ Separation Technology Summary. Carbon Dioxide Capture for Storage in Deep Geologic Formations 1(2005) : 91-97.

[9] Miracca, I., Aasen, K.I., Brownscombe, T., Gerdes, K., and Simmonds, M. Oxyfuel Combustion for $CO_2$ Capture Technology Summary. Carbon Dioxide Capture for Storage in Deep Geologic Formations 1(2005) : 441-449.

[10] Amdersem, H. Pre-Combustion Decarbonisation Technology Summary. Carbon Dioxide Capture for Storage in Deep Geologic Formations 1(2005) : 203-211.

[11] Suzuki, M., and Kenzi, T. Method for Selective Separation of Carbon Dioxide from Waste Gas of Combustion. U.S. Patent No.: 5667561, Issued Sep.16, 1997.

[12] Strazisar, B., Brian, R., Anderson, R.R., and White, C.M. Degradation of Monoethanolamine Used in Carbon Dioxide Capture from Flue Gas of a Coal-fired Electric Power Generating Station. In Proceeding of First National Conference on Carbon Sequestration, Washington, 2001.

[13] Chakravarti S., Gupta, A., and Amitabh, B. Advanced Technology for the Capture of Carbon Dioxide from Flue Gases. In Proceeding of First National Conference on Carbon Sequestration, Washington, 2001.

[14] Kohl, A.O., and Nielsen, R.B. Gas Purification. Houston, USA : Gulf Publishing Co., 2000.

[15] Chapel, D.G., Mariz, C.L., and Ernet, J. Recovery of $CO_2$ from Flue Gases: Commercial Trends. In the Annual Meeting of the Canadian Society of Chemical Engineering Saskatoon, Canada, 1999.

[16] Mimura, T., Satsumi, S., Iijima, M., and Mistsuoka, S. Development on Energy Saving Technology for Flue Gas Carbon Dioxide Recovery by the Chemical Adsorption Method and Seam Syste m in Power Plant. Riemer, P., Eliasson, B., Wokan, A. (eds.), Greenhouse gas control technologies, United Kingdom : Elsevier Science Ltd., 1999.

[17] White, C.M., Strazisar, B.R., Granite, E.J., and Hoffman, J.S. Separation and Capture of $CO_2$ from Large Stationary Sources and Sequestration in Geological Formations-coalbds and Deep Saline Aquifers. Journal of the Air and Waste Management Association 53 (2003) : 645-715.

[18] Leites, I.L., Sama, D.A., and Lior, N. The Theory and Practice of Energy Saving in the Chemical Industry: Some Methods for Reducing Thermodynamic Irreversibility in Chemical Technology Processes. Energy 28(2003) : 55-97.

[19] Nsakala, Y.N., and others. Engineering Feasibility of $CO_2$ Capture on an Existing US Coal-fired Power Plant. In First National Conference on Carbon Sequestration, Washington, DC, 2001.

[20] Raterman, K., and others. A Vertex Contactor for Carbon Dioxide Separation. In Proceedings of First National Conference on Carbon Sequestration, Washington, DC, 2001.

[21] Ishibashi, M., Otake, K., Kanamori, S., and Yasutake, A. Study on $CO_2$ Removal Technology from Flue Gas of Thermal Power Plant by Physical Adsorption Method. In Riemer, P., Eliasson, B., Wokaun, A. (eds.), Greenhouse Gas Control Technologies, pp.96-100. UK : Elsevier Science, Ltd., 1999.

[22] Yokoyama T. Japanese R&D on $CO_2$ Capture. In Gale, J., and Kaya, Y. (eds.), Greenhouse Gas Control Technologies, Proceeding of the 6th International Conference on Greenhouse Gas Control Technologies, pp.13-18. UK : Elsevier Science Ltd., 2003.

[23] CO2CRC2011. The Australian Government's Cooprative Research Centre Program. $CO_2$ Capture/Separation Technologies : Adsorption. [Online] 2002. Available from : http://www.co2crc.com. [2012, May 15]

[24] Carlos, A.G., and Rodrigues, A.E. Electric Swing Adsorption for CO2 Removal from Flue Gases. International Journal of Greenhouse Gas Control 2(2007) : 194-202.

[25] Shimizu, T., Hirama, T., Hosoda, H., Inagaki, K.M., and Tejima, K. A Twin Fluidized-bed Reactor for Removal of $CO_2$ from Combustion Processes (Part A). Transuction IChemE Journal 77 (1999) : 62-68.

[26] Curran, G.P., Fink, C.E., and Gorin, E. Carbon Dioxide-acceptor Gasification Process. Advance in Chemistry Series 69(1967) : 141-165.

[27] Abanades, J.C, Anthony, E.J. Alvarez, D., Lu, D.Y, and Salvador, C. Capture of CO2 from Combustion Gases in a Fluidized Bed of CaO. American Institution of Chemical Engineering Journal 50(2004) : 1614-1622.

[28] Abanades, J.C., Rubin, E.S., and Anthony, E.J. Sorbent Cost and Performance in $CO_2$ Capture Systems. Industrial and Engineering Chemistry Research 43(2004b) : 3462-3466.

[29] Nakagawa, K., and Ohashi, T. A Novel Method of $CO_2$ Capture from High Temperature Gases. Journal of the Electrochemical Society 145(1998) : 1344-1346.

[30] Gray, M.L, Soong, Y, Champagne, K.J., Pennline, H., Baltrus, J.P., and Stevens, R.W. Improved Immobilized Carbon Dioxide Capture Sorbents. Fuel Process Technology 86(2005) : 1449-1455.

[31] Pannocchia, G., Puccini, M., Seggiani, M., and Vitolo, S. Experimental and Modeling Studies on High Temperature Capture of CO2 Using Lithium Zirconate Based Sorbent. Industrial Engineering Chemistry Reseach 46(2007) : 6696-6706.

[32] Abanades, J.C., and Alvarez, D. Conversion Limits in the Reaction of $CO_2$ with Lime. Energy and Fuels 2(2003) : 308-315.

[33] United State of America Department of Energy. The Dry Carbonate Sorbent Technology for Co2 Removal From Flue Gas of Existing Coal-fired Power Plants. [Online]. 2002. Available from : http://www.netl.doe.gov/dry-regen.html [2012, May 16]

[34] Jose, D.F., Timothey, F., Sean, P., Howard, M., and Rameshwar, D.S. Advances in CO2 Capture Technology-The U.S. Department of Energy's Carbon Sequestration Program. International Jornal of Greenhouse Gas Control 2(2008) : 9-20.

[35] CO2CRC2011. The Australian Government's Cooprative Research Centre Program. $CO_2$ Capture/Separation Technologies : Membranes. [Online]. 2002. Available from : http://www.co2crc.com.au/c.html [2012, May 15]

[36] Herzog, H., Golomb, D., and Zemba, S. Feasility, Modeling and Economics of Sequestering Power Plant CO2 Emission in the Deep Ocean. Environmental Progress 10(1991) : 64-74.

[37] Van der Sluijs, J.P., Hendriks, C.A., and Blok K. Feasibility of Polymer Membranes for Carbon Dioxide Recovery from Flue Gases. Energy Conversion Management 33(1991) : 429-436.

[38] Feron, P.H.M. Membranes for Carbon Dioxide Recovery from Power Plant. In Carbon Dioxide Chemistry. In Paul, C.M. (eds.), Environmental Issues Journal. Cambridge, United Kingdom : The Royal Society of Chemistry, 1996.

[39] Barbara, M. Zero emissions Technologies for Fossil Fuels. In Technology Status Report IEA Working Party on Fossil Fuels. Cambridge, United Kingdom : The Royal Society of Chemistry, 2002.

[40] CO2CRC2011. The Australian Government's Cooprative Research Centre Program. $CO_2$ Capture images : Membranes. [Online]. 2002. Available from : http://www.co2crc.com.au.php [2012, May 15]

[41] Kumar, P.S., Hogendoorn, J.A., Feron, P.H.M., and Versteeg, G.F. New Absorption Liquids for the Removal of CO2 from Dilute Gas Streams Using Membrane Contactors. Chemical Engineering Science 57 (2002) : 1639-1650.

[42] Xu, Z-K., Xiao, L., Wang, J., Xu, Y.-Y. Separation and Fixation of Carbon Dioxide Using Polymeric Membrane Contactor. In Proceedings of First National Conference on Carbon Sequestration, Washington, DC, 2001.

[43] Allan, H., and Nimalan, G. Cryogenic CO2 Capture in Natural Gas. Energy Procedia 1(2009) : 697-706.

[44] Ushotsearches. Cryogenic $CO_2$ Capture to Control Climate Change Emission. [Online]. 2000. Available from : http://sustainablees.com [2012 May 15]

[45] Rowan University. Fluidization. [Online]. 2006. Available from : http://users.rowan.edu/~hesketh/0906-309/laboratories/fluidizedbed flow regimes rev1.pdf [2012, May 15]

[46] Fluidized Bed Team. Fluidized bed. [Online]. 2003. Available from : http://fluidizedbed2008.webs.com [2012, May 15].

[47] Haeri, S., and Shrimpton, J.S. A Mesoscopic Description of Polydispersed Particle Laden Turbulent Flows. Progress in Energy and Combustion Science. 37 (2011) : 716-740.

[48] Radic, D., Jovovic, A., Povlovic, M.,and Karamarkovic, V. The Influence of Variable Operation Condition on the Design and Exploitation of Fly Ash Pneumatic Transport Systems in the Thermal Power Plants. Brazilian Journal of Chemical Engineering 25(2008) : 123-135.

[49] Sau, D.C., Mohanty, S., and Biswal, K.C. Minimum Fluidization Velocities and Maximum Bed Pressure Drops for Gas-solid Tapered Fluidized Beds. Chemical Engineering Journal 132(2007) : 151-157.

[50] J.R. Grace, and Bi, H. Circulating Fluidized Beds, New York : Blackie Academic and Professional, 1997.

[51] Daleffe, R.V., and Freire, J.T. Analysis of the Fluid-dynamic Behavior of Fluidized and Vibrofluidized Bed Containing Glycerol. Brazilian Jornal of Chemical Engineering 21(2004) : 35-46.

[52] Parise, M.R., Taranto, O.P., Kurka, P.R.G., and Benetti, L.B. Detection of the Minimum Gas Velocity Region Using Gaussian Spectral Pressure Distribution in a Gas-Solid Fluidized Bed. Powder Technology 182(2008) : 453-458.

[53] Basu, P. In Combustion and gasification in fluidized beds. United State : Taylor and Francis Group, 2006.

[54] Kunii, D., and Levenspiel, O. Fluidization Engineering. United State : Ed. Butterworth-Heinemann. E.U.A., 1991.

[55] Constantineau, J.P., Grace, J.R., Lim, C.J., and Richards, G.G. Generalized Bubbling-Slugging Fluidized Bed Reactor Model. Chemical Engineering Science 63 (2007) : 70-81.

[56] Geldart, D. Gas Fluidization Technology. New York : John Willey & Sons Inc., 1986.

[57] Stewart, P.S.B., and Davidison, J.F. Slug Flow in Fluidized Beds. Powder Technology 1(1967) : 61-70.

[58] Yang, R.T., Shen, M.-S., and Steinberg, M. Fluidized-Bed Combustion of Coal with Lime Additives : Catalytic Sultation of Lime with Iron Compounds and Coal Ash. Environmental Science & Technology 12(1978) : 915-918.

[59] Bi, H.T., Ellis, N., Abba, I.A., and Grace, J.R. A State-of-the-Art Review of Gas-Solid Turbulent Fluidization. Chemical Engineering Science 55 (2000) : 4789-4825.

[60] Basu, P. Bubbling to Turbulent Transition. Combustion and gasification in fluidized beds. United State : Taylor and Francis Group, 2006.

[61] Yerushalmi, J., and Cankurt, N.T. Further Studies of the Regimes of Fluidization. Powder Technology 24(1979) : 187-205.

[62] Jiradilok, V., Gidaspow, D., Damronglerd, S., Koves, J.W., and Mostofi, R. Kinetic Theory Based CFD Simulation of Turbulent Fluidization of FCC Particle in Riser. Chemical Engineering Science 61(2006) : 5544-5559.

[63] Yang, W.C. Mechanistic Models for Transitions between Regimes of Fluidization. American Institution Chemical Engineering Journal 30(1984) : 1025-1027.

[64] Jin, Y., Yu, Z.O., Wang, Z.W., and Cai, P. A Criterion for Transition from Bubbling to Turbulent Fluidization: In østergaard, K., and Sørensen, A. (eds.), Fluidization Volume, New York: Engineering Foundation, 1996.

[65] Lee, G.S., and Kim, S.D. Pressure Fluctuation in Turbulent Fluidized Beds. Journal of Chemical Engineering of Japan 21(1988) : 515-521.

[66] Leu, L.-P., Huang, J.-W., and Gua, B.-B. Axial Pressure Distribution in Turbulent Fluidized Beds. In Proceedings of the Second Asian Conference on Fluidized-bed and Three-phase Reactor, 1990.

[67] Horio, M. Circulating Fluidized Bed Technology III. Oxford: Pergamon, 1991.

[68] Nakajima, M., Harada, M., Asai, M., Yamazaki, R., and Jimbo, G. Circulating Fluidized bed III. Oxford: Pergamon Press, 1991.

[69] Dunham, G.E., Mann, M.D., and Grewal, N.S. Dependence of Transition to Turbulent Fluidization on Static Bed Depth in a Fluidized Bed. In Avidan, A.A. (eds.), Preprints of the Fourth International Conference on Circulating Fluidized Beds, Pennsylvania, 1993.

[70] Bi, H.T., and Grace, J.R. Effects of Measurement Method on Velocities Used to Demarcate the Transition to Turbulent Fluidization. Chemical Engineering Journal 57(1995) : 261-271.

[71] Chehbouni, A., Chaouki, Guy, J. and Klvana, C. D. Characterization of the Flow Transition between Bubbling and Turbulent Fluidization. Industrail and Engineering Chemistry Research 33(1994) : 1889-1898.

[72] Smolders, K., and Baeyens, J. Gas Fluidized Bed Operating at High Velocities: a Critical Revieof Occurring Regimes. Powder Technology 119 (2001) : 269-291.

[73] Li, J., and Kwauk, M. Fluidization, New York : Plenum Press, 1980.

[74] Schnitzlein, M.G., and Weinstein, H., Flow Characterization in High Velocity Fluidized Beds Using Pressure Fluctuations. Chemical Engineering Science 43 (1988) : 2605-2614.

[75] Perales, J.F., Coll, T., Llop, M.F., Puigjaner, L., Arnaldos, J., and Casal, J. Circulating Fluidized Bed Technology III. Oxford : Pergamon Press, 1991.

[76] Takeuchi, H., and Hirama, T., A Quantitative Definition and Flow Regime Diamgram for Fast Fluidization. Powder Technology 47(1986) : 195-199.

[77] Kumthanasup, S., and Nitivattananon, S. Effect of Air Flowrate on Particle Velocity Profile in a Circulating Fluidize Bed. Korean Journal Chemical Engineering 24(2007) : 851-855.

[78] Namkung, W. Kim, W.S., and Kim, D.S. Flow Regimes and Axial Pressure Profiles in a Circulating Fluidized Bed. Chemical Engineering Journal 72(1999) : 245-252.

[79] Lee, G.S., and Kim, S.D. Bed Expansion Characteristics and Transition Velocity in Turbulent Fluidized Beds. Powder Technology 62(1990b) : 201-215.

[80] Bi, H.T., and Fan, L.S. Existence of Turbulent Regime in Gas-Solid Fluidization. American Institution Chemical Engineering Journal 38 (1992) : 297-301.

[81] Adanez, J., de Diego, L.F., and Gayan, P. Transport Velocities of Coal and Sand Particles. Powder Technology 77 (1993) : 61-68.

[82] Tsukada, M., Nakanishi, D., and Horio, M. The Effect of Pressure on the Phase Transition from Bubbling to Turbulent Fluidization. International Journal of Multiphase Flow 19(1993) : 27-34.

[83] Chehbouni, A., Chaouki, J., Guy, C., and Klvana, D. Effect de Different Parmetress sur les Vitesses du Transition de la Fluidization en Regime Turbulent. Cannadian Journal of Chemical Engineering 73 (1995) : 41-50.

[84] Geldart, D., Types of Gas Fluidization. Powder Technology 7(1973) : 285-292.

[85] Pandit, K.J., Wang, X.S., and Rhodes, M.J. Study of Geldart's Group A Behavior using the Discrete Elecment Method Simulation. Powder Technology 160 (2005): 7-14.

[86] Sharonov, V.E., Okunev, A.G., and Aristov, Y. Kinetics of Carbon Dioxide Sorption by The Composite Material $K_2CO_3$ in $Al_2O_3$. Reaction Kinetics and Catalysis Letters 2(2004) : 363-369.

[87] Kee, C.S., and others. Novel Regenerable Potassium-Based Dry Sorbents for $CO_2$ Capture at Low Temperature. Jornal of Molecular Catalysis B: Enzymatic 56(2009) : 179-184.

[88] Seo, Y., Jo, S-H., Ryu, H-J., Bae, H.D., Ryu, K.C., and Yi, C.K. Effect of Water Pretreatment on $CO_2$ Capture Using a Potassium-Based Solid Sorbent in a Bubbling Fluidized Bed Reactor. Korean Journal of Chemical Engineering 24(2007) : 457-460.

[89] Yi, C.-K., Jo, S.-H., Seo, Y., Lee, J.-B., and Ryu, C.-K. Continuous Operation of The Potassium-Based Dry Sorbent $CO_2$ Capture Process with Two Fluidized-Bed Reactors. Internation Journal of Greenhouse Gas Control 1(2007) : 31-36.

[90] Park, Y.C., Jo, S,-H., Park, K.W., Park, Y.S., and Yi, C.-K. Effect of Bed Height on The Carbon Dioxide Capture by Carbonation/Regeneration Cyclic Operation Using Dry Potassium-Based Sorbets. Korean Journal of Chemical Engineering 26(2009) : 874-878.

[91] Zhao, C., Chen, X., and Zhao, C. Effect of Crystal Structure on $CO_2$ Capture Characteristics of Dry Potassium-Based Sorbents. Chemosphere 75(2009) 1401-1404.

[92] Cui, H., and Chaouki, J. Effect of Temperature on Local Two-Phase Flow Structure in Bubbling and Turbulent Fluidized Beds of FCC Particles. Chemical Engineering Science 59(2004) : 3413-3422.

[93] Monazam, E.R., Shadle, L.J., Mei, J.S., and Spenik, J. Identification and Characteristics of Different Flow Regimes in a Circulating Fluidized Bed. Power Technology 155(2005) : 17-25.

[94] Ellis, H., Bi, H.T., Lim, C.J., and Grace, J.R. Hydrodynamics of Turbulent Fluidized Bed of Different Diameter. Power Technology 141(2004) : 124-136.

[95] Zhu, H., and Zhu, J. Comparative Study of Flow Structures in a Circulating-Turbulent Fluidized Bed. Chemical Engineering Science 63(2008) : 2920-2927.

[96] Detamore, M.S., Swanson, M.A., Frender, K.R., and Hrenya, C.M. A Kinetice-theory Analysis of the Scale-up of Circulating Fluidized beds. Powder Technology 116(2001) : 190-203.

[97] van der Meer, E.H., Thopre, R.B. and Davidson, J.F. Dimensionless Groups for Practicable Similarity of Circulating Fluidized Beds. Chemical Engineering Science 54(1999) : 5369-5376.

[98] Lee, S.C., Choi, B.Y., Ryu, C.K., Ahn, Y.S., Lee, T.J., and Kim, J.C. The Effect of Water on the Activation and the CO2 Capture Capacities of Alkali Metal-based Sorbents. Korean of Journal Chemical Engineering 23(2006) : 374-379.

[99] Zu, G., and Gao, S. Necessary Parameters for Specifying the Hydrodynamics of Circulating Fluidized Bed Riser-a Review and Reiteration. Power Technology 137 (2003) : 63-76.

[100] Kim, S.W., Kirbas, G., Bi, H., Lim, C.J., and Grace, J.R. Flow Structure and Thickness of Annular Downflow Layer in a Circulating Fluidized Bed Riser. Power Technology 142 (2004) : 48-58.

[101] Matsumoto, T., and Suzuki, M. Statistical Analysis of Fluctuations of Froth Pressure on Perforated Plates without Downcomers. International Journal of Multiphase Flow 10 (1984) : 217-228.

[102] Johnsson, F., Zijerveld, R.C., Schouten, J.C., van den Bleek, C.M., and Leckner, B. Characterization of Fluidization Regime by Time-Series Analysis of Pressure Fluctuations. International Journal of Multiphase Flow 26 (2000) : 663-715.

[103] Abbasi, M., Sotudeh-Gharebagh, R., Mostoufi, N., and Mahjoob. M.J. Non-Intrusive Monitoring of Bubbles in a Gas-Solid Fluidized Bed Using Vibration Signature Analysis. Power Technology 196 (2009) : 278-285.

[104] Felipe, C.A.S., and Rocha, S.C.S. Prediction of Minimum Fluidization Velocity of Gas-solid Fluidized Beds by Pressure Fluctuation Measurements-Analysis of the Standard Deviation Methodology. Powder Technology 174 (2007) : 104-113.

[105] Wen, C.Y., and Yu, Y.H. A Generalized Method for Predicting the Minimum Fluidization Velocity. American Institution of Chemical Engineers Journal 12 (1966) : 610-612.

[106] Jin, Y., Yu, Z.Q., Wang, Z.W., and Cai, P. Multi-phase Chemical Reaction Engineering and Technology (Part I), Tsinghua University Academic Work : Tsinghua University Press, 2006.

[107] Lee, G.S, and Kim, S.D. Pressure Fluctuation in Turbulent Fluidized Beds. Journal of Chemical Engineering of Japan 21(1988) : 515-521.

[108] Luckos, A., and den Hoed, P. Fluidization and Flow Regimes of Titaniferous Solids. Industrial & Engineering Chemistry Research 43 (2004) : 5645-5652.

[109] Lee, G.S. and Kim, S.D. Bed Expansion Characteristics and Transition Velocity in Turbulent Fluidized Beds. Powder Technology 62 (1990) : 207-215.

[110] Bi, X. Flow Regime Transition in Gas-Solid Fluidization and Transport. Doctoral dissertation, Department of Chemical Engineering, Faculty of Engineering, University of British Columbia, 1994.

[111] Parssinen, J.H., and Zhu, J.-X. Particle Velocity and Flow Development in a Long and High-Flux Circulation Fluidized Bed Riser. Chemical Engineering Science 56 (2001) : 5295-5303.

[112] Issangya, A.S., Bai, D., Bi, H.T., Zhu, J., and Grace, J.R. Suspension Densities in a High-Density Circulating Fluidized Bed Riser. Chemical Engineering Science 54 (1999**) :** 5451-5460.

[113] Bi, H.T. A Critical Review of the Complex Pressure Fluctuation Phenomenon in Gas-Solid Fluidized Beds. Chemical Engineering Science 62 (2007) : 3473-3493.

[114] Van der Schaaf, J., Schouten, I.C., Johnsson, F., and van der Bleek, C.M.. Multiple Modes of Bed Mass Oscillation in Gas-Solid Fluidized Bed. In Proceeding of the 15th International Conference on Fluidized bed Combustion, Georgia, 1999.

[115] Yang, T-Y., and Leu, L-P. Study of Transition Velocities from Bubbling to Turbulent Fluidization by Statistic and Wavelet Multi-Resolution Analysis on Absolute Pressure Fluctuations. Chemical Engineering Science 63 (2008) : 1950-1970.

[116] Brzic, D., Ahchieva, D., Piskova, E., Heinrich, S., and Grbavcic, Z. Hydrodynamics of Shallow Fluidized Bed of Coarse Particles. Chemical Engineering Journal 114 (2005) 47-54.

[117] Child, M.S. Molecular Collision Theory. London: Acadamic Press, 1974

# APPENDIES

# APPENDIX A

## $CO_2$ ADSORPTION RAW DATA

Table A-1 operating condition used for $CO_2$ adsorption at 50 °C of reaction temperature.

| | | |
|---|---|---|
| % conc. $CO_2$ at input | 12 | %vol. |
| Solid inventory: | 60 | g |
| $K_2CO_3$ weight | 21 | g |
| Riser Temperature: | 50 | °C |
| Temperature | 323 | K |
| Feed gas flow rate ($F_{input}$) | 0.8 | l/min |
| Pressure | 1 | atm |
| Gas constant | 0.082 | (l/atm)/(g mole/K) |

Table A-2 row data for $CO_2$ adsorption at 50 °C of reaction temperature.

| Time | % conc.$CO_{2\ output}$ | $Flow_{output}$ | $[CO_2]_{output}$ | F | $V_{CO2ads}$ | $W_{CO2\ ads}$ |
|---|---|---|---|---|---|---|
| (Minute) | %vol. | l/min | l/min | - | l/min | g/min |
| 0 | 0.00 | 0.70 | 0.000 | 1.000 | 0.120 | 0.159 |
| 2 | 0.00 | 0.70 | 0.000 | 1.000 | 0.120 | 0.159 |
| 4 | 0.00 | 0.70 | 0.000 | 1.000 | 0.120 | 0.159 |
| 4.5 | 0.00 | 0.70 | 0.000 | 1.000 | 0.120 | 0.159 |
| 5 | 0.00 | 0.70 | 0.000 | 1.000 | 0.120 | 0.159 |
| 6 | 0.00 | 0.70 | 0.000 | 1.000 | 0.120 | 0.159 |
| 7 | 0.00 | 0.70 | 0.000 | 1.000 | 0.120 | 0.159 |
| 8 | 1.19 | 0.71 | 0.009 | 0.911 | 0.109 | 0.145 |
| 9 | 2.26 | 0.72 | 0.016 | 0.830 | 0.100 | 0.132 |
| 10 | 2.87 | 0.73 | 0.021 | 0.782 | 0.094 | 0.125 |
| 11 | 4.31 | 0.74 | 0.032 | 0.669 | 0.080 | 0.107 |
| 12 | 7.18 | 0.76 | 0.055 | 0.431 | 0.052 | 0.069 |
| 13 | 8.52 | 0.77 | 0.066 | 0.315 | 0.038 | 0.050 |
| 14 | 9.53 | 0.78 | 0.074 | 0.225 | 0.027 | 0.036 |
| 15 | 9.76 | 0.78 | 0.076 | 0.205 | 0.025 | 0.033 |
| 16 | 10.18 | 0.79 | 0.080 | 0.167 | 0.020 | 0.027 |
| 17 | 10.39 | 0.79 | 0.082 | 0.148 | 0.018 | 0.024 |
| 18 | 10.88 | 0.79 | 0.086 | 0.104 | 0.012 | 0.017 |
| 19 | 11.05 | 0.79 | 0.088 | 0.088 | 0.011 | 0.014 |
| 20 | 11.19 | 0.79 | 0.089 | 0.075 | 0.009 | 0.012 |
| 21 | 11.28 | 0.79 | 0.090 | 0.067 | 0.008 | 0.011 |
| 22 | 11.31 | 0.79 | 0.090 | 0.064 | 0.008 | 0.010 |
| 23 | 11.40 | 0.80 | 0.091 | 0.056 | 0.007 | 0.009 |

| | | | | | | |
|---|---|---|---|---|---|---|
| 25 | 11.45 | 0.80 | 0.091 | 0.051 | 0.006 | 0.008 |
| 30 | 11.45 | 0.80 | 0.091 | 0.051 | 0.006 | 0.008 |
| 35 | 11.46 | 0.80 | 0.091 | 0.050 | 0.006 | 0.008 |
| 40 | 11.47 | 0.80 | 0.091 | 0.049 | 0.006 | 0.008 |
| 45 | 11.45 | 0.80 | 0.091 | 0.051 | 0.006 | 0.008 |
| 50 | 11.47 | 0.80 | 0.091 | 0.049 | 0.006 | 0.008 |
| 55 | 11.51 | 0.80 | 0.092 | 0.045 | 0.005 | 0.007 |
| 60 | 11.97 | 0.80 | 0.096 | 0.003 | 0.000 | 0.001 |

Table A-3 operating condition used for $CO_2$ adsorption at 60 °C of reaction temperature.

| | | |
|---|---|---|
| % conc. $CO_2$ at input | 12 | %vol. |
| Solid inventory: | 60 | g |
| $K_2CO_3$ weight | 21 | grams |
| Riser Temperature: | 60 | °C |
| Temperature | 333 | K |
| Feed gas flow rate ($Flow_{input}$) | 0.8 | l/min |
| Pressure | 1 | atm |
| Gas constant | 0.082 | (l/atm)/(g mole/K) |

Table A-4 row data for $CO_2$ adsorption at 60 °C of reaction temperature.

| Time | % conc.$CO_{2\ output}$ | $Flow_{output}$ | $[CO_2]_{output}$ | F | $V_{CO2ads}$ | $W_{CO2\ ads}$ |
|---|---|---|---|---|---|---|
| (Minute) | %vol. | l/min | l/min | - | l/min | g/min |
| 0 | 0.00 | 0.70 | 0.000 | 1.000 | 0.120 | 0.193 |
| 2 | 0.00 | 0.70 | 0.000 | 1.000 | 0.120 | 0.193 |
| 4 | 0.00 | 0.70 | 0.000 | 1.000 | 0.120 | 0.193 |
| 4.5 | 0.00 | 0.70 | 0.000 | 1.000 | 0.120 | 0.193 |
| 5 | 0.00 | 0.70 | 0.000 | 1.000 | 0.120 | 0.193 |
| 6 | 0.00 | 0.70 | 0.000 | 1.000 | 0.120 | 0.193 |
| 7 | 0.00 | 0.70 | 0.000 | 1.000 | 0.120 | 0.193 |
| 8 | 0.00 | 0.70 | 0.000 | 1.000 | 0.120 | 0.193 |
| 9 | 0.00 | 0.70 | 0.000 | 1.000 | 0.120 | 0.193 |
| 10 | 0.00 | 0.70 | 0.000 | 1.000 | 0.120 | 0.193 |
| 11 | 0.00 | 0.70 | 0.000 | 1.000 | 0.120 | 0.193 |
| 12 | 0.00 | 0.70 | 0.000 | 1.000 | 0.120 | 0.193 |
| 13 | 0.00 | 0.70 | 0.000 | 1.000 | 0.120 | 0.193 |
| 14 | 0.00 | 0.70 | 0.000 | 1.000 | 0.120 | 0.193 |
| 15 | 0.00 | 0.70 | 0.000 | 1.000 | 0.120 | 0.193 |
| 16 | 0.00 | 0.70 | 0.000 | 1.000 | 0.120 | 0.193 |
| 17 | 0.72 | 0.71 | 0.005 | 0.947 | 0.114 | 0.183 |
| 18 | 2.09 | 0.72 | 0.015 | 0.843 | 0.101 | 0.163 |
| 19 | 3.13 | 0.73 | 0.023 | 0.762 | 0.091 | 0.147 |
| 20 | 4.80 | 0.74 | 0.036 | 0.628 | 0.075 | 0.122 |
| 21 | 5.46 | 0.75 | 0.041 | 0.575 | 0.069 | 0.111 |
| 22 | 6.60 | 0.76 | 0.050 | 0.480 | 0.058 | 0.093 |
| 23 | 7.74 | 0.77 | 0.059 | 0.382 | 0.046 | 0.074 |
| 25 | 9.60 | 0.78 | 0.075 | 0.219 | 0.026 | 0.042 |
| 30 | 10.49 | 0.79 | 0.083 | 0.139 | 0.017 | 0.027 |
| 35 | 10.96 | 0.79 | 0.087 | 0.096 | 0.012 | 0.019 |
| 40 | 11.22 | 0.79 | 0.089 | 0.072 | 0.009 | 0.014 |
| 45 | 11.45 | 0.80 | 0.091 | 0.051 | 0.006 | 0.010 |
| 50 | 11.47 | 0.80 | 0.091 | 0.049 | 0.006 | 0.010 |
| 55 | 11.51 | 0.80 | 0.092 | 0.045 | 0.005 | 0.009 |
| 60 | 11.97 | 0.80 | 0.096 | 0.003 | 0.000 | 0.001 |

Table A-5 operating condition used for $CO_2$ adsorption at 70 °C of reaction temperature.

| | | |
|---|---|---|
| % conc. $CO_2$ at input | 12 | %vol. dry basis |
| Solid inventory: | 60 | g |
| $K_2CO_3$ weight | 21 | grams |
| Riser Temperature: | 70 | °C |
| Temperature | 343 | K |
| Feed gas flow rate ($Flow_{input}$) | 0.8 | l/min |
| Pressure | 1 | atm |
| Gas constant | 0.082 | (l/atm)/(g mole/K) |

Table A-6 row data for $CO_2$ adsorption at 70 °C of reaction temperature.

| Time | % conc.$CO_{2\ output}$ | $Flow_{output}$ | $[CO_2]_{output}$ | F | $V_{CO2ads}$ | $W_{CO2\ ads}$ |
|---|---|---|---|---|---|---|
| (Minute) | %vol. | l/min | l/min | - | l/min | g/min |
| 0 | 0.00 | 0.70 | 0.000 | 1.000 | 0.120 | 0.188 |
| 2 | 0.00 | 0.70 | 0.000 | 1.000 | 0.120 | 0.188 |
| 4 | 0.00 | 0.70 | 0.000 | 1.000 | 0.120 | 0.188 |
| 4.5 | 0.00 | 0.70 | 0.000 | 1.000 | 0.120 | 0.188 |
| 5 | 0.00 | 0.70 | 0.000 | 1.000 | 0.120 | 0.188 |
| 6 | 0.00 | 0.70 | 0.000 | 1.000 | 0.120 | 0.188 |
| 7 | 0.00 | 0.70 | 0.000 | 1.000 | 0.120 | 0.188 |
| 8 | 0.00 | 0.70 | 0.000 | 1.000 | 0.120 | 0.188 |
| 9 | 0.00 | 0.70 | 0.000 | 1.000 | 0.120 | 0.188 |
| 10 | 0.00 | 0.70 | 0.000 | 1.000 | 0.120 | 0.188 |
| 11 | 0.00 | 0.70 | 0.000 | 1.000 | 0.120 | 0.188 |
| 12 | 0.00 | 0.70 | 0.000 | 1.000 | 0.120 | 0.188 |
| 13 | 0.00 | 0.70 | 0.000 | 1.000 | 0.120 | 0.188 |
| 14 | 0.00 | 0.70 | 0.000 | 1.000 | 0.120 | 0.188 |
| 15 | 0.00 | 0.70 | 0.000 | 1.000 | 0.120 | 0.188 |
| 16 | 0.76 | 0.71 | 0.005 | 0.944 | 0.113 | 0.177 |
| 17 | 2.09 | 0.72 | 0.015 | 0.843 | 0.101 | 0.158 |
| 18 | 3.18 | 0.73 | 0.023 | 0.759 | 0.091 | 0.142 |
| 19 | 5.11 | 0.74 | 0.038 | 0.603 | 0.072 | 0.113 |
| 20 | 6.43 | 0.76 | 0.049 | 0.494 | 0.059 | 0.093 |
| 21 | 8.03 | 0.77 | 0.062 | 0.357 | 0.043 | 0.067 |
| 22 | 8.87 | 0.77 | 0.069 | 0.284 | 0.034 | 0.053 |
| 23 | 9.37 | 0.78 | 0.073 | 0.239 | 0.029 | 0.045 |
| 25 | 9.92 | 0.78 | 0.078 | 0.191 | 0.023 | 0.036 |
| 30 | 10.52 | 0.79 | 0.083 | 0.136 | 0.016 | 0.026 |
| 35 | 10.78 | 0.79 | 0.085 | 0.113 | 0.014 | 0.021 |
| 40 | 11.01 | 0.79 | 0.087 | 0.091 | 0.011 | 0.017 |
| 45 | 11.44 | 0.80 | 0.091 | 0.052 | 0.006 | 0.010 |
| 50 | 11.47 | 0.80 | 0.091 | 0.049 | 0.006 | 0.009 |
| 55 | 11.48 | 0.80 | 0.091 | 0.049 | 0.006 | 0.009 |
| 60 | 11.48 | 0.80 | 0.091 | 0.049 | 0.006 | 0.009 |

Table A-7 operating condition used for $CO_2$ adsorption at 80 °C of reaction temperature.

| | | |
|---|---|---|
| % conc. $CO_2$ at input | 12 | %vol. dry basis |
| Solid inventory: | 60 | g |
| $K_2CO_3$ weight | 21 | grams |
| Riser Temperature: | 80 | °C |
| Temperature | 353 | K |
| Feed gas flow rate ($Flow_{input}$) | 0.8 | l/min |
| Pressure | 1 | atm |
| Gas constant | 0.082 | (l/atm)/(g mole/K) |

Table A-8 row data for $CO_2$ adsorption at 80 °C of reaction temperature.

| Time | % conc.$CO_{2\ output}$ | $Flow_{output}$ | $[CO_2]_{output}$ | F | $V_{CO2ads}$ | $W_{CO2\ ads}$ |
|---|---|---|---|---|---|---|
| (Minute) | %vol. | l/min | l/min | - | l/min | g/min |
| 0 | 0.00 | 0.70 | 0.000 | 1.000 | 0.120 | 0.182 |
| 2 | 0.00 | 0.70 | 0.000 | 1.000 | 0.120 | 0.182 |
| 4 | 0.00 | 0.70 | 0.000 | 1.000 | 0.120 | 0.182 |
| 4.5 | 0.00 | 0.70 | 0.000 | 1.000 | 0.120 | 0.182 |
| 5 | 0.00 | 0.70 | 0.000 | 1.000 | 0.120 | 0.182 |
| 6 | 0.00 | 0.70 | 0.000 | 1.000 | 0.120 | 0.182 |
| 7 | 0.00 | 0.70 | 0.000 | 1.000 | 0.120 | 0.182 |
| 8 | 0.00 | 0.70 | 0.000 | 1.000 | 0.120 | 0.182 |
| 9 | 0.00 | 0.70 | 0.000 | 1.000 | 0.120 | 0.182 |
| 10 | 0.00 | 0.70 | 0.000 | 1.000 | 0.120 | 0.182 |
| 11 | 0.00 | 0.70 | 0.000 | 1.000 | 0.120 | 0.182 |
| 12 | 0.00 | 0.70 | 0.000 | 1.000 | 0.120 | 0.182 |
| 13 | 0.00 | 0.70 | 0.000 | 1.000 | 0.120 | 0.182 |
| 14 | 0.90 | 0.71 | 0.006 | 0.934 | 0.112 | 0.170 |
| 15 | 1.76 | 0.72 | 0.013 | 0.869 | 0.104 | 0.158 |
| 16 | 3.19 | 0.73 | 0.023 | 0.757 | 0.091 | 0.138 |
| 17 | 4.50 | 0.74 | 0.033 | 0.653 | 0.078 | 0.119 |
| 18 | 5.74 | 0.75 | 0.043 | 0.551 | 0.066 | 0.101 |
| 19 | 7.44 | 0.76 | 0.057 | 0.408 | 0.049 | 0.074 |
| 20 | 8.61 | 0.77 | 0.067 | 0.307 | 0.037 | 0.056 |
| 21 | 9.23 | 0.78 | 0.072 | 0.252 | 0.030 | 0.046 |
| 22 | 9.53 | 0.78 | 0.074 | 0.225 | 0.027 | 0.041 |
| 23 | 10.24 | 0.79 | 0.080 | 0.162 | 0.019 | 0.030 |
| 25 | 11.17 | 0.79 | 0.089 | 0.077 | 0.009 | 0.014 |
| 30 | 11.11 | 0.79 | 0.088 | 0.083 | 0.010 | 0.015 |
| 35 | 10.82 | 0.79 | 0.086 | 0.109 | 0.013 | 0.020 |
| 40 | 11.46 | 0.80 | 0.091 | 0.050 | 0.006 | 0.009 |
| 45 | 11.48 | 0.80 | 0.091 | 0.049 | 0.006 | 0.009 |
| 50 | 11.48 | 0.80 | 0.091 | 0.049 | 0.006 | 0.009 |
| 55 | 11.48 | 0.80 | 0.091 | 0.049 | 0.006 | 0.009 |
| 60 | 11.48 | 0.80 | 0.091 | 0.049 | 0.006 | 0.009 |

Table A-9 operating condition used for $CO_2$ adsorption at 90 °C of reaction temperature.

| | | |
|---|---|---|
| % conc. $CO_2$ at input | 12 | %vol. dry basis |
| Solid inventory: | 60 | g |
| $K_2CO_3$ weight | 21 | g |
| Riser Temperature: | 90 | °C |
| Temperature | 363 | K |
| Feed gas flow rate ($Flow_{input}$) | 0.8 | l/min |
| Pressure | 1 | atm |
| Gas constant | 0.082 | (l/atm)/(g mole/K) |

Table A-10 row data for $CO_2$ adsorption at 80 °C of reaction temperature.

| Time | % conc.$CO_{2\ output}$ | $Flow_{output}$ | $[CO_2]_{output}$ | F | $V_{CO2ads}$ | $W_{CO2\ ads}$ |
|---|---|---|---|---|---|---|
| (Minute) | %vol. | l/min | l/min | - | l/min | g/min |
| 0 | 0.00 | 0.70 | 0.000 | 1.000 | 0.120 | 0.177 |
| 2 | 0.00 | 0.70 | 0.000 | 1.000 | 0.120 | 0.177 |
| 4 | 0.00 | 0.70 | 0.000 | 1.000 | 0.120 | 0.177 |
| 4.5 | 0.00 | 0.70 | 0.000 | 1.000 | 0.120 | 0.177 |
| 5 | 0.00 | 0.70 | 0.000 | 1.000 | 0.120 | 0.177 |
| 6 | 0.00 | 0.70 | 0.000 | 1.000 | 0.120 | 0.177 |
| 7 | 0.00 | 0.70 | 0.000 | 1.000 | 0.120 | 0.177 |
| 8 | 0.00 | 0.70 | 0.000 | 1.000 | 0.120 | 0.177 |
| 9 | 0.00 | 0.70 | 0.000 | 1.000 | 0.120 | 0.177 |
| 10 | 0.00 | 0.70 | 0.000 | 1.000 | 0.120 | 0.177 |
| 11 | 0.00 | 0.70 | 0.000 | 1.000 | 0.120 | 0.177 |
| 12 | 1.47 | 0.72 | 0.011 | 0.891 | 0.107 | 0.158 |
| 13 | 2.88 | 0.73 | 0.021 | 0.782 | 0.094 | 0.139 |
| 14 | 8.32 | 0.77 | 0.064 | 0.332 | 0.040 | 0.059 |
| 15 | 9.23 | 0.78 | 0.072 | 0.252 | 0.030 | 0.045 |
| 16 | 9.80 | 0.78 | 0.077 | 0.201 | 0.024 | 0.036 |
| 17 | 10.29 | 0.79 | 0.081 | 0.157 | 0.019 | 0.028 |
| 18 | 9.79 | 0.78 | 0.077 | 0.202 | 0.024 | 0.036 |
| 19 | 10.34 | 0.79 | 0.081 | 0.153 | 0.018 | 0.027 |
| 20 | 10.88 | 0.79 | 0.086 | 0.104 | 0.012 | 0.018 |
| 21 | 10.93 | 0.79 | 0.087 | 0.099 | 0.012 | 0.018 |
| 22 | 11.02 | 0.79 | 0.087 | 0.091 | 0.011 | 0.016 |
| 23 | 11.05 | 0.79 | 0.088 | 0.088 | 0.011 | 0.016 |
| 25 | 11.22 | 0.79 | 0.089 | 0.072 | 0.009 | 0.013 |
| 30 | 11.25 | 0.79 | 0.089 | 0.070 | 0.008 | 0.012 |
| 35 | 11.45 | 0.80 | 0.091 | 0.051 | 0.006 | 0.009 |
| 40 | 11.43 | 0.80 | 0.091 | 0.053 | 0.006 | 0.009 |
| 45 | 11.44 | 0.80 | 0.091 | 0.052 | 0.006 | 0.009 |
| 50 | 11.47 | 0.80 | 0.091 | 0.049 | 0.006 | 0.009 |
| 55 | 11.48 | 0.80 | 0.091 | 0.049 | 0.006 | 0.009 |
| 60 | 11.48 | 0.80 | 0.091 | 0.049 | 0.006 | 0.009 |

Table A-11 operating condition used for $CO_2$ adsorption at 7.4% vol. of water content.

| | | |
|---|---|---|
| % Conc. $CO_2$ at input | 12 | %vol., dry basis |
| Solid inventory: | 60 | g |
| $K_2CO_3$ weight | 21 | g |
| Riser Temperature: | 60 | °C |
| Temperature | 333 | K |
| Feed gas flow rate ($F_{input}$) | 0.8 | l/min |
| Pressure | 1 | atm |
| Water concentration | 7.4 | %vol. |
| Mole fraction between vapor and $CO_2$, $x_v/x_c$ | 0.58 | - |
| Gas constant | 0.082 | (l/atm)/(g mole/K) |

Table A-12 row data for $CO_2$ adsorption at 7.4 % vol. of water content.

| Time | % conc.$CO_{2\ output}$ | $Flow_{output}$ | $[CO_2]_{output}$ | F | $V_{CO2ads}$ | $W_{CO2\ ads}$ |
|---|---|---|---|---|---|---|
| (Minute) | %vol. | l/min | l/min | - | l/min | g/min |
| 0 | 0.00 | 0.70 | 0.000 | 1.000 | 0.120 | 0.193 |
| 2 | 0.00 | 0.70 | 0.000 | 1.000 | 0.120 | 0.193 |
| 4 | 0.00 | 0.70 | 0.000 | 1.000 | 0.120 | 0.193 |
| 4.5 | 0.00 | 0.70 | 0.000 | 1.000 | 0.120 | 0.193 |
| 5 | 0.00 | 0.70 | 0.000 | 1.000 | 0.120 | 0.193 |
| 6 | 0.00 | 0.70 | 0.000 | 1.000 | 0.120 | 0.193 |
| 7 | 0.00 | 0.70 | 0.000 | 1.000 | 0.120 | 0.193 |
| 8 | 0.00 | 0.70 | 0.000 | 1.000 | 0.120 | 0.193 |
| 9 | 3.70 | 0.73 | 0.027 | 0.718 | 0.086 | 0.139 |
| 10 | 6.05 | 0.75 | 0.045 | 0.526 | 0.063 | 0.102 |
| 11 | 8.36 | 0.77 | 0.064 | 0.329 | 0.039 | 0.064 |
| 12 | 9.04 | 0.78 | 0.070 | 0.269 | 0.032 | 0.052 |
| 13 | 9.64 | 0.78 | 0.075 | 0.216 | 0.026 | 0.042 |
| 14 | 10.03 | 0.78 | 0.079 | 0.181 | 0.022 | 0.035 |
| 15 | 10.10 | 0.78 | 0.079 | 0.175 | 0.021 | 0.034 |
| 16 | 10.15 | 0.79 | 0.080 | 0.169 | 0.020 | 0.033 |
| 17 | 10.26 | 0.79 | 0.081 | 0.160 | 0.019 | 0.031 |
| 18 | 10.40 | 0.79 | 0.082 | 0.147 | 0.018 | 0.028 |
| 19 | 10.50 | 0.79 | 0.083 | 0.138 | 0.017 | 0.027 |
| 20 | 10.63 | 0.79 | 0.084 | 0.127 | 0.015 | 0.024 |
| 21 | 10.94 | 0.79 | 0.087 | 0.098 | 0.012 | 0.019 |
| 22 | 11.27 | 0.79 | 0.089 | 0.068 | 0.008 | 0.013 |
| 23 | 11.40 | 0.80 | 0.091 | 0.056 | 0.007 | 0.011 |
| 25 | 11.44 | 0.80 | 0.091 | 0.052 | 0.006 | 0.010 |
| 30 | 11.60 | 0.80 | 0.092 | 0.037 | 0.004 | 0.007 |
| 35 | 11.66 | 0.80 | 0.093 | 0.032 | 0.004 | 0.006 |
| 40 | 11.74 | 0.80 | 0.094 | 0.024 | 0.003 | 0.005 |
| 45 | 11.96 | 0.80 | 0.096 | 0.004 | 0.000 | 0.001 |
| 50 | 12.00 | 0.80 | 0.096 | 0.000 | 0.000 | 0.000 |
| 55 | 12.00 | 0.80 | 0.096 | 0.000 | 0.000 | 0.000 |
| 60 | 12.00 | 0.80 | 0.096 | 0.000 | 0.000 | 0.000 |

Table A-13 operating condition used for $CO_2$ adsorption at 13.5 % vol. of water content.

| | | |
|---|---|---|
| % conc. $CO_2$ at input | 12 | %vol. dry basis |
| Solid inventory: | 60 | g |
| $K_2CO_3$ weight | 21 | g |
| Riser Temperature: | 60 | °C |
| Temperature | 333 | K |
| Feed gas flow rate ($F_{input}$) | 0.8 | l/min |
| Pressure | 1 | atm |
| Water concentration | 13.5 | %vol. |
| Mole fraction between vapor and $CO_2$, $x_v/x_c$ | 1.08 | - |
| Gas constant | 0.082 | (l/atm)/(g mole/K) |

Table A-14 row data for $CO_2$ adsorption at 13.5 % vol. of water content.

| Time | % conc.$CO_{2\ output}$ | $Flow_{output}$ | $[CO_2]_{output}$ | F | $V_{CO2ads}$ | $W_{CO2\ ads}$ |
|---|---|---|---|---|---|---|
| (Minute) | %vol. | l/min | l/min | - | l/min | g/min |
| 0 | 0.00 | 0.70 | 0.000 | 1.000 | 0.120 | 0.193 |
| 2 | 0.00 | 0.70 | 0.000 | 1.000 | 0.120 | 0.193 |
| 4 | 0.00 | 0.70 | 0.000 | 1.000 | 0.120 | 0.193 |
| 4.5 | 0.00 | 0.70 | 0.000 | 1.000 | 0.120 | 0.193 |
| 5 | 0.00 | 0.70 | 0.000 | 1.000 | 0.120 | 0.193 |
| 6 | 0.00 | 0.70 | 0.000 | 1.000 | 0.120 | 0.193 |
| 7 | 0.00 | 0.70 | 0.000 | 1.000 | 0.120 | 0.193 |
| 8 | 0.00 | 0.70 | 0.000 | 1.000 | 0.120 | 0.193 |
| 9 | 0.00 | 0.70 | 0.000 | 1.000 | 0.120 | 0.193 |
| 10 | 2.07 | 0.72 | 0.015 | 0.845 | 0.101 | 0.163 |
| 11 | 3.87 | 0.73 | 0.028 | 0.704 | 0.084 | 0.136 |
| 12 | 6.04 | 0.75 | 0.045 | 0.527 | 0.063 | 0.102 |
| 13 | 9.03 | 0.78 | 0.070 | 0.270 | 0.032 | 0.052 |
| 14 | 10.54 | 0.79 | 0.083 | 0.135 | 0.016 | 0.026 |
| 15 | 10.84 | 0.79 | 0.086 | 0.107 | 0.013 | 0.021 |
| 16 | 11.13 | 0.79 | 0.088 | 0.080 | 0.010 | 0.016 |
| 17 | 11.64 | 0.80 | 0.093 | 0.034 | 0.004 | 0.007 |
| 18 | 11.64 | 0.80 | 0.093 | 0.033 | 0.004 | 0.006 |
| 19 | 11.67 | 0.80 | 0.093 | 0.030 | 0.004 | 0.006 |
| 20 | 11.70 | 0.80 | 0.093 | 0.028 | 0.003 | 0.005 |
| 21 | 11.75 | 0.80 | 0.094 | 0.024 | 0.003 | 0.005 |
| 22 | 11.78 | 0.80 | 0.094 | 0.021 | 0.002 | 0.004 |
| 23 | 11.80 | 0.80 | 0.094 | 0.018 | 0.002 | 0.004 |
| 25 | 11.85 | 0.80 | 0.095 | 0.014 | 0.002 | 0.003 |
| 30 | 11.90 | 0.80 | 0.095 | 0.009 | 0.001 | 0.002 |
| 35 | 11.93 | 0.80 | 0.095 | 0.007 | 0.001 | 0.001 |
| 40 | 11.98 | 0.80 | 0.096 | 0.002 | 0.000 | 0.000 |
| 45 | 11.99 | 0.80 | 0.096 | 0.001 | 0.000 | 0.000 |
| 50 | 12.00 | 0.80 | 0.096 | 0.000 | 0.000 | 0.000 |
| 55 | 12.00 | 0.80 | 0.096 | 0.000 | 0.000 | 0.000 |
| 60 | 12.00 | 0.80 | 0.096 | 0.000 | 0.000 | 0.000 |

Table A-15 operating condition used for $CO_2$ adsorption at 18.5 % vol. of water content.

| | | |
|---|---|---|
| % conc. $CO_2$ at input | 12 | %vol. dry basis |
| Solid inventory: | 60 | g |
| $K_2CO_3$ weight | 21 | g |
| Riser Temperature: | 60 | °C |
| Temperature | 333 | K |
| Feed gas flow rate ($F_{input}$) | 0.8 | l/min |
| Water concentration | 18.5 | %vol. |
| Mole fraction between vapor and $CO_2$, $x_v/x_c$ | 1.50 | - |
| Pressure | 1 | atm |
| Gas constant | 0.082 | (l/atm)/(g mole/K) |

Table A-16 row data for $CO_2$ adsorption at 18.5 % vol. of water content.

| Time | % conc.$CO_{2\ output}$ | $Flow_{output}$ | $[CO_2]_{output}$ | F | $V_{CO2ads}$ | $W_{CO2\ ads}$ |
|---|---|---|---|---|---|---|
| (Minute) | %vol. | l/min | l/min | - | l/min | g/min |
| 0 | 0.00 | 0.70 | 0.000 | 1.000 | 0.120 | 0.193 |
| 2 | 0.00 | 0.70 | 0.000 | 1.000 | 0.120 | 0.193 |
| 4 | 0.00 | 0.70 | 0.000 | 1.000 | 0.120 | 0.193 |
| 4.5 | 0.00 | 0.70 | 0.000 | 1.000 | 0.120 | 0.193 |
| 5 | 0.00 | 0.70 | 0.000 | 1.000 | 0.120 | 0.193 |
| 6 | 0.00 | 0.70 | 0.000 | 1.000 | 0.120 | 0.193 |
| 7 | 0.00 | 0.70 | 0.000 | 1.000 | 0.120 | 0.193 |
| 8 | 0.00 | 0.70 | 0.000 | 1.000 | 0.120 | 0.193 |
| 9 | 0.00 | 0.70 | 0.000 | 1.000 | 0.120 | 0.193 |
| 10 | 0.00 | 0.70 | 0.000 | 1.000 | 0.120 | 0.193 |
| 11 | 0.00 | 0.70 | 0.000 | 1.000 | 0.120 | 0.193 |
| 12 | 0.00 | 0.70 | 0.000 | 1.000 | 0.120 | 0.193 |
| 13 | 0.00 | 0.70 | 0.000 | 1.000 | 0.120 | 0.193 |
| 14 | 0.00 | 0.70 | 0.000 | 1.000 | 0.120 | 0.193 |
| 15 | 0.00 | 0.70 | 0.000 | 1.000 | 0.120 | 0.193 |
| 16 | 0.00 | 0.70 | 0.000 | 1.000 | 0.120 | 0.193 |
| 17 | 0.34 | 0.71 | 0.002 | 0.975 | 0.117 | 0.189 |
| 18 | 1.14 | 0.71 | 0.008 | 0.916 | 0.110 | 0.177 |
| 19 | 3.28 | 0.73 | 0.024 | 0.751 | 0.090 | 0.145 |
| 20 | 5.02 | 0.74 | 0.037 | 0.611 | 0.073 | 0.118 |
| 21 | 5.70 | 0.75 | 0.043 | 0.555 | 0.067 | 0.107 |
| 22 | 6.90 | 0.76 | 0.052 | 0.454 | 0.055 | 0.088 |
| 23 | 8.10 | 0.77 | 0.062 | 0.352 | 0.042 | 0.068 |
| 25 | 10.04 | 0.78 | 0.079 | 0.180 | 0.022 | 0.035 |
| 30 | 10.37 | 0.79 | 0.082 | 0.150 | 0.018 | 0.029 |
| 35 | 11.46 | 0.80 | 0.091 | 0.050 | 0.006 | 0.010 |
| 40 | 11.73 | 0.80 | 0.094 | 0.025 | 0.003 | 0.005 |
| 45 | 11.97 | 0.80 | 0.096 | 0.002 | 0.000 | 0.000 |
| 50 | 11.99 | 0.80 | 0.096 | 0.001 | 0.000 | 0.000 |
| 55 | 12.00 | 0.80 | 0.096 | 0.000 | 0.000 | 0.000 |
| 60 | 12.00 | 0.80 | 0.096 | 0.000 | 0.000 | 0.000 |

Table A-17 operating condition used for $CO_2$ adsorption at 22.5 % vol. of water content.

| | | |
|---|---|---|
| % conc. $CO_2$ at input | 12 | %vol. basis |
| Solid inventory: | 60 | g |
| $K_2CO_3$ weight | 21 | g |
| Riser Temperature: | 60 | °C |
| Temperature | 333 | K |
| Feed gas flow rate ($F_{input}$) | 0.8 | l/min |
| Water concentration | 22.5 | %vol. |
| Mole fraction between vapor and $CO_2$, $x_v/x_c$ | 1.88 | - |
| Pressure | 1 | atm |
| Gas constant | 0.082 | (l/atm)/(g mole/K) |

Table A-18 row data for $CO_2$ adsorption at 22.5 % vol. of water content.

| Time | % conc.$CO_{2\ output}$ | $Flow_{output}$ | $[CO_2]_{output}$ | F | $V_{CO2ads}$ | $W_{CO2\ ads}$ |
|---|---|---|---|---|---|---|
| (Minute) | %vol. | l/min | l/min | - | l/min | g/min |
| 0 | 6.00 | 0.75 | 0.045 | 0.530 | 0.064 | 0.102 |
| 2 | 6.60 | 0.76 | 0.050 | 0.480 | 0.058 | 0.093 |
| 4 | 7.56 | 0.76 | 0.058 | 0.398 | 0.048 | 0.077 |
| 4.5 | 8.04 | 0.77 | 0.062 | 0.357 | 0.043 | 0.069 |
| 5 | 8.76 | 0.77 | 0.068 | 0.294 | 0.035 | 0.057 |
| 6 | 9.36 | 0.78 | 0.073 | 0.241 | 0.029 | 0.047 |
| 7 | 10.20 | 0.79 | 0.080 | 0.165 | 0.020 | 0.032 |
| 8 | 10.56 | 0.79 | 0.083 | 0.133 | 0.016 | 0.026 |
| 9 | 10.80 | 0.79 | 0.085 | 0.111 | 0.013 | 0.021 |
| 10 | 10.92 | 0.79 | 0.086 | 0.100 | 0.012 | 0.019 |
| 11 | 11.16 | 0.79 | 0.089 | 0.078 | 0.009 | 0.015 |
| 12 | 11.40 | 0.80 | 0.091 | 0.056 | 0.007 | 0.011 |
| 13 | 11.64 | 0.80 | 0.093 | 0.033 | 0.004 | 0.006 |
| 14 | 11.88 | 0.80 | 0.095 | 0.011 | 0.001 | 0.002 |
| 15 | 11.92 | 0.80 | 0.095 | 0.008 | 0.001 | 0.002 |
| 16 | 11.94 | 0.80 | 0.095 | 0.006 | 0.001 | 0.001 |
| 17 | 12.00 | 0.80 | 0.096 | 0.000 | 0.000 | 0.000 |
| 18 | 12.00 | 0.80 | 0.096 | 0.000 | 0.000 | 0.000 |
| 19 | 12.00 | 0.80 | 0.096 | 0.000 | 0.000 | 0.000 |
| 20 | 12.00 | 0.80 | 0.096 | 0.000 | 0.000 | 0.000 |
| 21 | 12.00 | 0.80 | 0.096 | 0.000 | 0.000 | 0.000 |
| 22 | 12.00 | 0.80 | 0.096 | 0.000 | 0.000 | 0.000 |
| 23 | 12.00 | 0.80 | 0.096 | 0.000 | 0.000 | 0.000 |
| 25 | 12.00 | 0.80 | 0.096 | 0.000 | 0.000 | 0.000 |
| 30 | 12.00 | 0.80 | 0.096 | 0.000 | 0.000 | 0.000 |
| 35 | 12.00 | 0.80 | 0.096 | 0.000 | 0.000 | 0.000 |
| 40 | 12.00 | 0.80 | 0.096 | 0.000 | 0.000 | 0.000 |
| 45 | 12.00 | 0.80 | 0.096 | 0.000 | 0.000 | 0.000 |
| 50 | 12.00 | 0.80 | 0.096 | 0.000 | 0.000 | 0.000 |
| 55 | 12.00 | 0.80 | 0.096 | 0.000 | 0.000 | 0.000 |
| 60 | 12.00 | 0.80 | 0.096 | 0.000 | 0.000 | 0.000 |

Table A-19 operating condition used for $CO_2$ adsorption in fixed bed regime.

| **Type of fluidized bed** | **Fixed bed** | - |
|---|---|---|
| % conc. $CO_2$ at input | 12 | %vol. dry basis |
| Solid inventory: | 60 | g |
| $K_2CO_3$ weight | 21 | g |
| Riser Temperature: | 60 | °C |
| Temperature | 333 | K |
| Feed gas flow rate ($F_{input}$) | 0.8 | l/min |
| Water concentration | 18.5 | %vol. |
| Pressure | 1 | atm |
| Gas constant | 0.082 | (l/atm)/(g mole/K) |

Table A-20 row data for $CO_2$ adsorption in fixed bed regime.

| Time | % conc.$CO_{2\ output}$ | $Flow_{output}$ | $[CO_2]_{output}$ | F | $V_{CO2ads}$ | $W_{CO2\ ads}$ |
|---|---|---|---|---|---|---|
| (Minute) | %vol. | l/min | l/min | - | l/min | g/min |
| 0 | 0.00 | 0.70 | 0.000 | 1.000 | 0.120 | 0.193 |
| 2 | 0.00 | 0.70 | 0.000 | 1.000 | 0.120 | 0.193 |
| 4 | 0.00 | 0.70 | 0.000 | 1.000 | 0.120 | 0.193 |
| 4.5 | 0.00 | 0.70 | 0.000 | 1.000 | 0.120 | 0.193 |
| 5 | 0.00 | 0.70 | 0.000 | 1.000 | 0.120 | 0.193 |
| 6 | 0.00 | 0.70 | 0.000 | 1.000 | 0.120 | 0.193 |
| 7 | 0.00 | 0.70 | 0.000 | 1.000 | 0.120 | 0.193 |
| 8 | 0.00 | 0.70 | 0.000 | 1.000 | 0.120 | 0.193 |
| 9 | 0.00 | 0.70 | 0.000 | 1.000 | 0.120 | 0.193 |
| 10 | 0.00 | 0.70 | 0.000 | 1.000 | 0.120 | 0.193 |
| 11 | 0.00 | 0.70 | 0.000 | 1.000 | 0.120 | 0.193 |
| 12 | 0.00 | 0.70 | 0.000 | 1.000 | 0.120 | 0.193 |
| 13 | 0.00 | 0.70 | 0.000 | 1.000 | 0.120 | 0.193 |
| 14 | 0.00 | 0.70 | 0.000 | 1.000 | 0.120 | 0.193 |
| 15 | 0.00 | 0.70 | 0.000 | 1.000 | 0.120 | 0.193 |
| 16 | 0.30 | 0.71 | 0.002 | 0.978 | 0.117 | 0.189 |
| 17 | 2.69 | 0.73 | 0.019 | 0.797 | 0.096 | 0.154 |
| 18 | 3.94 | 0.74 | 0.029 | 0.698 | 0.084 | 0.135 |
| 19 | 6.23 | 0.75 | 0.047 | 0.511 | 0.061 | 0.099 |
| 20 | 7.65 | 0.77 | 0.059 | 0.390 | 0.047 | 0.075 |
| 21 | 10.65 | 0.79 | 0.084 | 0.124 | 0.015 | 0.024 |
| 22 | 11.31 | 0.79 | 0.090 | 0.064 | 0.008 | 0.012 |
| 23 | 11.67 | 0.80 | 0.093 | 0.030 | 0.004 | 0.006 |
| 25 | 11.98 | 0.80 | 0.096 | 0.002 | 0.000 | 0.000 |
| 30 | 11.98 | 0.80 | 0.096 | 0.002 | 0.000 | 0.000 |
| 35 | 11.74 | 0.80 | 0.094 | 0.024 | 0.003 | 0.005 |
| 40 | 11.97 | 0.80 | 0.096 | 0.003 | 0.000 | 0.001 |
| 45 | 11.98 | 0.80 | 0.096 | 0.002 | 0.000 | 0.000 |
| 50 | 11.97 | 0.80 | 0.096 | 0.003 | 0.000 | 0.000 |
| 55 | 12.00 | 0.80 | 0.096 | 0.000 | 0.000 | 0.000 |
| 60 | 12.00 | 0.80 | 0.096 | 0.000 | 0.000 | 0.000 |

Table A-21 operating condition used for $CO_2$ adsorption in multiple-bubbling regime.

| | | |
|---|---|---|
| Type of fluidized bed | Multiple-bubbling | - |
| % conc. $CO_2$ at input | 12 | %vol. dry basis |
| Solid inventory: | 60 | g |
| $K_2CO_3$ weight | 21 | grams |
| Riser Temperature: | 60 | °C |
| Temperature | 333 | K |
| Feed gas flow rate ($F_{input}$) | 3 | l/min |
| Water concentration | 18.5 | %vol. |
| Pressure | 1 | atm |
| Gas constant | 0.082 | (l/atm)/(g mole/K) |

Table A-22 row data for $CO_2$ adsorption in multiple-bubbling regime.

| Time | % conc.$CO_{2\ output}$ | $Flow_{output}$ | $[CO_2]_{output}$ | F | $V_{CO2ads}$ | $W_{CO2\ ads}$ |
|---|---|---|---|---|---|---|
| (Minute) | %vol. | l/min | l/min | - | l/min | g/min |
| 0 | 0.00 | 2.64 | 0.000 | 1.000 | 0.360 | 0.580 |
| 1 | 0.00 | 2.64 | 0.000 | 1.000 | 0.360 | 0.580 |
| 2 | 0.00 | 2.64 | 0.000 | 1.000 | 0.360 | 0.580 |
| 3 | 0.00 | 2.64 | 0.000 | 1.000 | 0.360 | 0.580 |
| 4 | 0.00 | 2.64 | 0.000 | 1.000 | 0.360 | 0.580 |
| 5 | 2.16 | 2.70 | 0.058 | 0.838 | 0.302 | 0.486 |
| 6 | 3.12 | 2.73 | 0.085 | 0.763 | 0.275 | 0.443 |
| 7 | 5.21 | 2.80 | 0.146 | 0.596 | 0.214 | 0.346 |
| 8 | 7.03 | 2.85 | 0.201 | 0.443 | 0.159 | 0.257 |
| 9 | 7.55 | 2.87 | 0.216 | 0.399 | 0.144 | 0.231 |
| 10 | 9.13 | 2.91 | 0.266 | 0.261 | 0.094 | 0.151 |
| 11 | 9.98 | 2.94 | 0.293 | 0.186 | 0.067 | 0.108 |
| 12 | 10.69 | 2.96 | 0.316 | 0.121 | 0.044 | 0.070 |
| 13 | 11.41 | 2.98 | 0.340 | 0.054 | 0.020 | 0.032 |
| 14 | 11.77 | 2.99 | 0.352 | 0.021 | 0.008 | 0.012 |
| 15 | 11.76 | 2.99 | 0.352 | 0.022 | 0.008 | 0.013 |
| 16 | 11.84 | 3.00 | 0.355 | 0.015 | 0.005 | 0.009 |
| 17 | 11.95 | 3.00 | 0.358 | 0.005 | 0.002 | 0.003 |
| 18 | 11.99 | 3.00 | 0.360 | 0.001 | 0.000 | 0.001 |
| 19 | 11.91 | 3.00 | 0.357 | 0.008 | 0.003 | 0.005 |
| 20 | 11.91 | 3.00 | 0.357 | 0.008 | 0.003 | 0.005 |

Table A-23 operating condition used for $CO_2$ adsorption in slugging regime.

| | | |
|---|---|---|
| Type of fluidized bed | Slugging | - |
| % conc. $CO_2$ at input | 12 | %vol. basis |
| Solid inventory: | 60 | g |
| $K_2CO_3$ weight | 21 | g |
| Riser Temperature: | 60 | °C |
| Temperature | 333 | K |
| Feed gas flow rate ($F_{input}$) | 6 | l/min |
| Water concentration | 18.5 | %vol. |
| Pressure | 1 | atm |
| Gas constant | 0.082 | (l/atm)/(g mole/K) |

Table A-24 row data for $CO_2$ adsorption in slugging regime.

| Time | % conc.$CO_{2\ output}$ | $Flow_{output}$ | $[CO_2]_{output}$ | F | $V_{CO2ads}$ | $W_{CO2\ ads}$ |
|---|---|---|---|---|---|---|
| (Minute) | %vol. | l/min | l/min | - | l/min | g/min |
| 0 | 0.15 | 5.29 | 0.008 | 0.989 | 0.712 | 1.147 |
| 1 | 1.56 | 5.37 | 0.084 | 0.883 | 0.636 | 1.025 |
| 2 | 3.73 | 5.50 | 0.205 | 0.715 | 0.515 | 0.829 |
| 3 | 6.32 | 5.66 | 0.358 | 0.503 | 0.362 | 0.584 |
| 4 | 7.50 | 5.73 | 0.430 | 0.403 | 0.290 | 0.468 |
| 5 | 9.38 | 5.84 | 0.548 | 0.239 | 0.172 | 0.277 |
| 6 | 10.38 | 5.90 | 0.613 | 0.149 | 0.107 | 0.173 |
| 7 | 10.75 | 5.92 | 0.637 | 0.116 | 0.083 | 0.134 |
| 8 | 11.36 | 5.96 | 0.677 | 0.060 | 0.043 | 0.069 |
| 9 | 11.76 | 5.99 | 0.704 | 0.022 | 0.016 | 0.026 |
| 10 | 11.83 | 5.99 | 0.709 | 0.016 | 0.011 | 0.018 |
| 11 | 11.94 | 6.00 | 0.716 | 0.006 | 0.004 | 0.007 |
| 12 | 11.99 | 6.00 | 0.720 | 0.000 | 0.000 | 0.001 |
| 13 | 12.00 | 6.00 | 0.720 | 0.000 | 0.000 | 0.000 |
| 14 | 12.00 | 6.00 | 0.720 | 0.000 | 0.000 | 0.000 |
| 15 | 12.00 | 6.00 | 0.720 | 0.000 | 0.000 | 0.000 |
| 16 | 12.00 | 6.00 | 0.720 | 0.000 | 0.000 | 0.000 |
| 17 | 12.00 | 6.00 | 0.720 | 0.000 | 0.000 | 0.000 |
| 18 | 12.00 | 6.00 | 0.720 | 0.000 | 0.000 | 0.000 |
| 19 | 12.00 | 6.00 | 0.720 | 0.000 | 0.000 | 0.000 |
| 20 | 12.00 | 6.00 | 0.720 | 0.000 | 0.000 | 0.000 |

Table A-25 operating condition used for $CO_2$ adsorption in turbulent regime.

| | | |
|---|---|---|
| Type of fluidized bed | Turbulent | - |
| % conc. $CO_2$ at input | 12 | %vol. drybasis |
| Solid inventory: | 60 | g |
| $K_2CO_3$ weight | 21 | g |
| Riser Temperature: | 60 | °C |
| Temperature | 333 | K |
| Feed gas flow rate ($F_{input}$) | 9 | l/min |
| Water concentration | 18.5 | %vol. |
| Pressure | 1 | atm |
| Gas constant | 0.082 | (l/atm)/(g mole/K) |

Table A-26 row data for $CO_2$ adsorption in turbulent regime.

| Time | % conc.$CO_{2\ output}$ | $Flow_{output}$ | $[CO_2]_{output}$ | F | $V_{CO2ads}$ | $W_{CO2\ ads}$ |
|---|---|---|---|---|---|---|
| (Minute) | %vol. | l/min | l/min | - | l/min | g/min |
| 0 | 0.52 | 7.97 | 0.041 | 0.962 | 1.039 | 1.674 |
| 1 | 1.56 | 8.06 | 0.126 | 0.884 | 0.954 | 1.538 |
| 2 | 3.73 | 8.26 | 0.308 | 0.715 | 0.772 | 1.244 |
| 3 | 6.32 | 8.49 | 0.536 | 0.503 | 0.544 | 0.876 |
| 4 | 8.50 | 8.68 | 0.738 | 0.317 | 0.342 | 0.551 |
| 5 | 9.94 | 8.81 | 0.876 | 0.189 | 0.204 | 0.329 |
| 6 | 10.38 | 8.85 | 0.919 | 0.149 | 0.161 | 0.260 |
| 7 | 10.75 | 8.89 | 0.955 | 0.116 | 0.125 | 0.201 |
| 8 | 11.36 | 8.94 | 1.015 | 0.060 | 0.065 | 0.104 |
| 9 | 11.76 | 8.98 | 1.056 | 0.022 | 0.024 | 0.039 |
| 10 | 11.83 | 8.98 | 1.063 | 0.016 | 0.017 | 0.028 |
| 11 | 11.94 | 8.99 | 1.074 | 0.006 | 0.006 | 0.010 |
| 12 | 11.99 | 9.00 | 1.079 | 0.000 | 0.001 | 0.001 |
| 13 | 12.00 | 9.00 | 1.080 | 0.000 | 0.000 | 0.000 |
| 14 | 12.00 | 9.00 | 1.080 | 0.000 | 0.000 | 0.001 |
| 15 | 12.00 | 9.00 | 1.080 | 0.000 | 0.000 | 0.000 |
| 16 | 12.00 | 9.00 | 1.080 | 0.000 | 0.000 | 0.000 |
| 17 | 12.00 | 9.00 | 1.080 | 0.000 | 0.000 | 0.000 |
| 18 | 12.00 | 9.00 | 1.080 | 0.000 | 0.000 | 0.000 |
| 19 | 12.00 | 9.00 | 1.080 | 0.000 | 0.000 | 0.000 |
| 20 | 12.00 | 9.00 | 1.080 | 0.000 | 0.000 | 0.000 |

Table A-27 operating condition used for $CO_2$ adsorption in fast fluidization regime.

| | | |
|---|---|---|
| Type of fluidized bed | Fast fluidized | - |
| % conc. $CO_2$ at input | 12 | %vol. dry basis |
| Solid inventory: | 300 | g |
| $K_2CO_3$ weight | 105 | g |
| Riser Temperature: | 60 | °C |
| Temperature | 333 | K |
| Feed gas flow rate ($F_{input}$) | 21 | l/min |
| Water concentration | 18.5 | %vol. |
| Pressure | 1 | atm |
| Gas constant | 0.082 | (l/atm)/(g mole/K) |

Table A-28 row data for $CO_2$ adsorption in fast fluidization regime.

| Time | % conc.$CO_{2\ output}$ | $Flow_{output}$ | $[CO_2]_{output}$ | F | $V_{CO2ads}$ | $W_{CO2\ ads}$ |
|---|---|---|---|---|---|---|
| (Minute) | %vol. | l/min | l/min | - | l/min | g/min |
| 0 | 4.32 | 19.39 | 0.838 | 0.67 | 1.682 | 2.710 |
| 2 | 4.92 | 19.51 | 0.960 | 0.62 | 1.560 | 2.513 |
| 4 | 4.42 | 19.41 | 0.859 | 0.66 | 1.661 | 2.677 |
| 6 | 4.73 | 19.47 | 0.921 | 0.63 | 1.599 | 2.577 |
| 8 | 5.85 | 19.71 | 1.153 | 0.54 | 1.367 | 2.202 |
| 10 | 9.14 | 20.40 | 1.865 | 0.26 | 0.655 | 1.055 |
| 12 | 9.74 | 20.53 | 1.999 | 0.21 | 0.521 | 0.839 |
| 14 | 11.06 | 20.80 | 2.301 | 0.09 | 0.219 | 0.352 |
| 16 | 11.15 | 20.82 | 2.323 | 0.08 | 0.197 | 0.318 |
| 18 | 11.19 | 20.83 | 2.331 | 0.07 | 0.189 | 0.304 |
| 20 | 11.50 | 20.89 | 2.402 | 0.05 | 0.118 | 0.190 |
| 22 | 11.47 | 20.89 | 2.397 | 0.05 | 0.123 | 0.198 |
| 24 | 11.68 | 20.93 | 2.446 | 0.03 | 0.074 | 0.119 |
| 26 | 11.75 | 20.95 | 2.462 | 0.02 | 0.058 | 0.093 |
| 28 | 11.77 | 20.95 | 2.466 | 0.02 | 0.054 | 0.086 |
| 30 | 11.79 | 20.96 | 2.471 | 0.02 | 0.049 | 0.079 |
| 35 | 11.90 | 20.98 | 2.497 | 0.01 | 0.023 | 0.038 |
| 40 | 11.98 | 21.00 | 2.515 | 0.00 | 0.005 | 0.008 |
| 50 | 11.94 | 20.99 | 2.507 | 0.01 | 0.013 | 0.021 |
| 60 | 12.00 | 21.00 | 2.520 | 0.00 | 0.000 | 0.000 |

# VITA

Miss Or-ampai Jaiboon was born on June 30, 1982 in Ubonratchatanee, Thailand.

**University Education :**

2001-2005 Bachelor of Science, Department of Chemistry, Faculty of Science, King Mongkut's Institute of Technology Ladkrabang, Bangkok, Thailand.

2005-2007 Master of Science, Department of Chemical Technology, Faculty of Science, Chulalongkorn University, Bangkok, Thailand.

2007-2011 Doctor of Philosophy, Department of Chemical, Chulalonkorn University, Bangkok, Thailand.